ASPECTS OF SENSORY CUES AND PROPULSION IN MARINE ZOOPLANKTON HYDRODYNAMIC DISTURBANCES

A Thesis
Presented to
The Academic Faculty

by

Kimberly Bernadine Catton

In Partial Fulfillment
Of the Requirements for the Degree
Doctor of Philosophy in Civil Engineering

School of Civil and Environmental Engineering
Georgia Institute of Technology

December 2009

ASPECTS OF SENSORY CUES AND PROPULSION IN MARINE ZOOPLANKTON HYDRODYNAMIC DISTURBANCES

Approved by:

Dr. Donald R. Webster, Advisor
School of Civil and Environmental Engineering
Georgia Institute of Technology

Dr. Thorsten Stoesser
School of Civil and Environmental Engineering
Georgia Institute of Technology

Dr. Jeannette Yen
School of Biology
Georgia Institute of Technology

Dr. Terry W. Sturm
School of Civil and Environmental Engineering
Georgia Institute of Technology

Dr. Philip J. W. Roberts
School of Civil and Environmental Engineering
Georgia Institute of Technology

Date Approved: 30 July 2009

ACKNOWLEDGEMENTS

First, I would like to thank and acknowledge my Civil Engineering advisor, Dr. Donald Webster, for his insight into the research, availability, and inspiration. Without his hard work, this dissertation would not have been possible. I would also like to thank my biology advisor, Dr. Jeannette Yen, for her incredible fieldwork abilities, which included the successful identification of numerous zooplankton species, the ability to sort copepods on a rocking boat, and her willingness to forgo sleep for the data collection effort. Her generosity also contributed to the success of this research as she provided the lodging necessary to collect the *Euchaeta rimana* flow fields in Hawai'i. The *Cues in the Sea* IGERT program was also invaluable in this effort as a source of funding and inspiration. I am also appreciative of the time and comments provide by the other members of my thesis committee, Dr. Terry Sturm, Dr. Phil Roberts, and Dr. Thorsten Stoesser.

Next, I would like to thank my colleagues (Environmental Fluid Mechanics and Biology graduate students) for their input and advice on this research throughout my tenure at Georgia Tech. In particular, Rachel Lasley's assistance in sorting and maintaining the copepods was invaluable the research effort. From the computational side, I owe Jason Brown, Brock Woodson, Sarah Kelly Delavan and Brian Dickman a commendation for their efforts on the computer code and analysis of the results.

The collaboration between Georgia Tech and the Australian Antarctic Division in Tasmania was essential to the collection of the *Euphausia superba* data and the efforts of Dr. So Kawaguchi and Rob King merit additional thanks. Much gratitude is also due Dr.

William Peterson and his colleagues at the Hatfield Marine Station for collection and care of the *Euphausia pacifica* used in this study.

Finally, I would like to thank my husband, Thomas Bradley, for his patience, proofreading efforts, and support during my time at Georgia Tech.

TABLE OF CONTENTS

LIST OF TABLES

Page

LIST OF FIGURES

Page

LIST OF SYMBOLS

X	longitudinal axis
Y	transverse axis
Z	vertical axis
R	radial axis
θ	circumferential axis
x	longitudinal coordinate
y	transverse coordinate
z	vertical coordinate
r	radial coordinate
t	time
u_x , u	x-direction velocity
u_y , v	y-direction velocity
u_z , w	z-direction velocity
u_r	radial velocity
u_θ	tangential velocity
e_{xx}	linear strain rate (x-direction)
e_{yy}	linear strain rate (y-direction)
e_{zz}	linear strain rate (z-direction)
e_{xy}	shear strain rate (x-y direction)
e_{xz}	shear strain rate (x-z direction)
ω_z	z-component of vorticity
ω_y	y-component of vorticity
Ψ	energy dissipation rate
μ	dynamic viscosity
ν	kinematic viscosity
ρ	fluid density
P	average pressure
Re	Reynolds number

SUMMARY

The hydrodynamic disturbances generated by two types of free-swimming, marine zooplankton were quantified experimentally in the laboratory with a novel, infrared Particle Image Velocimetry (PIV) system. The study consisted of three main parts: (1) the flow fields of free-swimming and tethered *Euchaeta antarctica* were compared to determine the effects of tethering, (2) three species of copepods (*Euchaeta rimana*, *Euchaeta elongata*, and *Euchaeta antarctica*) that live in seawater in a range of temperatures (23 ºC – 0 ºC) and a corresponding range of fluid viscosity (0.97 – 1.88 $mm^2\ s^{-1}$) were analyzed experimentally and with a computational fluid dynamics model (FLUENT) to assess the effect of size and fluid viscosity on the flow fields, (3) the flow fields were collected for individuals of two species of euphausiids (*Euphausia pacifica* and *Euphausia superba*) to compare the effect of size and Reynolds number on propulsion and the spatial extent of the flow disturbance. In addition to the measured flow fields around solitary krill, flow fields were collected around small, coordinated groups of *E. superba* to examine group sensory cues through hydrodynamics.

In the first part of this investigation, it was determined that tethering zooplankton during data collection resulted in flow fields with increased asymmetry and larger spatial extent due to the unbalanced force applied to the fluid by the tether. In response to these findings, only flow fields collected for free-swimming organisms were used in the subsequent studies. In the second part of the study, the increase in viscosity between subtropical and temperate fluid environments in conjunction with increased size and species-specific swimming speeds resulted in similar Reynolds numbers among *E.*

elongata and *E. rimana* (in both cruising and escaping modes). During cruising (*Re* ~10), the spatial extent of the copepod hydrodynamic disturbances and propulsion costs were similar between species. In the case of fluid disturbances of escape (*Re* ~ 100), the spatial extent and energetic cost were larger for the larger species (*E. elongata*). In the third part of the study, the hydrodynamic disturbance produced by *E. superba* (larger krill species) was found to be longer in horizontal spatial extent and at scales more appropriate for communication within schools than the hydrodynamic disturbance produced by *E. pacifica*. However, the sensory cue in coordinated groups of krill was complicated by the interaction of multiple flow disturbance fields, which suggests that hydrodynamic cues between krill in groups are restricted to small distances. The energetic cost of propulsion was ten times greater for the larger species of krill, and energetic expenditure did not appear to decrease for krill swimming in coordinated groups.

CHAPTER 1

INTRODUCTION

The broad objective of this study is to investigate aspects of sensory cues and propulsion in two types of marine zooplankton (copepods and krill) over a range of Reynolds numbers (order of 10 to 1,000). Zooplankton are small, aquatic animals that are widely acknowledged as an important link in the food web between photosynthetic phytoplankton and higher trophic-level species, such as fish and whales. Aggregations of zooplankton attract large predators (Hain et. al., 1982; Fraser et al., 1989), many of which are commercially-important species. In addition, krill are an important fisheries stock in the Antarctic region (Kanda et al., 1982). Because of the importance of zooplankton in fisheries, there is widespread interested in the sensory cues used to maintain zooplankton aggregations (Hamner, 1984; Wiese and Ebina, 1995) and the predator-prey interactions that determine ecological community structure (Ohman, 1990). Similarly, the propulsive ability of zooplankton is of interest to researchers as it determines the migration ability of zooplankton (Kils, 1982) and the energetic costs of behavior (Ritz, 2000).

Hydromechanical cues are an important mechanism for cues between zooplankton (reviewed in Visser, 2001) and are believed to be used by zooplankton to maintain coordinated positions in aggregations (e.g., schools) (Hamner, 1984; Wiese and Ebina, 1995). Zooplankton also use hydromechanical cues to sense prey (Kerfoot, 1978; Svensen and Kiørboe, 2000; Fields and Yen, 2002), predators (Yen and Fields, 1992; Kiørboe et al., 1999; Buskey et al., 2002; Fields and Yen, 2002), mates (Yen et al., 1998), and oceanic structure (Woodson et al., 2005; Woodson et al., 2007a,b). Zooplankton that

can accurately sense these hydromechanical cues have a competitive advantage, which leads to greater species success. Therefore, the response of zooplankton to hydrodynamic disturbances has ecological implications in respect to population dynamics and evolution of animal behavior.

Zooplankton have hydromechanical receptor systems that sense fluid disturbances (Yen et al., 1992; Patria and Wiese, 2004). The fluid disturbance that elicits a behavioral response in zooplankton is dependent on the species and position in the food web (Kiørboe and Visser, 1999; Kiørboe et al., 1999; Visser, 2001). For instance, a threshold fluid deformation rate (either linear or shear deformation) triggers an escape response in copepods (Fields and Yen, 1997a; Kiørboe et al., 1999), whereas, the absolute velocity magnitude is suspected to be the hydromechanical cue sensed by copepod predators (Svensen and Kiørboe, 2000). To understand the hydromechanical cues between zooplankton, the velocity fields generated by zooplankton must be measured in order to quantify the absolute velocity magnitude and deformation rate fields. Thus, the motivation to better understand the mechanosensory disturbance of swimming zooplankton requires measuring the velocity field with sufficient precision and resolution to accurately calculate spatial derivatives.

The cost of propulsion can also be derived from the velocity fields by estimating the energy dissipated into the fluid by zooplankton motion. Previous methods employed to estimate the energetic costs associated with zooplankton propulsion include estimating oxygen consumption rates (Ritz, 2000; Swadling et al., 2005) and estimations of the drag force (Kils, 1982). These methods have estimated the cost of propulsion at 0.1 to 95% of

the total metabolism of the organism (Alcarez and Strickler, 1988). Given the large range of propulsion cost estimates, the direct quantification of the cost of propulsion from the flow fields may provide more accurate results and allow for comparisons between species, swimming behaviors, and aggregation behaviors.

In the current study, two types of zooplankton: copepods and krill were selected for flow field investigation because they present contrasting modes of swimming and present specific questions about their hydrodynamic disturbances. The proposed research will address the following questions about hydromechanical cues and the cost of propulsion created by swimming zooplankton:

1) What is the effect of tethering a specimen at a fixed location on the measured flow field, and to what extent does tethering alter the estimation of the hydromechanical cue created by a copepodid, *Euchaeta antarctica*? For a free-swimming copepod, what is the flow disturbance pattern and hydromechanical cue generated?

2) What is the effect of the subtropical and temperate marine environments, where *Euchaeta rimana* and *Euchaeta elongata* reside, on the flow fields on *Euchaeta* copepods? How do differences in the flow field generated by the two species alter the hydromechanical cue available to prey and predators? How does the cost of propulsion vary between marine environments and copepod behavior?

3) Do the hydrodynamic disturbances generated by *Euphausia pacifica*, a non-schooling krill species, differ from the hydrodynamic disturbances generated by *Euphausia superba,* an obligate schooler? What are the implications of the differences in

flow field structure on intraspecies sensory cues, the ability to school, and the cost of propulsion?

CHAPTER 2

LITERATURE REVIEW

This chapter includes a discussion of flow fields generated by krill and copepods with respect to hydromechanical cues and propulsion. In addition, a section of this review is devoted to a summary of zooplankton swimming behavior. The objective of this chapter is to provide background information and to further explain the motivation for the proposed study. Each section begins with a general review of the subject, which is followed by a review of the previous findings for the specific species involved in this study.

2.1 Zooplankton swimming behavior

Zooplankton is a non-specific term given to a group of morphologically and behaviorally diverse organisms that are small with limited propulsion abilities (e.g., krill, copepods, jellyfish, dinoflagellates, and mollusks). In addition to organisms that spend their entire life cycle as zooplankton, some species of fish and benthic organisms spend their juvenile stage as free-swimming plankton. Zooplankton form an intermediate level in the food web between phytoplankton and fish. In the case of krill, the food chain spans from phytoplankton to krill to whales and skips the larval fish and cephalopods that usually directly feed on zooplankton (Wickstead, 1976). Numerically, the zooplankton community is dominated by copepods who account for 50 – 80% of the population (Wickstead, 1976). Krill are also an important type of zooplankton as they compose a majority of the biomass and are a keystone species in the Antarctic region (Nicol and

Endo, 1997). Thus, an understanding of the sensory cue and propulsion aspects of the flow fields generated by these two types of zooplankton will provide information about the most abundant types of zooplankton.

The open ocean lacks the typical terrestrial forms of refuge from predation. Accordingly, zooplankton have evolved different strategies to avoid predation in the pelagic ocean which include small size, invisibility due to transparency, diurnal vertical migration, and exploitation of the sea surface (Hamner, 1995). The swimming behavior of zooplankton is also diverse in response to predation risks. For example, jellyfish swim at very low speeds but have advanced defense systems, whereas copepods have a rapid escape response to predators. In addition, zooplankton morphology is diverse, ranging from hard-shelled crustaceans to gelatinous jellyfish to winged pteropods. Because of the varied morphology, zooplankton propulsion mechanisms and swimming behavior are varied and even species-specific. The range of swimming behaviors is in part due to the flow regime of swimming zooplankton, which is described by Reynolds number ($Re = u_s l/\nu$) in the range of 10^{-2} to 10^{4} (the laminar to transitional flow regime) (Vogel, 1994). The swimming behavior employed by zooplankton must effectively span a range of Reynolds numbers during the life cycle of the organism to ensure the success of the species. Copepod swimming occurs at Reynolds numbers spanning 0.01 to 1000 (Yen, 2000), whereas krill swimming occurs at Reynolds numbers ranging from 100 to 10,000 (Yen et al., 2003; Kils, 1982). The following discussion will focus on steady swimming behaviors (cruising, pleopod swimming) and unsteady behaviors (escapes) of copepods and krill.

2.1.1 Copepod swimming behavior (genus: *Euchaeta*)

Copepods are distributed worldwide in a range of water temperatures from polar to tropical ocean environments. The three species of interest in this study are *Euchaeta antarctica* (polar species) (Figure 2.1), *Euchaeta elongata* (temperate species) (Figure 2.2), and *Euchaeta rimana* (subtropical species) with prosome lengths of approximately 7 mm, 4 mm, and 2 mm, respectively. Similar to other organisms, a colder fluid environment is associated with a larger body size (Chapelle and Peck, 1999). The current nomenclature, based on sequencing of 16s rRNA and vertical migration behavior, assigns *Euchaeta antarctica* and *Euchaeta elongata* in the *Paraeuchaeta* genus, although this nomenclature has not been widely adopted (Braga et al., 1999). The *Euchaeta rimana* line branched off from the ancestor of *E. elongata* and *E. antarctica* and became a shallow-living species. Evolutionarily, the common ancestor of all three *Euchaeta* species was a subtropical species and independent migrations occurred to temperate and Antarctic waters (Braga et al., 1999). Overall, the evolutionary similarity between *E. antarctica* and *E. elongata* may result in similar swimming behavior.

Euchaeta are carnivorous copepods that prey on smaller copepods and fish larvae (Yen, 1983; Yen, 1985; Greene and Landry, 1985; Yen, 1991). *E. elongata* prefer copepod prey species with lengths of 0.6 – 1 mm and fish larvae (Yen, 1985), whereas *E. rimana* prey on smaller copepods of 0.3 – 0.7 mm in length (Yen, 1988). Predatory copepods have an important role in the aquatic communities as selective foragers that precipitate the evolution of defense tactics in smaller copepods (Kerfoot, 1978). Large copepod species, such as *Euchaeta antarctica,* are the primary food item of

macrozooplankton (amphipods, chaetognaths), fish, seabirds (petrels), and penguins (Bocher et al., 2002). Therefore, *Euchaeta* are an important predator within the zooplankton community and prey species.

The swimming behavior of *Euchaeta* is dependent on whether the copepod is foraging or escaping from a predator. *Euchaeta* forage for smaller copepods by gliding through the water at a constant speed in a behavior known as cruising. When cruising, the copepod is propelled forward by the beating of the second antennae (see Figure 2.3 for the position of the second antennae). Turning motions are initiated every 2.6 s by the swimming legs and a tucking motion of the urosome to the body (Yen, 1988). Overall, the swimming speeds of *E. elongata* and *E. rimana* are similar, but the migration patterns are different. The cruising swim pattern varies based on the species and the copepod gender. *E. elongata*, the temperate species, vertically migrates 200 to 400 meters in a diurnal migration, and as a result these copepods swim vertically in a sinusoidal pattern at an average speed of 0.6 cm s^{-1} (Yen, 1985; Greene and Landry, 1985). Contrarily, female *E. rimana* primarily swim in the horizontal direction at an average swimming speed of 0.7 cm s^{-1} (Yen, 1988). However, male *E. rimana* swim predominantly upward in the vertical direction at an average speed of 0.75 cm s^{-1} and then sink at a velocity of 0.5 cm s^{-1}. Further, there is sexual dichotomy in the behavior and feeding habits of *E. rimana*. Female *E. rimana* have larger feeding appendages and mechanoreceptive setae to find prey, whereas these body parts are reduced in the non-feeding, adult males whose only mission is to find a mate (Yen, 1988).

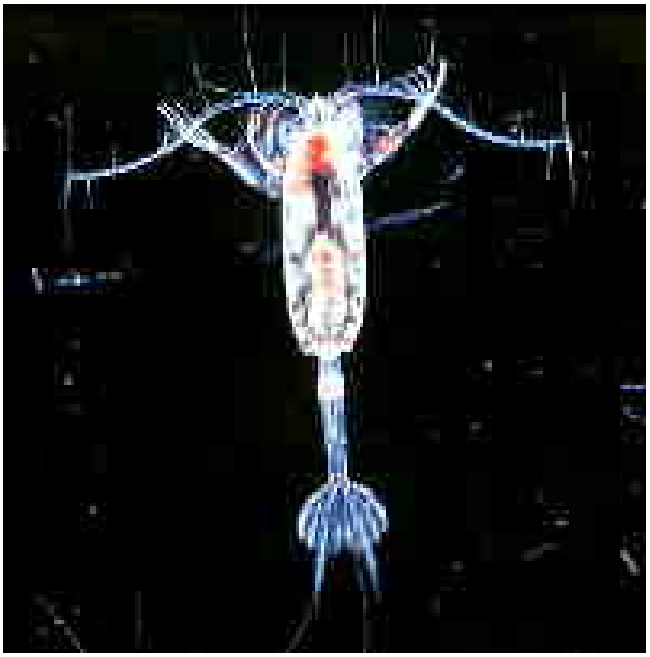

Figure 2.1 Photograph of *Euchaeta antarctica* (Photo courtesy of Jeannette Yen).

Figure 2.2 Photograph of *Euchaeta elongata* (Photo courtesy of Steve Bollens).

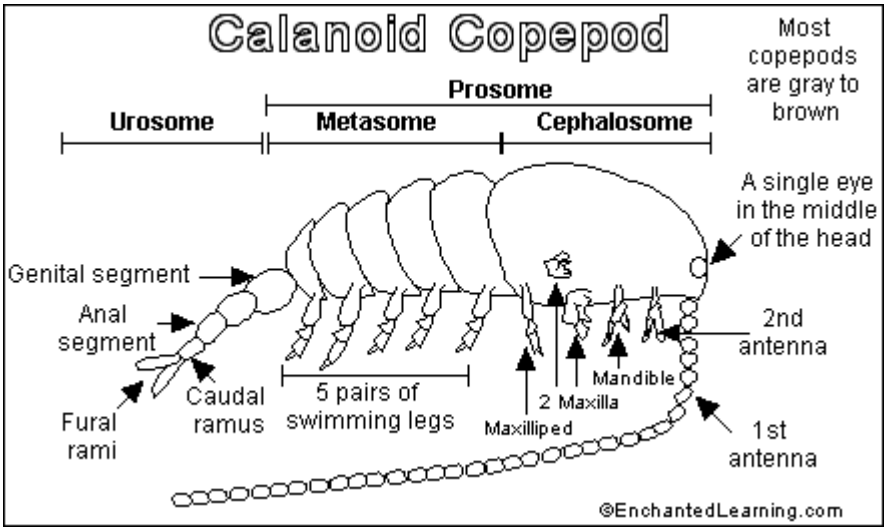

Figure 2.3 Drawing of calanoid copepod anatomy (Drawing courtesy of Enchanted Learning).

The escape behavior of *Euchaeta* is initiated by a synchronized contraction of the first antennae and stroke of the swimming legs to generate a brief and large acceleration of the organism. Copepod escapes consist of a series of jumps at a rate of 50 – 200 Hz (Lenz and Hartline, 1999; Buskey et al., 2002). Generally, escapes tend to occur in the upward direction and the escape velocity is larger for larger copepods (Buskey et al., 2002). The range of escape speeds for *E. rimana* was measured as 30 – 38 cm s^{-1} (Yen, 1988; Yen, 2000). The escape velocities of *E. antarctica* and *E. elongata* have not been accurately documented at this point. The simultaneous measurement of copepod escapes with flow field analysis is needed for the larger *Euchaeta* species to determine the variation in escape speeds with geographical location and copepod size.

2.1.2 Krill swimming behavior (genus: *Euphausia*)

Euphausia pacifica Hansen (Figure 2.4) is a dominant species in the northern regions of the Pacific Ocean that is typically found in inland fjords and along the continental shelf break. Pacific krill are smaller than the Antarctic krill (discussed below) with a maximum length of 20 mm (Nicol and Endo, 1997). *Euphausia pacifica* typically do not live in dense aggregations but will swarm at the surface when adult individuals are longer than 12 mm (reviewed in Bollens et al., 1992; de Robertis, 2002). Additionally, Nicol (1984) suggested that the occasional *E. pacifica* swarms (Figure 2.7) form for a reproductive function. Recent in situ observations of *E. pacifica* showed that vertically migrating individuals were at low densities and randomly organized (de Robertis et al., 2003). Thus, *E. pacifica* is a species capable of forming social aggregations in the form of swarms but are not often found in aggregations.

Euphausia superba (Antarctic krill) (Figure 2.5) is the largest species of krill (maximum length of 65 mm) and is found in the Southern Ocean off the coast of Antarctica (Nicol and Endo, 1997). Antarctic krill have a lifespan of 5 years and live in separate geographical areas during different stages of development (Marr, 1962). Juveniles, who are referred to as furciliae, congregate under ice shelves or icebergs at a density 100 times higher than in the open ocean (Hamner et al., 1989). At adulthood, *E. superba* form schools (Figure 2.6) of the same age and size and travel offshore to the open ocean (Siegel, 2000). *E. superba* schools migrate over distances of 50 – 100 km in a few weeks time (Kanda, 1982) and their distribution is patchy and unpredictable (Hamner, 1984). These schools also vertically migrate during the summer period within the upper 150 meters of the water column (Miller and Hampton, 1989). Overall, *E. superba* is an obligate schooler and is capable of swimming at high speeds over long distances.

Krill have two distinct swimming modes: pleopod swimming and tail swimming (escape behavior). Pleopod swimming is the typical mode of swimming. The five pairs of pleopods (see Figure 2.8 for the location of pleopods) beat in a metachronal rhythm, which results in a mean uniform velocity of approximately 6 cm s^{-1} and a maximum velocity of 8 body lengths per second (Kils, 1979). Pleopod swimming speed is determined by the efficiency of the stroke rather than by the pleopod beat rate. The pleopod beat rate remains the same for krill swimming at 0 cm s^{-1} to 15 cm s^{-1}, and only at speeds higher than 15 cm s^{-1} does the velocity increase with increased beat frequency (Kils, 1982). Tail swimming is an escape response that is generated by a repetitive bending and stretching of the abdomen and results in a fluctuating velocity that oscillates

between 20 and 100 cm s^{-1} (Kils, 1979). Table 2.1 is a summary of previous observations of *E. pacifica* and *E. superba* swimming behavior that includes krill length, swimming speeds, and body orientation. In general, length and swimming speed are greater for *E. superba* compared to *E. pacifica* in both laboratory and field studies. Increased body length and krill density were associated with increased swimming speeds (Kils, 1979; Miyashita et al., 1996). Estimations of the body orientation varied widely between studies due to difference in swimming behavior in the studies (i.e., hovering, pleopod swimming, schooling), variables tested, and measurement method. Miyashita et al. (1996) found that the body orientation of *E. pacifica* depended on the swimming behavior: hovering (mean angle = 36.9 degrees) and swimming fast (velocities greater between 1 – 2 cm s^{-1}) (mean angle = 15.0 degrees). *E. superba* swimming angle also depends on swimming behavior as hovering krill orient at an angle of 55 degrees and faster swimming krill orient at 20 to 30 degrees (Kils, 1982). Miyashita et al. (1996) suggested that the difference in body angles between species is caused by differences in body morphology. Body orientation is also sex dependent; males have been shown to orient more horizontally than females (Endo, 1993). Also, the swimming angle decreased with an increase in krill density (70 per tank) (Miyashita et al., 1996). In terms of schooling, the larger swimming speeds typical of *E. superba* are more suitable to schooling, migrating species. The consequences of the differences in swimming behavior between *E. superba* and *E. pacifica* on the flow fields will be discussed in the next section.

Figure 2.4 *Euphausia pacifica* (Photo courtesy of Sarah Goldthwait-Stone).

Figure 2.5 *Euphausia superba* (Photo courtesy of Cecilie Broms Årnes).

Figure 2.6 School of krill (Photo courtesy of Ronald Pedersen).

Figure 2.7 Krill swarm (Photo courtesy of Jamie Hall).

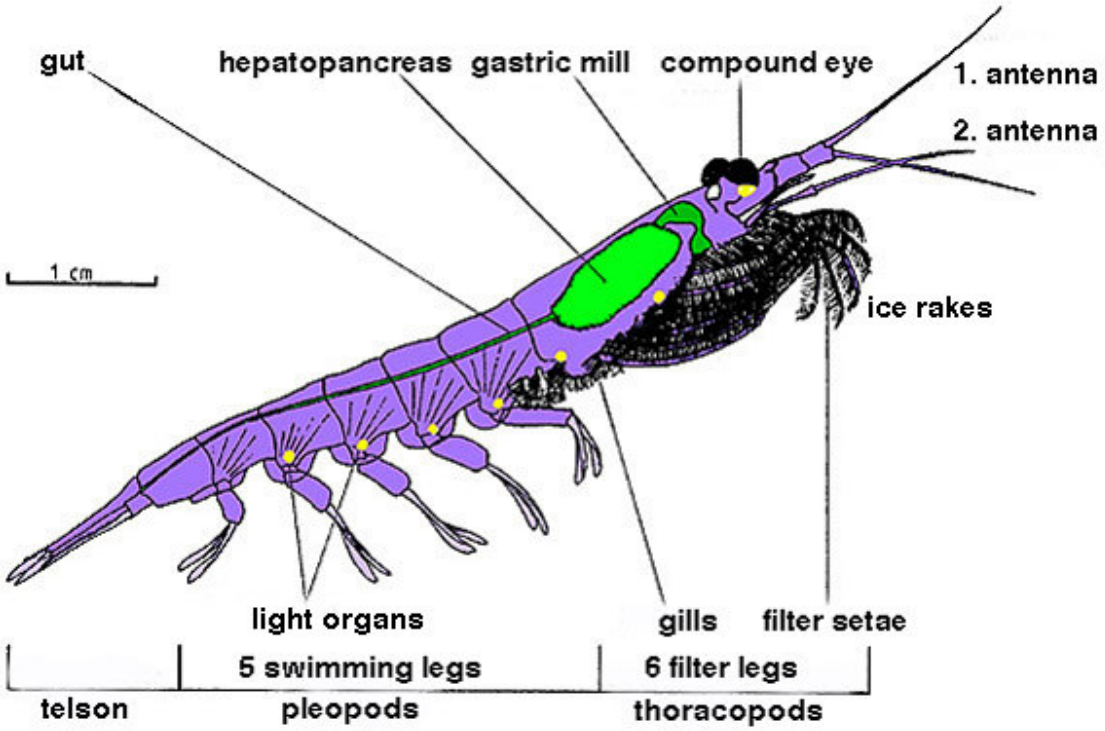

Figure 2.8 Drawing of *Euphausia superba* anatomy (Drawing courtesy of Uwe Kils).

Table 2.1. Summary of reported euphausiid swimming behavior. Values listed as mean ± standard deviation unless otherwise noted.

Species	**Method**	**Body length (cm)**	**Swimming speed (cm s^{-1})**	**Swimming angle (degrees)**	**Source**
Euphausia pacifica	Annular respirometer	1.4 – 1.7	0 – 9.7	-	Torres and Childress (1983)
E. pacifica	Video recording in tank	1.59 ± 0.138 1.69 ± 0.131	0 – 1 (hovering) 1 – 5 (swimming)	36.9 ± 12.9 (hovering) 15.0 ± 24.4 (swimming)	Miyashita et al. (1996)
E. pacifica	Field observations	-	-	-9.8	Kristensen and Dalen (1986)
E. pacifica	In situ 3D acoustic observations	1.2 – 2.2 (range)	1.8 (day) 1.2 – 3.5 (dusk)	± 15 (<10% of population)	de Robertis et al. (2003)
E. pacifica	In situ 3D acoustic observations	1.5 – 2.0	0.3 – 1.2 (range)	-	Jaffe et al. (1999)
Euphausia superba	Video in respiration chamber	3.6 (mean)	Current speed < 5 cm s^{-1} Current speed > 5 cm s^{-1}	45 – 60 0 – 5	Swadling et al. (2005)
E. superba	High speed camera in tank	-	6 (undisturbed pleopod swimming) 50 (escape)	-	Kils (1979)
E. superba	High speed camera in laboratory	5.0 – 6.0	0 – 15 (pleopod swimming)	55 (hovering) 20 – 30 (6 – 10 cm s^{-1})	Kils (1982)
E. superba	Video	2 – 4	10 – 20 (pleopod swimming)	0	Hamner (1984)

2.2 Zooplankton flow fields

2.2.1 Flow visualization methods

Zooplankton flow fields have been quantified with the following methods Schlieren optics (Strickler, 1977), high-speed micro-cinematography (Alcaraz et al., 1980; Koehl and Strickler, 1981), particle tracking (Yen et al., 1991; Yen and Fields, 1992; Fields and Yen, 1993; Bundy and Paffenhöfer, 1996; Strickler, 1982; Yen and Strickler, 1996), planar Particle Image Velocimetry (PIV) (Stamhuis and Videler, 1995; van Duren et al., 1998, 2003; Stamhuis et al., 2002; van Duren and Videler, 2003; Yen et al., 2003; Katija and Dabiri, 2008), and three-dimensional digital holography (Malkiel et al., 2003; Sheng et al., 2007). Schlieren optics and micro-cinematography will not be discussed in detail because these methods do not produce a quantified velocity field.

For particle tracking, individual neutrally-buoyant particles are spatially tracked in a fluid to obtain velocity measurements. The particles can be tracked in three-dimensions using two orthogonally placed cameras (e.g., Tiselius and Jonsson, 1990; Fields and Yen, 1997). The displacement of the particle is measured in both camera views and divided by the time difference between the images. Particle paths may be discarded because particles cross in and out of the field view (Tiselius and Jonsson, 1990). As a result, the velocity fields obtained by particle tracking are often sparse (Yen et al., 1991; Tiselius and Jonsson, 1990; Fields and Yen, 1993; Yen and Strickler, 1996), which leads to inaccuracies in secondary calculations. Since the velocity field measurements are extremely tedious, replicate flow fields are rarely obtained, and this constrains the analysis of the data.

The Particle Image Velocimetry (PIV) method is similar to particle tracking but the resulting velocity fields are more uniform and amenable to further data analysis. PIV is a fluid visualization method that measures the displacement of reflective, neutrally-buoyant particles over a discrete time period (Adrian, 1991; Raffel et al., 1998). Instead of tracking an individual particle, as in particle tracking, the field of view is discretized into interrogation subwindows and the displacement of groups of particles is calculated between image pairs. The particle displacement is determined by finding the peak value of the cross-correlation function relative to the center of the subwindow. Hence, the velocity obtained for each interrogation subwindow is an average velocity over the group of particles rather than an isolated particle velocity. The velocity vectors obtained from the PIV analysis are often filtered and smoothed to eliminate spurious data points (Westerweel, 1994). The main limitation of PIV is that most PIV systems are two-dimensional, and three-dimensional flow structures are difficult to quantify with these systems.

Ultimately, three-dimensional velocity fields are required to fully describe the hydrodynamic disturbances of zooplankton. Scanning PIV and stereo PIV are two types of three-dimensional PIV systems that have recently been used to measure the flow around larger aquatic organisms (Lauder and Madden, 2008). In scanning PIV, the planar laser sheet is scanned over thin slices of a three-dimensional volume to produce a nearly-instantaneous three-dimensional flow field. Scanning PIV systems may work better for larger aquatic organisms rather than the small copepods as the laser sheet width is nearly the same as the width of the copepod body for smaller species. Stereo PIV produces three-dimensional velocity vectors in the measurement plane by placing two

cameras in an off-perpendicular configuration. Stereo PIV is an improvement over traditional two-dimensional systems, but requires additional equipment and unique software. Digital holography is another three-dimensional flow visualization method that has been successfully applied to zooplankton (Malkiel et al., 2003; Sheng et al., 2007). A digital hologram is generated of the test specimen along with the seeded particles. A time-consuming and complicated numerical reconstruction is required to subsequently produce the velocity fields. Overall, the resolution of the velocity field appears to be much lower with digital holography compared to PIV (Malkiel et al., 2003).

In situ measurements of animal flow fields are ideal and only recently have researchers collected flow fields from zooplankton in the ocean (Katija and Dabiri, 2008). The underwater, planar PIV system developed by Katija and Dabiri (2008) uses suspended, marine particles as the seeding particles to estimate the ambient fluid velocity and the flow field generated by jellyfish. This system provides more ecologically relevant data than laboratory based PIV systems; however, the use of a green laser would initiate an escape response in other zooplankton and the resolution of the system is not fine enough to be applied to copepod flow fields.

2.2.2 Copepod flow fields

The majority of studies on copepod flow fields have been quantified around tethered copepods because the data collection of free-swimming organisms is tedious and costly. Past research on tethered and free-swimming copepod flow fields and previous data on *Euchaeta rimana* flow fields are discussed below. It is important to note that the

flow fields around the species *E. antarctica* and *E. elongata* have not been measured by any method prior to this study.

2.2.2.1 Tethered versus free-swimming flow fields

Particle paths, velocity fields, and vorticity fields have been collected on tethered and free-swimming copepods (Table 2.2). The majority of flow field data has been collected on tethered *Temora longicornis*, *Euchaeta rimana*, and *Centropages* sp. The maximum fluid velocity in the flow fields ranged from 0.08 to 2.5 cm s^{-1} and varied between species and with visualization method. The spatial extent of the fluid disturbance was estimated as the maximum distance of the fluid disturbance into the ambient fluid measured from the front of the antennae (Table 2.2). The maximum distance ranged from 0.1 to 0.4 cm and also varied greatly between species and measurement technique. Based on the data in Table 2.2, there is no discernable difference in the flow fields of tethered and free-swimming copepods.

A comparison between untethered and tethered larvae showed that the flow pattern is altered by the presence of the tether (Emlet, 1990). Emlet (1990) noted that the volume of fluid entrained from upstream of the tethered larvae was greater than for the untethered case. The magnitude and location of high velocity regions are different in tethered versus untethered larvae and copepods (Emlet, 1990; Bundy and Paffenhöfer, 1996). In addition to the physical differences in the flow field, organism behavior is also potentially modified by the presence of the tether. Hwang et al. (1993) found similar mean time allocation habits of tethered copepods compared to untethered copepods, but there was a significant difference in the individual variability. Despite the widespread acknowledgement that tethering alters the flow fields of zooplankton, studies are still

performed with tethered specimens. To date, there has not been a high resolution comparison between the flow fields of tethered and free-swimming copepod.

Table 2.2 Summary of reported copepod flow field data. Values listed as mean ± standard deviation unless otherwise noted

Species	Method	Specimen position	Maximum velocity of the flow (cm s^{-1})	Distance of flow disturbance in front of first antennae (cm)	Source
Eucalanus crassus	Particle tracking	Free swimming	0.2	0.15	Strickler (1982)
Paracalanus parvus	Particle tracking	Free swimming	0.4	0.3	Tiselius and Jonsson (1990)
Pseudocalanus elongates	Particle tracking	Free swimming	0.5	0.5	Tiselius and Jonsson (1990)
Temora longicornis	Particle tracking	Free swimming	0.8	0.8	Tiselius and Jonsson (1990)
Centropages typicus	Particle tracking	Free swimming	0.8	1.0	Tiselius and Jonsson (1990)
Centropages hamatus	Particle tracking	Free swimming	1.0	1.0	Tiselius and Jonsson (1990)
Euchaeta rimana	Particle tracking	Free swimming	0.45	0.2	Yen et al. (1991)
Pleuromamma xiphias	Particle tracking	Tethered	2.5	0.3	Fields and Yen (1993)
Euchaeta rimana	Particle tracking	Tethered	0.8	-	Lenz and Yen (1993)
Temora longicornis	PIV	Tethered	N/A	0.1	Stamhuis and Videler (1995)
Centropages velificatus	Particle tracking	Tethered	1.8	0.15	Bundy and Paffenhoefer (1996)
Paracalanus aculeatus	Particle tracking	Tethered	0.08	0.05-0.1	Bundy and Paffenhoefer (1996)
Euchaeta rimana	Schlieren	Tethered	2.0	0.1	Yen and Strickler (1996)
Euchaeta rimana	Particle tracking	Tethered	1.0	0.15	Fields and Yen (1997b)
Temora longicornis	PIV	Tethered	1.15 (escaping) 0.25 (feeding)	-	van Duren et al. (1998)
Euchaeta rimana	Particle tracking	Tethered	0.7	0.2	Moore et al. (1999)
Pleromamma xiphias	Particle tracking	Tethered	0.8	0.4	Moore et al. (1999)

Table 2.2 (Continued)

Species	Method	Specimen position	Maximum velocity of the flow (cm s^{-1})	Distance of flow disturbance in front of first antennae (cm)	Source
Temora longicornis	PIV	Tethered	2.1	0.04	Stamhuis et al. (2002)
Diaptomus minutus	Digital holography	Free swimming	0.35	0.15	Malkiel et al. (2003)
Temora longicornis	Particle tracking and PIV	Tethered	0.84	0.15	van Duren et al. (2006)

2.2.2.2 *Euchaeta rimana* cruising flow fields

Since this study is on copepods of the genus *Euchaeta,* this discussion will focus on the flow fields of *E. rimana*. The cruising flow field is generated by the beating of the second antennae or cephalic appendages. A maximum fluid velocity of 0.5 cm s^{-1} (free-swimming specimen) – 2.0 cm s^{-1} (tethered specimen) is located in the region of the second antennae where the fluid converges (Yen et al., 1991; Yen and Strickler, 1996). The vorticity is greatest (2 s^{-1} (free-swimming) – 8 s^{-1} (tethered)) adjacent to the cephalic appendages and extending to the midline of the front antennae (Yen et al., 1991; Fields and Yen, 1997b). Based on previous studies, tethering of the copepod results in increased velocity and vorticity values.

E. rimana prey exhibit an escape response at a distance of 0.7 mm from the front antennae (Doall et al., 2002). The fluid disturbance in front of *E. rimana* is limited to a distance of 1.5 mm – 2.0 mm (Fields and Yen, 1997b; Moore et al., 1999). The velocity value corresponding to a distance of 0.7 mm in front of the first antennae is approximately 3 mm s^{-1} (Fields and Yen, 1997b). Yen (1988) observed that *E. rimana* lunge at prey after the prey has initiated an escape response. *E. rimana* may be minimizing the hydrodynamic disturbance in front of the first antennae to a distance where prey capture is successful. The fluid velocity decreases to ambient values at the distal tips of the first antennae where the long setae are located (Lenz and Yen, 1993; Yen and Strickler, 1996; Fields and Yen, 1997b). Lenz and Yen (1993) suggest that the long setae at the distal tips are ideal for predator detection and benefit from being removed from the fluid movement associated with the swimming behavior. Thus, the

flow fields of cruising copepods have limited frontal extent to reduce conspicuousness to prey and maintain maximal rheotactic sensitivity.

2.2.2.3 *Euchaeta rimana* escape flow fields

The flow field of an escaping copepod consists of a series of vortices produced by jets of fluid produced by each copepod jump (Yen and Strickler, 1996; Yen, 2000). From Schlieren visualizations, toroidal vortices are shed by escaping *E. rimana* at a frequency of 30 – 100 Hz (Yen and Strickler, 1996). The volume of the escape vortex increased from 0.4 to 1.0 ml over a 35 ms time period. The toroid speed decreases from an initial value of approximately 30 mm s^{-1} to 6 mm s^{-1} in a 0.37 second time period.

2.2.3 Krill Flow Fields

2.2.3.1 *Euphausia pacifica* flow fields

The flow field generated by a swimming *Euphausia pacifica* has been quantified with PIV using tethered specimens (Yen et al., 2003). This study found that Pacific krill generated a downward and rear-directed jet with maximum, time-averaged velocities below the pleopods of 4.9 ± 1.1 cm s^{-1}. The fluid was entrained from below the krill into the pleopod region and then ejected into the propulsion jet. The regions of highest vorticity were located along the shear layers of the jet. The extent of the fluid region disturbed by the krill was 18 times larger than the area of its body. The hydromechanical cue for the tethered specimen was available to neighboring krill along the axis of the jet at a distance of less than two body lengths. In the transverse direction, the width of the hydromechanical cue was much less than one body length (0.23 cm). Yen et al. (2003) suggested that the jet was narrower and smaller in spatial extent in preliminary data on free-swimming specimens. We expect that the presence of the tether altered the flow in

meaningful ways and it is important to look at the flow fields of free-swimming krill to assess the natural cue structure.

2.2.3.2 *Euphausia superba* flow fields

The flow field produced by a tethered *Euphausia superba* has been visualized using a particle tracking method (Ebina and Miki, 1996). The reported data consisted of frequency of unsteadiness rather than velocity. The average frequency content of the flow fields was 4.21 ± 0.62 Hz and the flow fields extended to a length of 16 cm behind the animal (Ebina and Miki, 1996). Velocity, vorticity, and strain rate fields were not obtained using this method and remain unknown for *E. superba.*

Previous researchers have used the flow fields around a smaller species, *Meganyctiphanes norvegica* to investigate hydromechanical cues associated with *E. superba* (Kils, 1982; Patria and Wiese, 2004). Low resolution measurements via particle tracking showed that the flow field of a tethered *M. norvegica* is a downward-directed jet at an angle of 40 degrees (Kils, 1982). The propulsion jet has a maximum velocity of 10 cm s^{-1} at the swimmerets and the jet shear layers formed distinct vortices with diameters of 7 cm (Patria and Wiese, 2004). The velocity field was not well characterized in either study due to the methodological constraints of manual particle tracking and the use of a tethered specimen. Further, these studies provided minimal information about the vorticity, strain rate, and dissipation rate fields.

2.3 Hydromechanical cue

In many cases, visual sensory organs are absent in zooplankton and these organisms rely on hydromechanical cues rather than vision to escape predation (Visser,

2001). An understanding of the fluid disturbances generated and sensed by zooplankton allows us to understand how these organisms interact with each other. In the following sections, we will provide an overview of hydromechanical cues of two types of zooplankton: krill and copepods.

2.3.1 Copepod hydromechanical cues

2.3.1.1 Copepod sensory systems

Copepods sense their prey and predators using an array of setae on the first antennae that are sensitive to fluid disturbances (Lenz and Yen, 1993). The mechanoreceptive setae can detect fluid velocities as small as 20 $\mu m\ s^{-1}$. Elongated pairs of setae are arranged at 90° angles on the first antennae to sense fluid disturbances in three orthogonal planes (Yen and Nicoll, 1990). These pairs of setae are located on the distal tips of the antennae and the seventh and eight antennule segments (middle of the antennae) (Yen and Nicoll, 1990). The fluid surrounding the elongated setae at the distal tips is minimally disturbed by the hydrodynamic disturbance and well positioned to sense the hydrodynamic disturbances of predators and prey (Lenz and Yen, 1993). Further, the non-feeding males of *E. rimana* have lost the elongated pairs of setae and do not need to accurately detect prey (Yen, 1988). Conversely, the proximal section of the antennae experiences the largest velocities during locomotion and the setae are short and abundant in this region (Lenz and Yen, 1993). According to Kiørboe et al. (1999), the setal bending pattern depends on the type of fluid deformation rate the setae are exposed to such as fluid acceleration, vorticity, and deformation rate. The longer setae at the distal tips are better positioned to sense these fluid disturbance quantities than the shorter setae near the head.

2.3.1.2 Structure of the hydromechanical cue

This section reviews the fluid quantities that have been identified as eliciting a behavioral response in copepods. Copepods have been observed to initiate a capture response after contact with a hydrodynamic disturbance (Fields and Yen, 2002), but the more commonly observed response is an escape. Copepods exhibit an escape response when exposed to artificial hydrodynamic disturbances and the fluid disturbances generated by other copepods (Table 2.3). The escape response of an adult copepod is initiated by a threshold level of relative velocity, shear, or deformation rate (Table 2.3). Several studies have looked at the escape response in terms of distance from the predator (e.g., Doall et al., 2002; Viitasalo et al., 1998), but these studies did not directly measure the flow field of the predator so these studies were not included in this discussion.

The threshold values of copepod escape responses to the flow fields of predators have been determined in experiments with artificial hydrodynamic disturbances generated with siphons, oscillating cylinders, and small jets (Table 2.3). Kiørboe et al. (1999) performed a comprehensive study with siphon flow, an oscillating chamber, Couette device, and a rotating cylinder to determine the least varying fluid quantity that elicited copepod escapes. The siphon flow and Couette device consistently initiated behavioral responses that were associated with linear and shear deformation rates. The maximum deformation rate is the absolute value of the largest principal component of the deformation rate tensor, which is a tensor composed of both linear and shear deformation rates. The maximum deformation rate (Δ) at a point in the siphon flow is calculated from the theoretical flow predication:

$$\Delta = \frac{Q}{2\pi r^3} \tag{2.1}$$

where Q is the flow rate in the siphon and r is the distance from the siphon (Kiørboe et al., 1999; Burdick et al., 2007). The maximum deformation rate is estimated for the oscillating cylinder flow from the following equation:

$$\Delta = \frac{2a^2U}{r^3} \tag{2.2}$$

In this case, fluid deformation rate is the function of the radius of the bar (a), bar velocity (U), and radial distance from the bar (r) (Buskey et al., 2007). Fields and Yen (2002) elicited an escape response with a fluid jet where only the velocity magnitude was known rather than the deformation rate or other quantities.

Kiørboe and Visser (1999) hypothesized that the pertinent cue for prey is the product of the deformation rate and the length of the prey. However, Kiørboe et al. (1999) found that variation of the cue strength among species was much greater than the variation of the maximum deformation rate, which suggests unique sensory capabilities and behavior among species. When comparing the reported threshold values, the minimum value of the maximum deformation rate is approximately 0.4 s^{-1} (Table 2.3). The largest value of maximum deformation rate value that has been observed in the flow fields of the feeding currents of copepods ranges from 4.8 to 16.7 s^{-1} (reviewed in Kiørboe et al., 1999). These values are significantly greater than the behavioral threshold value, which suggest that prey entrained in the feeding currents will perform an escape behavior.

Table 2.3 Summary of reported thresholds of adult copepod escapes response to fluid flow stimuli. Mean threshold value reported unless noted otherwise.

Species	Fluid stimulus	Response distance (mm)	Fluid variable	Threshold value	Source
Acartia hudsonica nauplii	Tethered *Temora longicornis*	0.8 – 2.2	Relative velocity	0.74 mm s^{-1}	Yen and Fields (1992)
Labidocera madurae	Siphon	0.86	Shear Deformation rate	51.1 s^{-1} 6.3 s^{-1}	Fields and Yen (1997a)[1]
Acartia tonsa	Siphon	0.28	Shear Deformation rate	1.5 s^{-1} 0.38 s^{-1}	Fields and Yen (1997a)[1]
Euchaeta rimana	Siphon	1.18	Shear Deformation rate	4.1 s^{-1} 2.4 s^{-1}	Fields and Yen (1997a)[1]
Pleuromamma xiphias	Siphon	0.95	Shear Deformation rate	7.2 s^{-1} 4.6 s^{-1}	Fields and Yen (1997a)[1]
Oithona similus	Siphon	0.13	Shear Deformation rate	8.1 s^{-1} 3.8 s^{-1}	Fields and Yen (1997a)[1]
Eurytemora affinis	Pipette jet	0.53	Deformation rate	1.9	Viitasalo et al. (1998)[1]
Temora longicornis	Pipette jet	0.35	Deformation rate	6.5	Viitasalo et al. (1998)[1]
Temora longicornis nauplii	Siphon flow	-	Deformation rate	0.81 s^{-1}	Titelman (2001)
Euchaeta rimana	Pipette jet	2.6	Jet velocity	200 mm s^{-1}	Fields and Yen (2002)
Acartia hudsonica	Siphon flow	3.8	Deformation rate	2.2 s^{-1}	Burdick et al. (2007)
Temora longicornis	Siphon flow	3.7	Deformation rate	2.7 s^{-1}	Burdick et al. (2007)
Tortanus discadatus	Siphon flow	7.3	Deformation rate	0.3 s^{-1}	Burdick et al. (2007)
Centropages hamatus	Siphon flow	4.9	Deformation rate	1.2 s^{-1}	Burdick et al. (2007)
Acartia hudsonica	Oscillating bar	6.1	Deformation rate	1.7 s^{-1}	Burdick et al. (2007)
Temora longicornis	Oscillating bar	< 3	Deformation rate	>15 s^{-1}	Burdick et al. (2007)
Tortanus discadatus	Oscillating bar	7.0	Deformation rate	1.2 s^{-1}	Burdick et al. (2007)

Table 2.3 (Continued)

Species	Fluid stimulus	Response distance (mm)	Fluid variable	Threshold value	Source
Centropages hamatus	Oscillating bar	6.5	Deformation rate	1.4 s^{-1}	Burdick et al. (2007)
Temora turbinata	Siphon	2.1 – 2.8	Deformation rate	3.93 s^{-1}	Waggett and Buskey (2007)
Paracalanus parvus	Siphon	2.4 – 3.1	Deformation rate	6.16 s^{-1}	Waggett and Buskey (2007)

[1] Deformation rate values recalculated and presented in study by Kiørboe et al. (1999).

The discussion above relates to the fluid cue that copepod prey sense from predators. Kiørboe and Visser (1999) suggest that the cue that copepod predators use to detect prey is the absolute velocity magnitude. The threshold value for the capture response in *E. rimana* is 2.0 cm s^{-1}(Fields and Yen, 2002). From the previous flow field velocity data (Table 2.2), a copepod predator would be unable to detect the flow fields of many of the potential prey species at a velocity threshold of 2.0 cm s^{-1}.

Copepod nauplii also exhibit escape behavior (Yen and Fields, 1992; Titelman, 2001). In a study of the escape response of copepod nauplii to live predators, the fluid quantity defined as the relative velocity was identified as the least varying fluid quantity that produced an escape response in the flow field of *Temora longicornis* (Yen and Fields, 1992). Relative velocity was identified as the ratio of the nauplii swimming velocity to the ambient fluid velocity.

2.3.2 Krill hydromechanical cues

2.3.2.1 *E. superba* schooling behavior

The characteristics of *E. superba* schools have been well documented, whereas very little information exists on swarms of *E. pacifica*. Thus, the following discussion on schooling behavior will be limited to *E. superba.*

Schools of *E. superba* occur in densities of 20,000 to 30,000 krill per cubic meter (Hamner, 1984). Large layers of *E. superba* have been documented and these layers consist of small schools in close proximity to each other (Watkins and Murray, 1998). The krill within a school are the same size and at the same developmental stage (Watkins and Murray, 1998; Hamner and Hamner, 2000; Hamner et al., 1983). Within a school,

the nearest neighbor distances range from 0.5 to 3 krill body lengths (O'Brien, 1989; Kawaguchi et al., in press). Individuals within a school are never located directly below or above their neighbors instead they prefer an orientation alongside their neighbor.

Krill individuals are suspected to maintain their positions within the school by responding to the hydromechanical cues of nearby krill (Hamner, 1984; Wiese and Ebina, 1995), despite the fact that schooling behavior in the laboratory has been disrupted by low light levels and is non-existent with blinded krill (Strand and Hamner, 1990; Kawaguchi et al., in press). Buskey (2000) found that mysids, a similar type of zooplankton, school only during daylight hours and behaviorally respond to a moving visual cue, which further suggests that visual cues may be important in schooling. Schools of *E. superba* actively avoid visual stimuli within a tank and are only successful at schooling in white tanks (Strand and Hamner, 1990). However, krill were unable to school in uniform, ambient flow conditions or sudden disruptions of flow which suggests that hydromechanical cues also are used during schooling behavior.

2.3.2.2 Sensory cues

Krill are equipped with both vertical and horizontal deflecting flagella on each antennule. Each flagella is lined with both smooth and feathered hair-typed sensilla that sense high frequency hydrodynamic disturbances (Patria and Wiese, 2004). The threshold fluid velocity for krill antennae is approximately 0.25 mm s^{-1} at frequencies in the range 5 – 40 Hz for *Meganyctiphanes norvegica (*Patria and Wiese, 2004), and 0.15 mm s^{-1} in the same frequency range for *Euphausia superba* (Wiese and Marschall, 1990). The pleopod beat frequency of *E. superba* is in the range 3.5 – 5 Hz (Wiese and Ebina, 1995) and pressure pulses have been measured in the flow field of *E. superba* at 4 Hz

(Wiese and Ebina, 1995; Ebina and Miki, 1996). Based on frequency content, Ebina and Miki (1996) found that the flow field of *E. superba* extended 16 cm behind the animal. The spatial extent of the *E. pacifica* flow field is less than two body lengths to the rear and 0.2 cm in the transverse direction for a velocity limit of 0.5 mm s^{-1} (Yen et al., 2003). Given the sensitivity of the antennae in the frequency range and fluid velocity characteristic of krill flow fields, it is possible that the flow disturbance of krill may be used by conspecifics as a sensory cue.

2.4 Cost of propulsion

2.4.1 Propulsion analysis from flow fields

Researchers have been interested in estimating the cost of propulsion for aquatic organisms for many decades. With accurately quantified costs of propulsion, the ecological consequences of motility and foraging can be assessed and placed into an ecological framework. Several methods have been employed to estimate the energetic costs including measurements of the oxygen consumption rate, calculations of the locomotor force from vorticity field dynamics, and measurement of the viscous dissipation rate of kinetic energy.

Oxygen consumption rate, or respiration rate, data are collected in a calibrated respirometer, which measures the concentration of oxygen in the experimental chamber. The oxygen consumption rate is recorded as the volume or mass of oxygen consumed per gram of dry weight per hour. Early studies on respiration rate used confined chambers, and more recent studies have been performed in chambers that allow organisms to swim freely (Cekunova et al., 1974, McWhinnie et al., 1964; Swadling et al., 2005).

Propulsion costs have been measured directly from PIV-generated velocity fields for many species of fish (Tytell, 2006; Epps and Techet, 2007; Peng and Dabiri, 2007; Peng et al., 2007) and jellyfish (Dabiri, 2005). Dabiri (2005) proposed a method to use two dimensional PIV images to calculate the locomotive forces. First, the propulsive force **F** that an animal exerts onto a fluid can be estimated by the following equation:

$$\mathbf{F} = \rho \frac{\partial}{\partial t} \int (\mathbf{x} \times \boldsymbol{\omega}) dV_V + \rho \frac{\partial}{\partial t} \int \phi \mathbf{n} dS_V \tag{2.3}$$

where the ρ is the fluid density, **x** is a position vector, V_V is the volume, and S_V is the surface of the wake vortex. The calculation of the vorticity field ($\boldsymbol{\omega}$) from the velocity vector **u** is shown in Equation 2.4.

$$\boldsymbol{\omega} = \nabla \times \mathbf{u} = \left(\frac{\partial w}{\partial y} - \frac{\partial v}{\partial z} \right) \mathbf{i} - \left(\frac{\partial w}{\partial x} - \frac{\partial u}{\partial z} \right) \mathbf{j} + \left(\frac{\partial v}{\partial x} - \frac{\partial u}{\partial y} \right) \mathbf{k} \tag{2.4}$$

The first term of Equation 2.3 is the mathematical description of the generation and growth of the vorticity field. The vorticity in the flow disturbance can be approximated as a thin vortex loop of area (A) and circulation (Γ) (Equation 2.5).

$$\rho \frac{\partial}{\partial t} \int (\mathbf{x} \times \boldsymbol{\omega}) dV_V \approx \rho \frac{d}{dt} (A\Gamma) \tag{2.5}$$

The second term of Equation 2.3 is the surface integral of the velocity potential (ϕ) and the term concerns the added-mass effect or the resistance of the vortex in the fluid medium. This term can be approximated by a term including the added mass coefficient

(c_{ii}), vortex volume ($\Omega_V \approx SA$), and the wake vortex velocity in the *i*-direction ($\mathbf{U}_{Vi}$) (Equation 2.6).

$$\rho \frac{\partial}{\partial t} \int \phi \mathbf{n} dS_V \approx \rho c_{ii} \frac{d}{dt} (\Omega_V \mathbf{U}_{Vi}) \tag{2.6}$$

A new equation to calculate the propulsive force (Equation 2.7) is created by combining Equation 2.3 with Equations 2.5 and 2.6.

$$F \approx \rho \frac{d}{dt} (A\Gamma + \bar{c}_{ii} AS\mathbf{U}_{Vi}) \tag{2.7}$$

To calculate the locomotive force with instantaneous velocity fields collected at discrete time points (t_o and t_1), the following equation is used:

$$F(t_0) \approx \frac{\rho\{[A(t_1)\Gamma(t_1) + \bar{c}_{ii} A(t_1)S(t_1)\mathbf{U}_{Vi}(t_1)] - [A(t_0)\Gamma(t_0) + \bar{c}_{ii} A(t_0)S(t_0)\mathbf{U}_{Vi}(t_0)]\}}{\Delta t} \tag{2.8}$$

The underlying assumptions of this equation are that the animal swims at a constant velocity, the fluid is inviscid prior to wake formation, and the flow disturbance contains an isolated vortex. In the case of cruising copepods and krill, the flow disturbances do not consist of an isolated vortex, and this analysis cannot be used to estimate the propulsion costs. However, this analysis may be useful to examine the hydrodynamic disturbances of escaping copepods.

Another method used to calculate the energy dissipated into the fluid is the viscous dissipation rate of kinetic energy. The rate of energy dissipation due to viscosity, Ψ, is defined as (e.g., Schlichting and Gersten, 2000):

$$\Psi = \mu \left[\begin{array}{l} 2\left(\frac{\partial u_x}{\partial x}\right)^2 + 2\left(\frac{\partial u_y}{\partial y}\right)^2 + 2\left(\frac{\partial u_z}{\partial z}\right)^2 \\ + \left(\frac{\partial u_x}{\partial y} + \frac{\partial u_y}{\partial x}\right)^2 + \left(\frac{\partial u_x}{\partial z} + \frac{\partial u_z}{\partial x}\right)^2 + \left(\frac{\partial u_y}{\partial z} + \frac{\partial u_z}{\partial y}\right)^2 \end{array} \right] \tag{2.9}$$

Since most PIV flow fields are planar, the *z*-direction velocity component and spatial derivatives can not be calculated. The $\partial u_z / \partial z$ term can be estimated using the incompressible continuity equation:

$$\frac{\partial u_z}{\partial z} = -\frac{\partial u_x}{\partial x} - \frac{\partial u_y}{\partial y} \tag{2.10}$$

The *z*-direction spatial derivatives can be approximated as equal to the *x*-direction and *y*-direction derivatives:

$$\left(\frac{du_x}{dz} + \frac{du_z}{dx}\right)^2 \approx \left(\frac{du_x}{dy} + \frac{du_y}{dx}\right)^2 \text{ and } \left(\frac{du_y}{dz} + \frac{du_z}{dy}\right)^2 \approx \left(\frac{du_x}{dy} + \frac{du_y}{dx}\right)^2 \tag{2.11}$$

Therefore, the energy dissipation rate approximated in terms of the gradients calculated in the x - y plane is:

$$\Psi = \mu \left[2\left(\frac{\partial u_x}{\partial x}\right)^2 + 2\left(\frac{\partial u_y}{\partial y}\right)^2 + 2\left(-\frac{\partial u_x}{\partial x} - \frac{du_y}{dy}\right)^2 + 3\left(\frac{\partial u_x}{\partial y} + \frac{\partial u_y}{\partial x}\right)^2 \right] \tag{2.12}$$

van Duren et al. (2003) used this method to approximate the energy cost of the feeding current of the copepod *T. longicornis.*

2.4.2 Copepod propulsion costs

For copepods, the total oxygen consumption rate has been measured for several species of copepod (*Temora longicornis, Mesocyclops brasilianus, Oithona similis, Centropages hamatus*, and *Labidocera aestiva)* but has not been calculated for any *Euchaeta* species (Berner, 1962; Epp, 1979; Nakamura and Turner, 1997). For these other species, the estimates of power range from 1×10^{-7} to 1×10^{-8} W (reviewed in van Duren et al., 2003). Van Duren et al. (2003) calculated the power from PIV fields with the viscous dissipation rate as 6.6×10^{-11} W to 2.3×10^{-10} W. After taking into account mechanical efficiency and muscle efficiency, the power requirements were 1.6×10^{-9} W. Since oxygen consumption rate often measures the oxygen consumption needed for metabolic processes other than propulsion, the propulsion estimates obtained from flow fields may be lower than the power estimates from oxygen consumption rates. The amount of viscous energy dissipated by a cruising *Euchaeta rimana* copepod was estimated at 9.3×10^{-10} W (Yen et al., 1991). Based on these values, the propulsion costs are expected to be around 10^{-10} to 10^{-11} W for copepods.

2.4.3 Krill propulsion costs

The propulsion costs of both *E. pacifica* and *E. superba* have been measured with the oxygen consumption rate or respiration rate method. Respiration rates of euphausiids have been compared between species, temperature, and body size. The oxygen consumption rate has been quantified for both species of krill used in this study. Early studies on the oxygen respiration rates of *E. superba* in confined chambers found respiration rates ranging from 0.36 – 1.5 mg O_2 g_d^{-1} h^{-1} (Cekunova et al., 1974;

McWhinnie et al., 1964). The respiration rates of *E. pacifica* are similar and range between 0.70 – 3.64 mg O_2 g_d^{-1} h^{-1} (Lasker, 1966). The pattern of oxygen consumption of krill subjected to increasing water temperatures differed between species. Increased oxygen consumption was associated with an increase in water temperature in the temperate species *E. pacifica,* whereas oxygen consumption decreased with increased water temperature in the polar species *E. superba* (Small, 1967a; McWhinnie et al., 1964). Small (1967b) hypothesized that *E. pacifica* receive an energetic boost by performing diel vertical migration by increasing the time spent at a colder temperature where oxygen consumption was lower. In contrast, *E. superba* exists in an environment with less temperature stratification and the individuals acclimate their metabolism to different temperatures rather than gaining any energetic advantage from the temperature difference (McWhinnie et al., 1964). As for the effect of body size on respiration, the respiration rates of *E. pacifica* increase from January to June as a result of the increase in size of this species during this period (Small, 1967a). Kils (1982) found that energy expended during hovering increases with body size such that a 60 mm krill will need 61 times higher metabolism than a 5 mm krill. In sum, the increased body size between *E. pacifica* and *E. superba* should increase the oxygen consumption rate but that difference is not well resolved in direct studies of the different species.

The above mentioned studies could not quantify the effect of swimming speed on oxygen consumption due to use of a small, confined testing chamber. Kils (1979) found that the respiration rates were increased by 40% when performed in testing apparatus that allowed *E. superba* to swim freely (average krill swimming speed of 6 cm s^{-1}). Torres and Childress (1983) found that respiration rate increased linearly with swimming speed.

In addition, the respiration rates of *E. superba* increased four fold by increasing current speeds from 3 cm s^{-1} to 17 cm s^{-1} (Swadling et al., 2005). The energetic cost of transport in *E. superba* was estimated to range 73% of total metabolic expenditure (Swadling et al., 2005).

The benefit of reduced energy expenditure of schools has been showed by a decreased oxygen uptake in schools and swarms compared to oxygen uptake of solitary individuals in fish (Parker, 1975) and mysids (Ritz, 2000). In contrast to these studies, oxygen uptake of individuals of *E. superba* is similar to the oxygen uptake of the krill in groups (Swadling et al., 2005). The costs of increased disease transmission and reduced nutrient availability have been refuted by observations of krill schools in the ocean. Unhealthy krill tend to aggregate at the back of schools and are left behind when they are too weak to swim with the group (Hamner, 1984). Also, krill schools are narrow in one direction in order to allow transfer of oxygen and other nutrients to all individuals within the group (Hamner et al., 1983; Hamner and Hamner, 2000). In general, it appears that groups of krill benefit from forming aggregations, but research has not shown that schools provide a specific benefit over swarms.

2.5 Contributions of the current research

Previous research has quantified some aspects of zooplankton swimming behavior, flow fields, hydromechanical cues, and propulsion. However, these studies do not provide simultaneous laboratory measurements of swimming behavior along with high resolution flow field analysis. In addition, flow fields have not been collected of free-swimming *E. elongata, E. antarctica*, *E. pacifica*, or *E. superba.* The aims of the

current study are to simultaneously quantify the swimming behavior of these species and the resulting fluid disturbances. The experimental setup provides a unique means of quantifying the flow fields around a free-swimming zooplankton to address these objectives. Unlike other PIV systems, the infrared laser does not induce a behavioral response in zooplankton due to avoidance or attraction to the laser light. Further, the ability to capture high resolution velocity fields around free-swimming zooplankton is an improvement over previous research.

CHAPTER 3

QUANTITATIVE ANALYSIS OF TETHERED AND FREE-SWIMMING COPEPODID FLOW FIELDS

3.1 Summary

We quantified the flow field generated by tethered and free-swimming *Euchaeta antarctica* using the particle image velocimetry (PIV) technique. The streamlines around the free-swimming specimens were generally parallel to the body axis, whereas the streamlines around all of the tethered copepodids demonstrated increased curvature. Differences noted in the streamline pattern, and hence the vorticity, dissipation rate, and strain rate fields, are explained by considering the forces on the free-swimming specimen compared to the tethered specimen. Viscous flow theory demonstrates that the force on the fluid due to the presence of the tether irrevocably modifies the flow field in a manner that is consistent with the measurements. Hence, analysis of the flow field and all associated calculations differ for tethered versus free-swimming conditions. Consideration of the flow field of the free-swimming predatory copepodid shows the intensity of the biologically-generated flow and the extent of the mechanoreceptive cue quantified in terms of shear strain rate. The area in the dorso-ventral view surrounded by the 0.5 s^{-1} contour of e_{xy}, which is a likely threshold to induce an escape response, is 11 times the area of the exoskeletal form for the free-swimming case. Thus,

mechanoreceptive predators will perceive a more spatially-extended cue than the body size.

3.2 Introduction

One of the critical aspects of understanding the interaction between aquatic organisms and their surrounding fluid environment is the accurate quantification of flow fields created during feeding and locomotion. For instance, properly quantifying the flow field facilitates calculating the external forces created by animal propulsion (e.g., Drucker and Lauder, 2002), the energetic costs of feeding and locomotion (e.g., Stamhuis et al., 2002), and the flow disturbance created by organism motion (e.g., Yen and Fields, 1992). Flow fields generated by copepods are of particular interest because of the ecological significance of the interaction with other organisms. The flow field around a copepod is a complex structure comprised of an anterior feeding current and a lateral and ventral propulsive current (Fields and Yen, 1993). A strong anterior feeding current can maximize intake volume to the feeding appendages, as might be needed by a particle feeding plankter. It follows that accurate estimates of volume processed in the feeding current are useful to assess feeding rates and ultimately the impact of copepod grazing on trophic energy transfer in planktonic communities. Alternatively, a predatory copepod may construct a feeding current with a weaker velocity gradient so as not to reveal its presence to rheotactic prey (Yen and Strickler, 1996). Thus, crypsis of the predator from its prey may be an important mechanism in determining predation success. When generating the propulsive current, trimming of the wake can be useful when hiding from

mechanoreceptive predators (e.g., fish: Coombs et al., 1988) or when creating a minimally disturbed trail of the pheromone needed to attract a mate (Yen et al., 1998).

Because of the interest in visualizing and quantifying the flow fields created by copepods, several methods have been employed in recent decades: Schlieren optics (Strickler, 1977), high-speed micro-cinematography (Alcaraz et al., 1980; Koehl and Strickler, 1981; Strickler, 1982; Gallager, 1993), manual particle tracking (Yen et al., 1991; Yen and Fields, 1992; Fields and Yen, 1993; Bundy and Paffenhöfer, 1996), planar Particle Image Velocimetry (PIV) (van Duren et al., 1998, 2003; Stamhuis et al., 2002; van Duren and Videler, 2003), and three-dimensional digital holography (Malkiel et al., 2003). Because copepods are (generally) small, visualization of the flow field created by copepods requires high resolution. As a result, copepods are often tethered in order to maintain a fixed position within the small field of view during flow visualization. In the majority of the studies listed above, the copepod was tethered during the flow visualization process. Researchers generally acknowledge the distortion of the flow field induced by tethering the organism but tethering is often considered a necessary step for acquiring flow field data. For instance, during PIV measurements the copepod and surrounding fluid must be imaged when the body position coincides with a thin laser sheet. In absence of tethering, the researcher may have to wait patiently for the organism to swim through the imaging region of the laser sheet and hope that the body orientation is ideal during the pass. Obviously, this is a potentially tedious experimental procedure. As an alternative, researchers have suggested adding a fixed translational velocity to the measurements around tethered copepods to account for the differences in the flow field (e.g., Koehl and Strickler, 1981). It also has been suggested that placing a tethered

copepod in a moving current (at a speed that matches a typical swim velocity) eliminates the potential influence of the tether on the flow field (Bundy and Paffenhöfer, 1996).

Despite the common use of tethering of zooplankton during flow studies, a comparison between untethered and tethered larvae showed that the flow pattern is altered by the presence of the tether (Emlet, 1990). In addition, the magnitude and location of high velocity regions are different in tethered versus untethered copepods and larvae (Emlet, 1990; Bundy and Paffenhöfer, 1996). In addition to the physical differences in the flow field, the organism behavior is also potentially modified by the addition of the tether. Hwang et al. (1993) found similar mean time allocation habits of tethered copepods compared to untethered copepods, but there was a significant difference in the individual variability.

The objective of this study is to quantitatively compare the flow fields created by tethered and untethered copepodids using the particle image velocimetry (PIV) technique. As described in detail below, the fields of velocity, vorticity, dissipation rate, and strain rate created by the copepodid *Euchaeta antarctica* were quantified for free-swimming and tethered specimens. Because events occur at time scales of milliseconds for organisms in the millimeter range, the measurements require high precision in timing and high spatial resolution.

3.3 Materials and methods

3.3.1 Collection of organisms

Euchaeta antarctica individuals were collected at Croker Passage at latitude 64°05' S and longitude 62°50' W in the Southern Ocean during November 2003. The collected specimens were CV copepodids with a prosome length of 4.6 mm. Copepodids were sorted into 2 L containers of chilled seawater and hand-carried to our laboratory at the Georgia Institute of Technology in Atlanta, Georgia. In the laboratory, the specimens were placed in a dark environmental chamber at 0°C. The copepodids swam freely in 19 L buckets with gentle aeration and were fed phytoplankton. All measurements were performed within the first month since capture, although the copepodids lived for over 3 months in the laboratory.

3.3.2 Experimental setup

Flow fields created by free-swimming and tethered *E. antarctica* were visualized in a clear, glass cubic tank (15 cm × 15 cm × 15 cm) filled with artificial seawater of salinity of 34.85 ppt in a dark room. The temperature of the tank was maintained at 0°C during the experiment by immersing the glass tank in a recirculating bath of propylene glycol and deionized water, which was surrounded by insulating foam with small windows to provide optical access for the cameras. The recirculating bath fluid passed through a Fisher Scientific chiller in order to maintain the desired temperature. Images of free-swimming copepodids were recorded only when the copepodids swam through the laser sheet. A second camera, connected to a television monitor and possessing a

perspective perpendicular to the PIV camera, was used to monitor the position of the free-swimming copepodids.

To restrain the copepodid, we tethered it to a 38-gauge copper wire attached by cyanoacrylate glue. Attachments were made to the dorsal side of the copepodid near the junction between the cephalic and thoracic segments. A 0.5 mm bend at the end of the wire provided enough surface area for attachment. The end of the wire, dipped in glue and air-dried for 30 seconds until the glue was tacky, was attached to a copepodid, which was restrained in a drop of water in a cooled Petri dish. Just prior to attachment, the copepodid was blotted dry of seawater for less than 1 second. Once the tacky end of the wire made contact with the dorsal side of the copepodid, ambient seawater was added which annealed the bond. The copepodid was fully submerged in seawater and the copepodid-wire bond was checked for proper attachment and positioning away from the cephalic appendages. Copepodids with poorly positioned tethers were not used for flow field imaging. The bend directed the wire away from the copepodid at a right angle to minimize interference with the deployment of the locomotory appendages, although as noted below the presence of the tether appeared to influence the symmetry of the resultant biologically-generated flows. The wire was attached via a glass rod to a 3-axis precision position manipulator, which was used to position the copepodid in the laser sheet in the center of the field of view of the camera.

3.3.3 Fluid velocity measurements

Flow fields were measured for free-swimming and tethered *Euchaeta antarctica* using the non-intrusive particle image velocimetry (PIV) technique. The PIV technique

measures the displacement of small tracer particles suspended in the fluid over a short time period (e.g., Westerweel, 1997; Raffel et al., 1998). The advantage of this technique is that the position of many particles can be recorded with a digital camera; hence, a field of simultaneous velocity vectors is measured. Because the particles were illuminated by a laser sheet, the displacement vectors corresponded to the plane of illumination. One important assumption for PIV is that the particles follow the fluid flow over the measurement interval; therefore, tracer particles must be small and nearly neutrally-buoyant. In the current experiments, titanium dioxide particles with a mean diameter of less than 5 μm were homogeneously seeded into the fluid.

The particles were illuminated with an Oxford pulsed infrared laser (model HSI-500). The laser illuminated particles in a 1 mm thick sheet with a row of laser diodes that produced monochromatic light at a wavelength of 808 nm and maximum pulse energy of 15 mJ. Many copepods are phototactic, respond to light by swimming towards it, and are typically most sensitive to wavelengths centered around 500 nm (Stearns and Forward, 1984; Cohen and Forward, 2002). The copepodids swam freely into and out of the near IR wavelength laser sheet with no observable avoidance or preference to the laser and with no observable change in swimming characteristics. The laser pulse repetition period was variable within the range of 1 to 80 ms with longer delay period corresponding to greater output energy and illumination. In this set of experiments, the period between the laser pulses was 8 ms and a timing control circuit synchronized the camera shutter with the laser pulses. A VDS Vosskühler CMC-1300 CMOS digital camera and a Datacube MaxRevolution image acquisition board acquired the images. Image pairs (i.e., images of the laser pulses separated by 8 ms) were collected at 50 Hz. The width of the laser

sheet (1 mm) is relatively large compared to the size of the copepodid body (prosome length of 4.6 mm). As a result, the "planar" velocity measurements correspond to a finite width of the three-dimensional flow. Based on the camera lens focal length (105 mm), aperture (f/2.8), and location, the depth of field was calculated to be 0.725 mm. Therefore, the reported velocity fields correspond to the average over the depth of field rather than true planar velocity fields.

Pairs of PIV images were analyzed to determine the particle displacement in the image plane via a cross-correlation calculation (e.g., Raffel et al., 1998). The images were divided into interrogation subwindows of 32 × 32 pixels. Particle locations in a subwindow in the first image were compared to the corresponding subwindow in the second image by calculating the cross-correlation function in phase space. The average particle displacement in the subwindow region was determined by locating the peak value of the cross-correlation function relative to the center of the subwindow. The location of the peak in the correlation was identified to subpixel accuracy via a Gaussian function fit. This process was repeated for the entire image with a 50% overlap of each subwindow. The velocity was calculated by dividing the displacement vector by the time delay between consecutive laser pulses. The velocity data were validated by calculating the median velocity of a 3 × 3 grid of neighboring points and comparing the local velocities to the median velocity (Westerweel, 1994; Nogueira et al., 1997). Velocity vectors outside of an acceptable range were identified as bad vectors and replaced by a spatially-interpolated value. Velocity vectors that coincided with the location of the organism body were removed during post-processing by creating a blanking template from the

original image pair. Based on the accuracy of the peak correlation location estimate and other considerations, the uncertainty of the velocity vector is estimated to be ±3%.

3.3.4 Flow field analysis

The coordinate system (shown in Figure 3.1) for the flow field analysis was aligned with the body of the copepodid such that the origin of the coordinate system is at the head of the organism. The x direction is along the body axis, the y direction corresponds to the transverse coordinate in the dorso-ventral view (positive direction pointed toward the right side antennae), and the z direction corresponds to the transverse coordinate in the side view (positive direction pointed toward the dorsal side of the copepodid). The velocity components in the x, y, and z directions are u_x, u_y, and u_z, respectively. The reported velocity vectors correspond to the average value for samples collected within a one second period. The individual velocity fields were shifted before averaging such that the coordinate origin was always coincident with the head of the organism. The PIV data were rotated to be in the same orientation as the tethered copepodid, using the appropriate transformations for vector and tensor (e.g., strain rate) quantities.

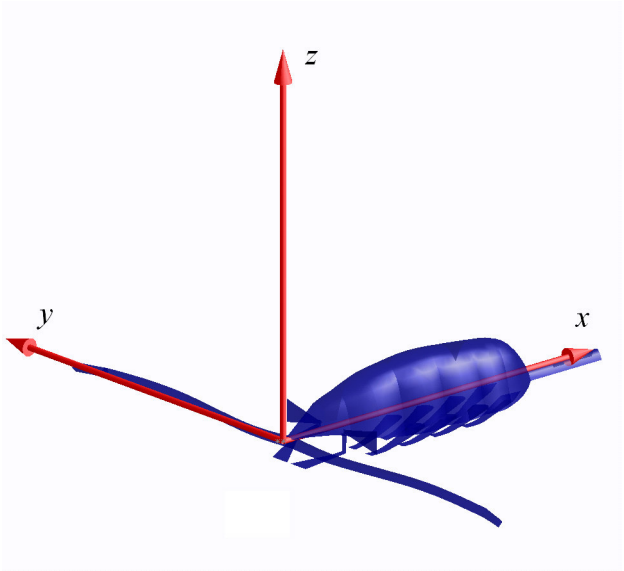

Figure 3.1. Coordinate system for the flow analysis.

The spatial gradient of velocity is important from a mechanosensory perspective and previous studies suggest that strain rate is the quantity that most closely correlates with copepod behavior (e.g., Fields and Yen, 1997a; Kiørboe et al., 1999; Woodson et al., 2005). Strain rate is a measure of the deformation of a fluid element as it flows. The strain rate components that can be directly calculated based on the measured planar velocity fields are:

$$e_{xx} = \left(\frac{du_x}{dx} \right); e_{yy} = \left(\frac{du_y}{dx} \right); e_{zz} = \left(\frac{du_z}{dx} \right)$$
$$e_{xy} = \frac{1}{2}\left(\frac{du_x}{dy} + \frac{du_y}{dx} \right); e_{xz} = \frac{1}{2}\left(\frac{du_z}{dx} + \frac{du_x}{dz} \right) \quad (3.1)$$

Vorticity is another quantity based on the velocity gradient and hence also could be important to define the perturbation created by an organism, although currently there is no direct evidence to support this conjecture. Vorticity is a point measure of the rotation of the fluid, and the components of the vorticity vector for the measured planes are:

$$\omega_z = \left(\frac{\partial u_y}{\partial x} + \frac{\partial u_x}{\partial y} \right); \omega_y = \left(\frac{\partial u_x}{\partial z} + \frac{\partial u_z}{\partial x} \right) \quad (3.2)$$

Another quantity involving spatial gradients of the velocity field is the viscous dissipation rate of kinetic energy. This quantity is of interest because it relates to the costs of propulsion, the time that a flow perturbation persists, and the ecological significance of predator avoidance. The rate of energy dissipation due to viscosity, Ψ, is defined as (e.g., Schlichting and Gersten, 2000):

$$\Psi = \mu \left[\begin{array}{l} 2\left(\frac{\partial u_x}{\partial x}\right)^2 + 2\left(\frac{\partial u_y}{\partial y}\right)^2 + 2\left(\frac{\partial u_z}{\partial z}\right)^2 + \\ \left(\frac{\partial u_x}{\partial y} + \frac{\partial u_y}{\partial x}\right)^2 + \left(\frac{\partial u_x}{\partial z} + \frac{\partial u_z}{\partial x}\right)^2 + \left(\frac{\partial u_y}{\partial z} + \frac{\partial u_z}{\partial y}\right)^2 \end{array} \right] \tag{3.3}$$

Several derivative terms in equation (3.3) cannot be calculated directly from the planar PIV data. For instance, for data in the x - y plane the u_z component of velocity and derivatives in the z direction cannot be determined directly. In this case, the $\partial u_z / \partial z$ term was estimated using the incompressible continuity equation:

$$\frac{\partial u_z}{\partial z} = -\frac{\partial u_x}{\partial x} - \frac{\partial u_y}{\partial y} \tag{3.4}$$

The other unknown terms are assumed to be approximately equal to a measured term, specifically:

$$\left(\frac{du_x}{dz} + \frac{du_z}{dx}\right)^2 \approx \left(\frac{du_x}{dy} + \frac{du_y}{dx}\right)^2 \text{ and } \left(\frac{du_y}{dz} + \frac{du_z}{dy}\right)^2 \approx \left(\frac{du_x}{dy} + \frac{du_y}{dx}\right)^2 \tag{3.5}$$

Therefore, the energy dissipation rate approximated in terms of the gradients calculated in the x - y plane is:

$$\Psi = \mu \left[2\left(\frac{\partial u_x}{\partial x}\right)^2 + 2\left(\frac{\partial u_y}{\partial y}\right)^2 + 2\left(-\frac{\partial u_x}{\partial x} - \frac{du_y}{dy}\right)^2 + 3\left(\frac{\partial u_x}{\partial y} + \frac{\partial u_y}{\partial x}\right)^2 \right] \tag{3.6}$$

An analogous equation was employed for the x - z plane.

3.4 Results

In this experiment, PIV images of five tethered individuals and three free-swimming individuals were collected. The replicate data were qualitatively similar to the data shown in the figures and the similarities are discussed in later sections. The data shown herein were selected for publication because the animal's trajectory was centered in the image region.

To compare among free-swimming and tethered flow fields, it was important to check that the swimming behavior of the copepodids was similar. Several criteria were used to confirm that all tested specimens were behaving in a typical cruising mode. First, the raw image sequences of the free-swimming and tethered copepodids were viewed to verify that the second antennae were being used to propel the organism. The second antennae are used for propulsion during cruising, whereas the antennules (first antennae) and swimming legs are used for propulsion during escaping. Occasionally, we observed the appendage motion associated with escape behavior in both the free-swimming and tethered specimens, but the data presented herein are exclusively associated with cruise swimming behavior. Second, we confirmed that the swimming speeds of the free-swimming copepodids for the reported PIV data (0.83 cm s^{-1} for the dorso-ventral view, and 0.82 cm s^{-1} for the side view) were consistent with typical swimming speeds for cruising copepodids. Table 3.1 shows the average and standard deviation of the swimming speeds and Reynolds number measured for a total of 67 individual specimens. Typical swimming speeds of cruising organisms are an order of magnitude smaller than the typical escaping speeds. Third, we measured the appendage paddling frequency and

found that both the tethered and free-swimming copepodids were paddling at approximately 50 Hz.

Table 3.1 Swimming speed and Reynolds number (mean ± std. dev.) for *Euchaeta antarctica* CV copepodids based on three-dimensional trajectory observations. N is the number of individual specimens observed. For the cruise mode, between 11 and 120 measurements of swimming speed for each individual were collected depending on the length of the observed path. For the escape mode, between 4 and 18 measurements of swimming speed for each individual were collected. The characteristic velocity and length scales in the Reynolds number are the swimming speed and prosome length, respectively.

Mode	**Swimming speed (cm s^{-1})**	**Reynolds number**	***N***
Cruising	1.46 ± 0.62	12 ± 5	38
Escaping	13.65 ± 4.80	105 ± 45	29

3.4.1 Flow field

The streamlines of the flow field for the free-swimming copepodid in both the dorso-ventral and side views slightly converged in front of and slightly diverged behind the body of the organism (Figure 3.2 A,C). These images were created by tracking tracer particle movement in the frame of reference of the copepodid. While the streamlines around the free-swimming copepodid were nearly parallel to the body of the specimen (Figure 3.2 A,C), the streamlines around the tethered copepodid curved sharply into the feeding appendages and abdomen (Figure 3.2 B,D). More pronounced convergence (upstream) and divergence (downstream) of the streamlines was evident for specimens in the figures and the replicates that are not shown. Qualitatively, the volume of fluid influenced by the tethered copepodid appeared to be greater than the volume of fluid influenced by the free-swimming copepodid in agreement with previous observations by Emlet (1990) for larvae of bivalves and gastropods and by Gallager (1988) for larvae of mollusks. Specifically, Emlet (1990) noted that the particle paths were much wider upstream for the tethered specimen compared to the free-swimming organism, which agrees with Figure 3.2.

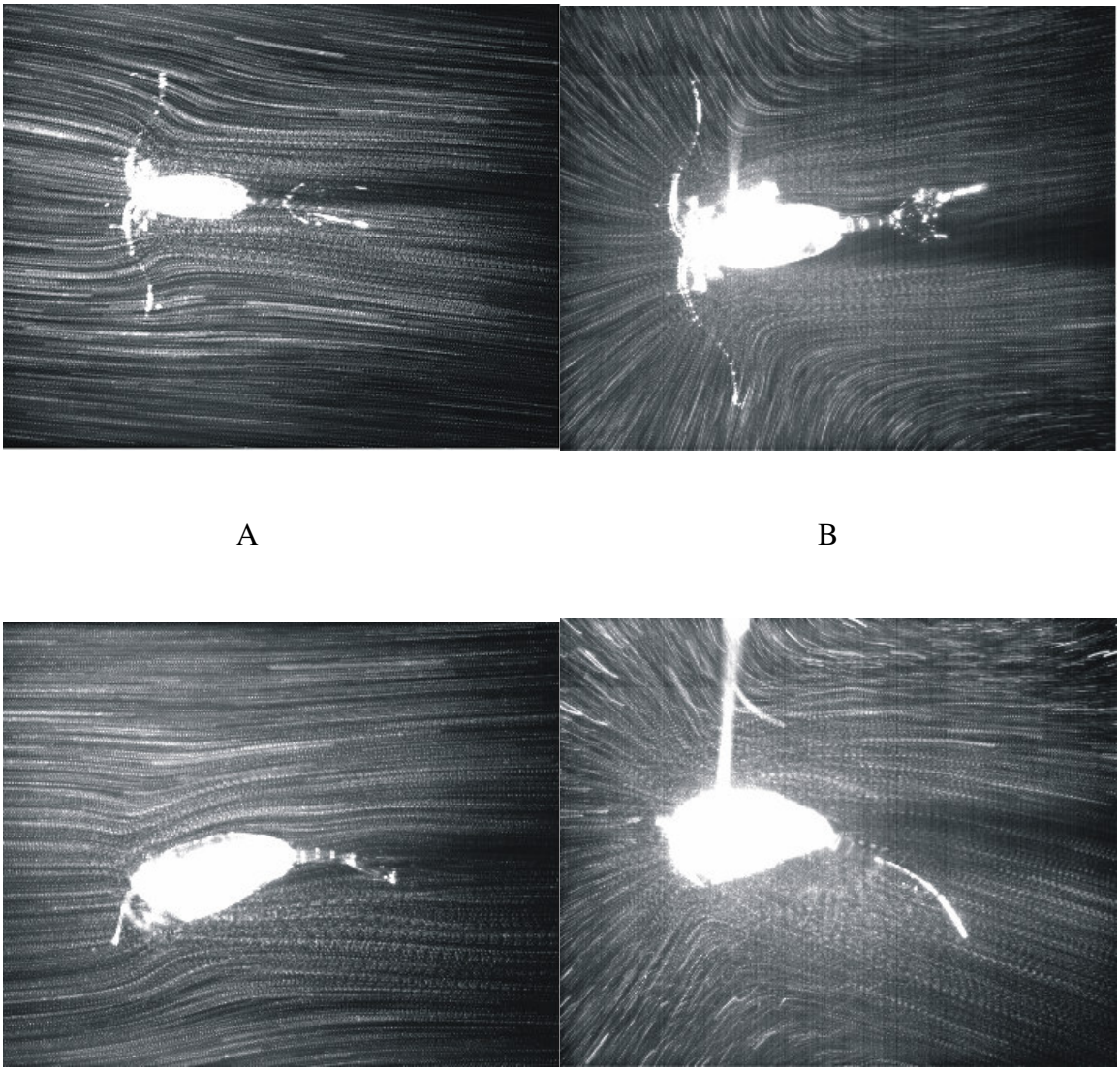

Figure 3.2 (A,B) Dorso-ventral and (C,D) side views of tracer particle paths around a (A,C) free-swimming and a (B,D) tethered *Euchaeta antarctica.*

3.4.2 Velocity field

The velocity around the body of the free-swimming copepodid was symmetrical about the line $y = 0$ with a maximum velocity of 1.2 cm s^{-1} occurring approximately 0.05 cm to the side of the abdomen of the copepodid (Figure 3.3 A). The velocity vectors for the free-swimming copepodid were nearly parallel to the body of the copepodid. In contrast, the velocity around the body of the tethered copepodid was asymmetrical with maximums of 0.8 cm s^{-1} on the right side ($y > 0$) and 1.4 cm s^{-1} on the left side ($y < 0$) (Figure 3.3 B). The maximum velocities in the replicate were similarly asymmetric with maximum values of 0.3 cm s^{-1} and 0.9 cm s^{-1} on each side. For the figure and replicate fields, the larger magnitude of velocity occurred on the side of the body that was opposite to the tether connection to the position manipulator. The flow asymmetry appeared to result from the effect of the tether presence on the movement of the cephalic appendages. The tethered copepodids preferentially paddled on the side opposite of the tether in all images. The velocity vectors on the side of the copepodid facing the tether mount were directed outward from the body and the velocity vectors on the opposite side of the tether were directed into the copepodid body. In front of the copepodid, the free-swimming specimen created a low velocity region (0.2 cm s^{-1}), whereas the tethered copepodid created a higher velocity region (0.6 cm s^{-1}).

In the side view, the maximum velocity below the ventral side of the specimen ($z < 0$), was greater for the free-swimming copepodid (maximum velocity of 1.4 cm s^{-1}) than for the tethered copepodid (maximum velocity of 1.1 cm s^{-1}) (Figure 3.4). The high

velocity region below the copepodid in the side view was larger in magnitude and confined to a smaller region for the free-swimming specimen.

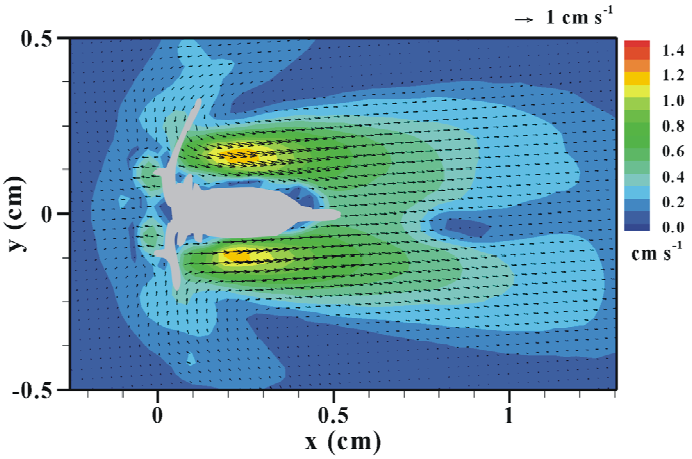

A

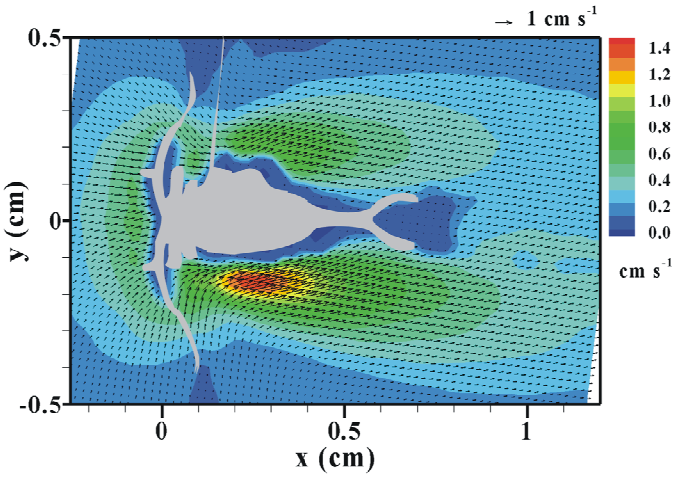

B

Figure 3.3 Velocity vectors and contours of velocity magnitude time-averaged over one second for a (A) free-swimming and (B) tethered *Euchaeta antarctica* for the dorso-ventral view.

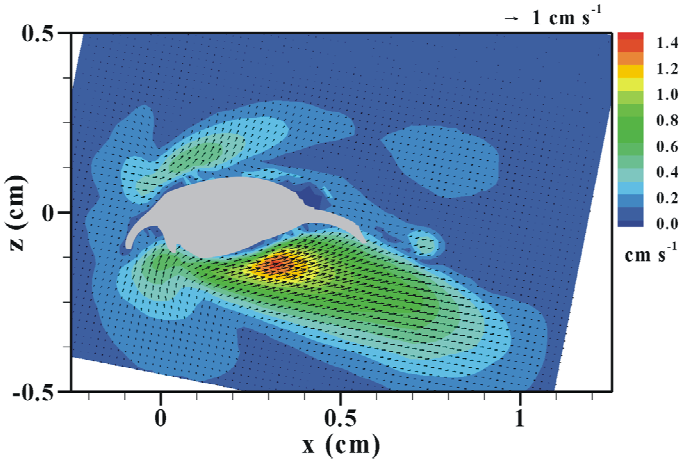

A

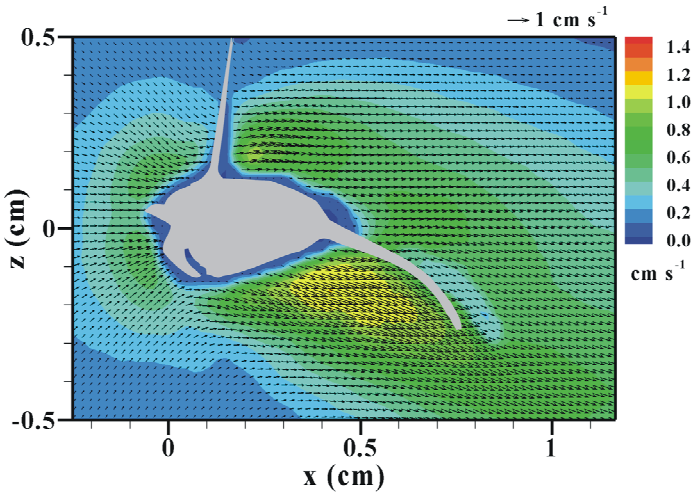

B

Figure 3.4 Velocity vectors and contours of velocity magnitude time-averaged over one second for a (A) free-swimming and (B) tethered *Euchaeta antarctica* for the side view.

3.4.3 Vorticity field

For the free-swimming copepodid, the vorticity field (Figure 3.5) also demonstrated (anti)symmetry about the $y = 0$ axis. The vorticity magnitude was largest in the boundary layer region near the body. Because of the opposite orientation of the velocity gradient, the vorticity on the left and right sides of the body had opposite signs; in both cases the maximum magnitude of the vorticity was roughly, 20 s^{-1}. In the side view, the region of high vorticity magnitude also was confined to the near body boundary layer and in particular along the ventral surface of the copepodid. In this plane, the maximum vorticity magnitude also was roughly 20 s^{-1}.

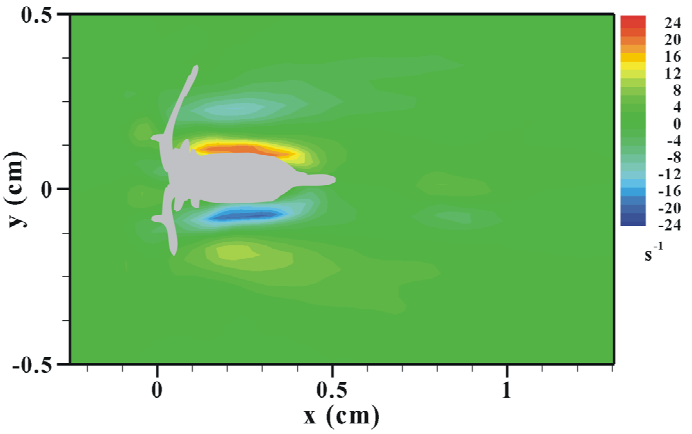

A

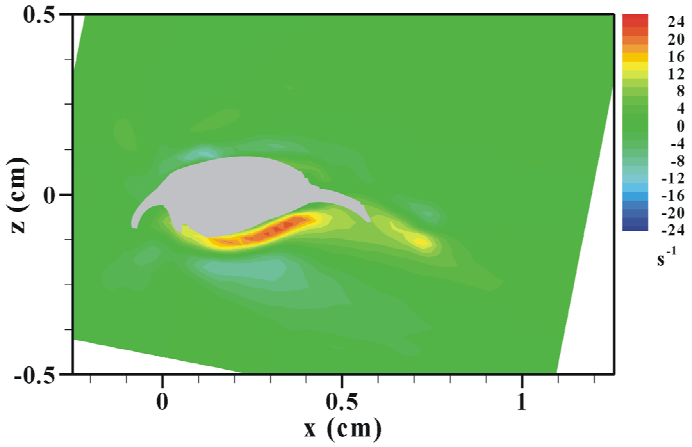

B

Figure 3.5 Contours of the vorticity field created by a free-swimming *Euchaeta antarctica* for the (A) dorso-ventral view (ω_z) and (B) side view (ω_y).

3.4.4 Dissipation Rate field

Kinetic energy was dissipated by viscous effects at relatively high levels along the sides of the free-swimming copepodid (y = 0.1 cm, y = -0.1 cm), behind the antennules, along the ventral surface (z < 0), and along the dorsal surface (z = 0.1 cm) (Figure 3.6). The maximum dissipation rate for the free-swimming copepodid occurred along the ventral surface (28 Wm^{-3}). Although not shown in a figure, the peak value of dissipation rate for the tethered copepodid was similar (roughly 30 Wm^{-3}). The total energy dissipation rate is calculated by integrating the dissipation rate, which is a point function, over the region of flow.

Table 3.2 summarizes the total energy dissipation rate in the planar velocity field (Wm^{-1}) by the tethered and free-swimming copepodids in the planar velocity field. The total energy dissipation rate was larger for the tethered copepodids in all cases but the difference was greatest in the side view cases. Based on these planar data and assuming axisymmetry, a rough estimate of the total dissipation rate in the fluid volume influenced by the copepodid is around 1×10^{-8} W. This is an order of magnitude larger than the estimate by Yen et al. (1991) for *Euchaeta rimana* and two orders of magnitude larger than the estimate by van Duren et al. (2003) for *Temora longicornis*. The difference may result from the fact that *E. antarctica* is larger than the other species. Further, increased resolution of the measurements may improve (and increase) the dissipation rate estimate due to better resolution of the spatial variation in velocity.

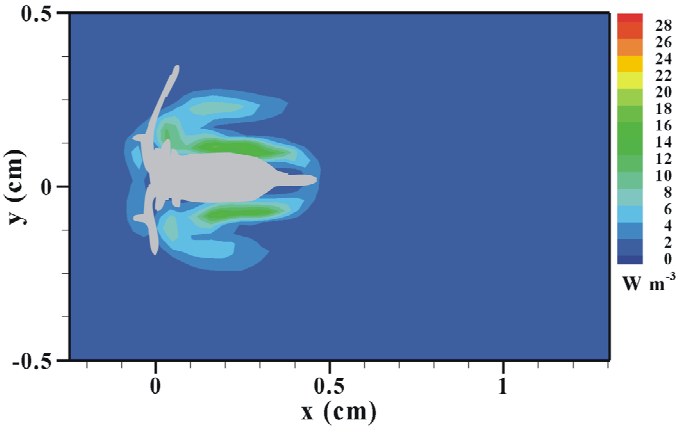

A

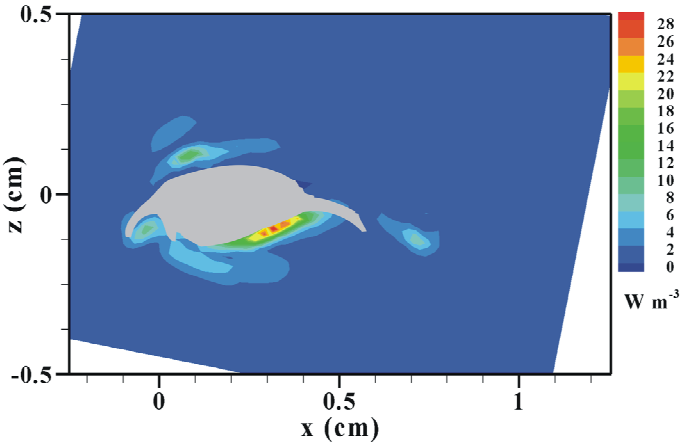

B

Figure 3.6 Contours of dissipation rate (Ψ) for a free-swimming *Euchaeta antarctica* for the (A) dorso-ventral view and (B) side view.

Table 3.2 The total energy dissipation rate of a cruising copepodid (Wm^{-1}). Replicate values are shown in parenthesis.

	Energy dissipation rate (Wm^{-1})	
	Side view	**Dorso-ventral view**
Tethered	7.5×10^{-6} (2.1×10^{-5}, 1.1×10^{-5})	9.3×10^{-6} (8.0×10^{-6})
Free-swimming	4.7×10^{-6}	5.2×10^{-6} (7.8×10^{-6})

3.4.5 Strain Rate field

The e_{xx} component of the strain rate tensor is shown in Figure 3.7 for the free-swimming copepodid. As with the other quantities described above, the location of the largest values of the strain rate was in the boundary layer region near the copepodid body. The peak value was approximately 10 s^{-1} along the appendages and the ventral surface of the copepodid. A peak negative value of -10 s^{-1} occurred along the antennae in front of the copepodid (i.e., x = -0.05 cm). Other components of the strain rate tensor showed a similar spatial distribution and will be discussed below for a specific profile location.

3.4.6 Example profiles

The field plots are useful because they reveal spatial variability of the quantities. However, the field plots are limited in the respect that it is difficult to make definitive comparisons between the free-swimming and tethered specimens. To further examine the similarities and differences between the flow characteristics around the free-swimming and tethered copepodids, profiles of the velocity, vorticity, and strain rate were extracted from the fields. Profiles are shown in Figure 3.8 for flow quantities along a profile axis direction that was perpendicular to the copepodid body axis in the dorso-ventral view. To best match the spatial location of the flow field, the position of the profile was specified such that it passed through the location of the maximum in velocity magnitude for each specimen (shown in Figure 3.8). Several other profile orientations were examined during this study with similar observations as the current example.

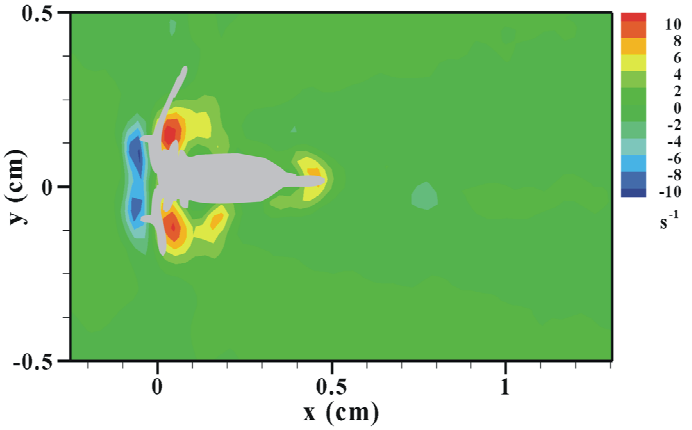

A

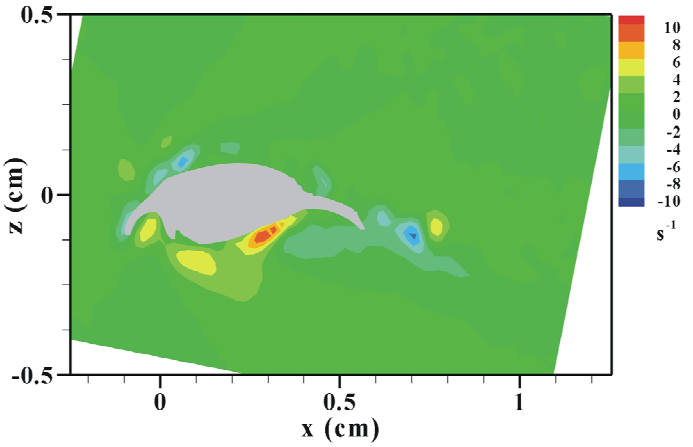

B

Figure 3.7 Contours of strain rate (e_{xx}) for a free-swimming *Euchaeta antarctica* for the (A) dorso-ventral view and (B) side view.

As described for the field plots in Figure 3.3, the velocity direction and magnitude was altered by the presence of the tether. In Figure 3.8 A,B, the peak value of the u_x-component of velocity was greater in the tethered case, and the u_y-component differed in magnitude and direction over much of the profile. The vorticity (Figure 3.8 C) and shear strain rate (Figure 3.8 F) profiles in this case agreed fairly well between the specimens, except very close to the copepodid body ($y' < 0.05$ cm) where the magnitude of both quantities was greater in the tethered case. The normal strain rate components (shown in Figure 3.8 D,E) were different between the tethered and free-swimming profiles. This reflected both a change in the velocity components (Figure 3.8 A,B) and a change in the spatial variation (i.e. gradient) of the velocity field.

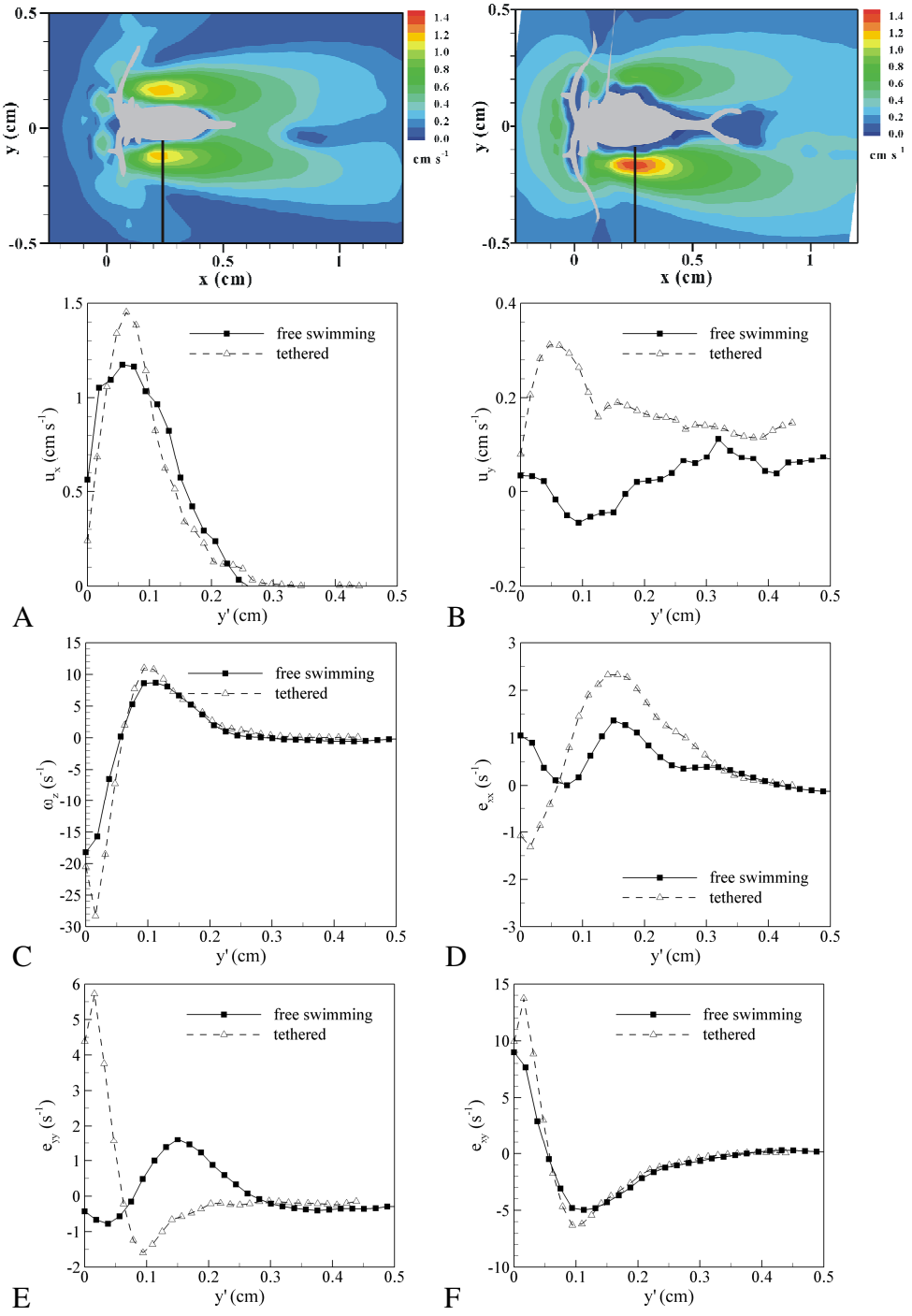

Figure 3.8 Exemplary profiles along the highlighted direction for the free-swimming and tethered *Euchaeta antarctica*. The profile direction in the dorsoventral view is oriented at 90° relative to the center axis of the organism and passes through the location of maximum velocity. Profiles correspond to (A) u_x, (B) u_y, (C) ω_z, (D) e_{xx}, (E) e_{yy}, and (F) e_{xy}. y' is zero at the location of the organism body rather than at the organism center axis

3.5 Discussion

3.5.1 Effects of tethering

As presented in the Results Section and by other researchers (Emlet, 1990; Bundy and Paffenhöfer, 1996), the flow field around a tethered organism differs from that around a free-swimming animal. On this note, van Duren et al. (2003) write "there is no doubt that the morphology of flow fields [around tethered copepods] will be to some extent different from those around moving animals." At first thought, it seems intuitive to suggest that the difference is merely due to a translational velocity difference due to the fixed position of the tethered specimen compared to the moving specimen. However, the particle trajectories shown in Figure 3.2 demonstrate that the difference is not solely due to the addition of a uniform velocity field corresponding to the translation of the organism. In both sets of images, the particles are moving past a copepodid fixed in the photograph, and it is clear that the particle paths are very different. Further, the data in Figs. Figure 3.3, Figure 3.4, and Figure 3.8 provide quantitative evidence that the presence of the tether greatly influences the flow field characteristics.

To explain the fundamental difference between the tethered and free-swimming flow fields, it is illuminating to consider the forces. The free body diagrams for the organism in the free-swimming and tethered cases are sketched in Figure 3.9. For an organism swimming in the horizontal direction (as shown in the sketch), the relevant forces on the copepod are the drag and thrust. For an organism that is cruising, i.e., not accelerating, the forces acting on the body are in equilibrium, which means they are equal and opposite in direction. Each force acts on the organism in one orientation and on the

fluid in the opposite orientation. On the organism, F_{thrust} acts in the direction of copepod motion, and F_{drag} acts opposite to the direction of copepod motion. On the fluid, F_{thrust} acts opposite to the direction of copepod motion and induces a fluid jet away from the organism, and F_{drag} acts in the direction of copepod motion and causes fluid to be dragged along with the organism.

The force balance changes meaningfully with the addition of a tether. The (non-accelerating) organism can now impart an unbalanced force on the fluid because it can push against the tether. The resistance to acceleration is not provided by a drag force, but is given rather by the force and moment on the tether. The force and moment on the tether balance F_{thrust} and act out of, and not on, the fluid (Figure 3.9 B). Hence, adding a translational velocity to the tethered flow field (a kinematic operation) does not take into account the force F_{drag} that results from fluid viscosity and causes fluid to be dragged along with the organism (a dynamic effect). (Note that an equally valid description of this phenomenon has been made with regard to a "momentumless wake" for a self-propelled object (e.g., Naudascher, 1965; Sirviente and Patel, 2000). The term "momentumless wake" refers to the momentum distribution in the wake of the self-propelled object having the same momentum flux as the approaching flow upstream of the object. The addition of a tether alters the momentum distribution in the wake due to the addition of the unbalanced force on the fluid.

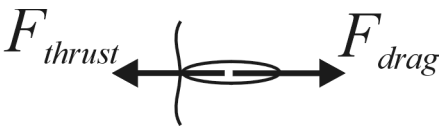

A

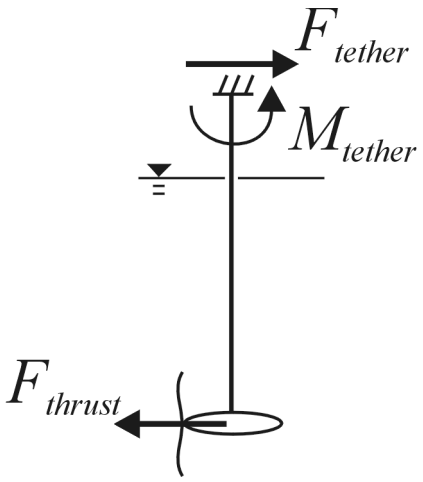

B

Figure 3.9 Free body diagram for the (A) free-swimming and (B) tethered copepods.

The difference between the flow fields is largely explained by the unbalanced force in the tethered case. An analytical solution of the Navier-Stokes equations for the laminar flow induced by a point force was first reported by Landau (1944) and Squire (1951). The analysis begins by locating a force at the coordinate origin within an infinitely large fluid domain. The point force and polar coordinate system are shown in Figure 3.10 A. The solution for the flow velocity components is:

$$u_r = \frac{2\nu}{r}\left[\frac{2\cos\theta}{(C+1-\cos\theta)} - \frac{\sin^2\theta}{(C+1-\cos\theta)^2}\right] \tag{3.7}$$

$$u_\theta = \frac{-2\nu}{r}\frac{\sin\theta}{(C+1-\cos\theta)} \tag{3.8}$$

and the streamfunction is:

$$\psi = 2\nu r\frac{\sin^2\theta}{(C+1-\cos\theta)} \tag{3.9}$$

where C is a constant related to the strength of the force imposed at the origin (Squire, 1951):

$$\frac{F}{2\pi\rho\nu^2} = \frac{32}{3C}\frac{1+C}{2+C} + 4(1+C)^2\ln\left(\frac{C}{2+C}\right) + 8(1+C) \tag{3.10}$$

In these equations, r and θ are the polar coordinates, ν is the fluid kinematic viscosity, ρ is the fluid density, and F is the magnitude of the applied force. Sherman (1990) provided an alternative interpretation of C in which the radial velocity

component, u_r, is evaluated along the downstream axis (i.e., $\theta = 0$) at an arbitrary distance $r = R$:

$$\frac{R u_r\big|_{\substack{r=R \\ \theta=0}}}{\nu} = \frac{4}{C} \tag{3.11}$$

Note that the left hand side appears like a local Reynolds number evaluated at $r = R$ and $\theta = 0$. We used the measured velocity field for the tethered copepodid to estimate the velocity at a distance of 0.75 cm downstream of the tether location. The resulting value for C was 0.4.

Figure 3.10 B shows the streamline pattern for the analytical flow solution. The streamlines converge upstream of the force location and diverge more gradually downstream. Comparison of the analytical streamline pattern with the particle paths for the tethered copepodid in Figure 3.2 B,D reveals a remarkable similarity. Despite the presence of the organism body and the fact that the force on the fluid is more broadly distributed in the organism case compared to the theoretical case, the general agreement suggests that the addition of a force on the fluid at the tip of the tether provides an explanation of the modified flow field for the tethered case compared to the free-swimming case.

Based on this discussion, we can draw some important practical conclusions. The flow field in the tethered case cannot be "corrected" by adding a uniform translational velocity (Koehl and Strickler, 1981). Rather, the addition of the unbalanced force in the tethered case modifies the flow field due to the viscous flow effects. The modified flow

field has different spatial gradients and hence different fields of vorticity, strain rate, and dissipation rate. Further, calculations performed during previous investigations of the filtering rate, volume of fluid entrained by zooplankton, and spatial extent of the fluid disturbance are influenced by the modification of the flow field. One solution to this dilemma is to perform the velocity field measurements on free-swimming organisms, as done in the current study. An alternate solution is to place the organism in a moving current (Bundy and Paffenhöfer, 1996), but implementing this strategy raises difficult practical issues. To eliminate the unbalanced force effect described above, the drag force due to the fluid moving past the organism body must exactly balance the self-generated thrust of the organism. The flow velocity in the test channel must be adjusted such that force on the tether equals zero, which in practical application requires that the force on the tether be measured (continuously). Because the tethered copepodid specimens demonstrate unsteady thrust generation (i.e., their swimming behavior and thrust force varies in time), data collection should be limited to periods when the measured force on the tether equals zero.

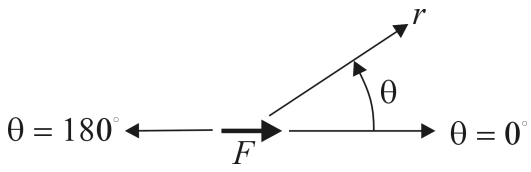

A

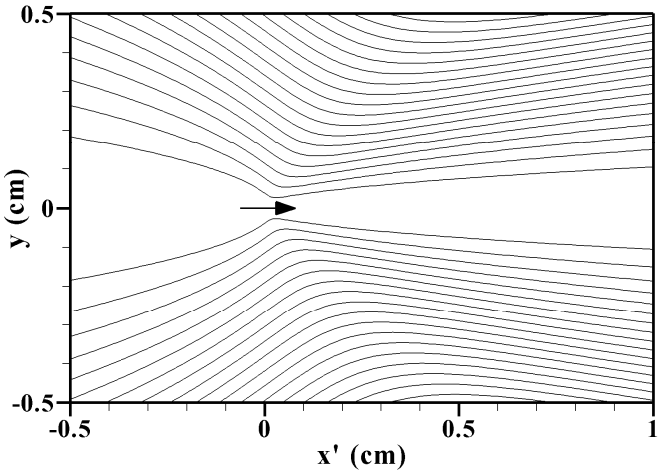

B

Figure 3.10 (A) Coordinate system and (B) streamline pattern for the theoretical solution of a force at the origin pointed to the right. C=0.4 for the streamlines shown. x' is zero at the location of the tether, rather than at the head of the organism.

3.5.2 Flow field of the free-swimming copepodid

Researchers have quantified the flow fields around tethered copepods (Bundy and Paffenhöfer, 1996; van Duren et al., 1998, 2003) and free-swimming copepods (Tiselius and Jonsson, 1990; Yen et al., 1991; Fields and Yen, 1993; Bundy and Paffenhöfer, 1996; Malkiel et al., 2003). The copepodids in these studies exhibited three locomotive modes: feeding, cruising, and escaping. Both simulations (Jiang et al., 2002b) and experiments (Tiselius and Jonsson, 1990; Bundy and Paffenhöfer, 1996) have shown that the geometry of the flow field is dependent on the locomotive mode. The current discussion is limited to the cruise mode of swimming.

Flow fields for free-swimming copepods have not been measured previously with planar PIV, but data from lower resolution particle tracking and holography methods provide useful information for comparison to the current results. In light of the discussion above regarding the modification of the flow field due to the presence of the tether, we did not make detailed comparisons to previous planar PIV data for tethered copepods despite the fact that the data in those studies have superior resolution than the particle tracking and holography methods. Malkiel et al. (2003) observed large-scale recirculation of the fluid surrounding sinking, feeding copepods. The current data do not reveal the recirculation pattern because the data are locally focused around the organism body and the fact that the copepodids were moving in cruise mode.

Analyses of the small-scale fluid motion of the pelagic copepodid offers some insight into factors influencing the complexity of the biologically-generated flow. For this free-swimming polar species, *E. antarctica*, the magnitude of the velocity field

shows a maximum (1.2 cm s^{-1}) surrounding the locomotory appendages, the second antennae. Velocity fields of free-swimming copepods have maximum velocity magnitudes ranging from 0.3 cm s^{-1} to 3.8 cm s^{-1} (Tiselius and Jonsson, 1990; Yen et al., 1991; Fields and Yen, 1993; Bundy and Paffenhöfer, 1996) and 1.98 cm s^{-1} in the simulations of Jiang et al. (1999). The velocity fields for these copepods were symmetrical in the dorso-ventral view with converging streamlines into the appendages and diverging streamlines to the rear of the organism (Tiselius and Jonsson, 1990; Yen et al., 1991). The geometry of the flow field was similar in the current study, and the maximum velocity (1.2 cm s^{-1}) was in the same range. The velocity distribution in the current study differed from that observed by Bundy and Paffenhöfer (1996), who reported considerable variability among trials. The resolution of the velocity field around the locomotory appendages is superior in the current study, which could lead to better estimates of the velocity and may explain the discrepancy. Overall, the current flow field measurements are qualitatively consistent with the previous data collected with other methods and provide improved quantitative details while avoiding the issues of tethering.

As noted for the tropical congener of this copepod (Lenz and Yen, 1993), the intensity of the anterior flow field declines toward the distal tips of *E. antarctica*. Hence, the mechanoreceptive sensors extend beyond the induced flow field, which enables sensing of an approaching predator. In front of the antennules, the anterior feeding current velocity has a double maximum where the longest mechanosensory hairs are located (Figure 3.3 A, also Yen and Nicoll, 1990). The structure of the feeding current appears to be optimized for evoking escapes where prey wakes can be best detected

(closest to mechanosensors) and for aggregating prey where they can be captured (i.e., within capture range of this carnivorous copepod).

With regard to the mechanoreceptive cue generated by *E. antarctica*, Figure 3.8 D,E,F suggests that e_{xy} is the largest component of the strain rate in the induced flow field. Shear strain rates greater than 2 s^{-1} (maximum of around 10 s^{-1}) surround the locomotory appendage region, which demonstrates the intensity of the copepodid-generated flow disturbance. The 0.5 s^{-1} contour of e_{xy} for the free-swimming case (Figure 3.11 A,C), which is a likely threshold to induce an escape response (Fields and Yen, 1997a; Kiørboe et al., 1999), provides a measure of the spatial extent of the cue for other mechanoreceptive predators. The area in the dorso-ventral view surrounded by the 0.5 s^{-1} contour is 11 times the area of the exoskeletal form. Hence, mechanoreceptive predators will perceive a much more spatially-extended cue than the body size. The 0.5 s^{-1} contour of e_{xy} for the tethered specimen in the side view (Figure 3.11 D) shows that the extent of the strain rate field is much greater in the tethered case (the contour extends beyond the boundaries of the measured field). Thus, the spatial extent of the mechanoreceptive cue would be overestimated with these data for the tethered specimen. Alternatively, the spatial extent of the 0.5 s^{-1} contour for the tethered copepodid in the dorso-ventral view (Figure 3.11 B) is similar or slightly reduced compared to the free swimming case (Figure 3.11 A). The differences in the strain rate fields for the free-swimming and tethered copepodid field demonstrates the subtle influence of altering the spatial distribution of the flow field due to the physical presence of the tether (described above) and perhaps due to the behavioral changes of the organism. This comparison

highlights the importance of using a free-swimming flow field when making sensory ecology conclusions.

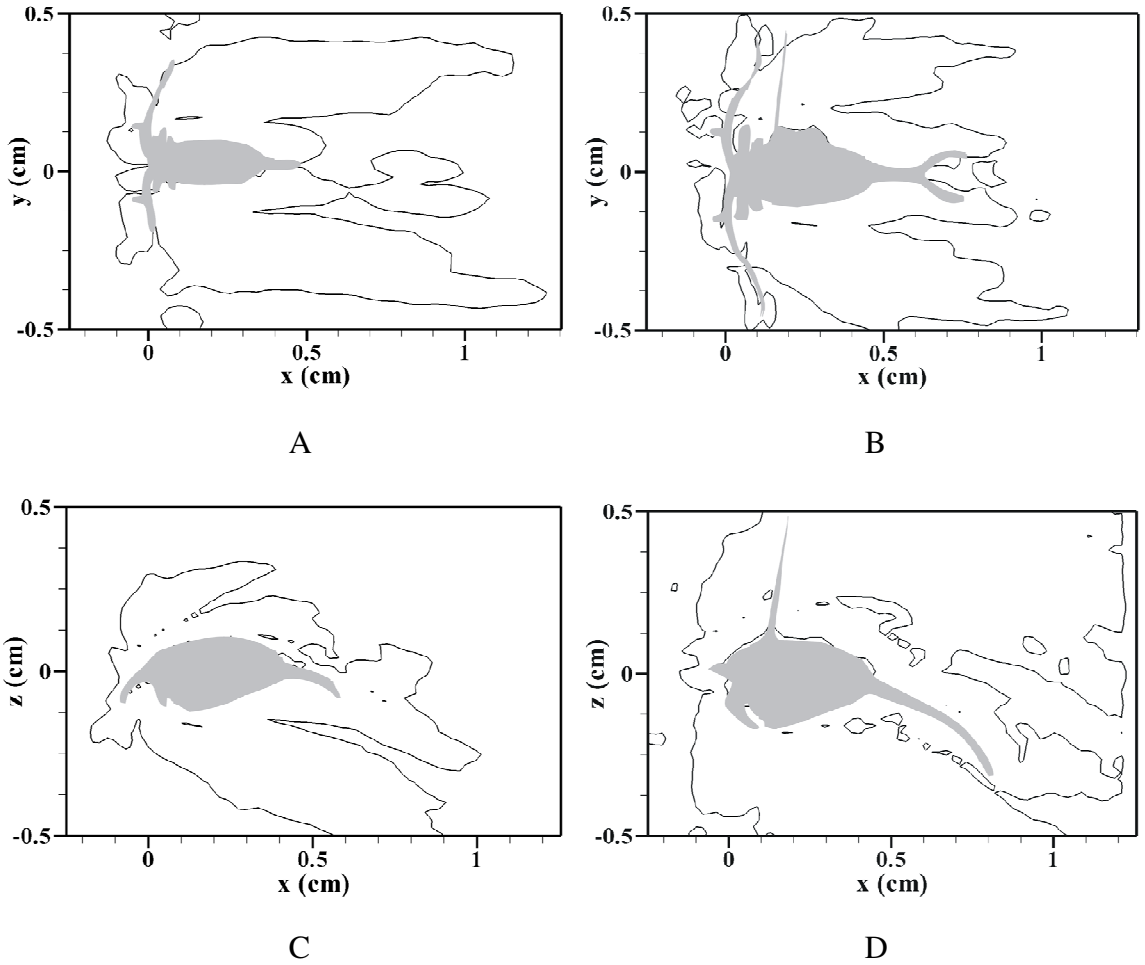

Figure 3.11 The 0.5 s^{-1} contour of strain rate (e_{xy}) for a (A,C) free-swimming and a (B,D) tethered *Euchaeta antarctica*. The 0.5 s^{-1} contour is shown as a representative value that has been observed to induce escape response in copepods (Fields and Yen, 1997a; Kiørboe et al., 1999).

CHAPTER 4

A COMPARISON OF THE FLOW FIELDS OF TEMPERATE AND SUBTROPICAL *EUCHAETA* SPECIES

4.1 Summary

We compared the fluid disturbances of cruising and escaping *Euchaeta elongata* and *Euchaeta rimana* copepods with the Particle Image Velocimetry technique. The copepod genera *Euchaeta* ranges from subtropical to polar latitudes, with body size and fluid viscosity increasing with higher latitude. The fluid disturbance generated by *Euchaeta* copepods during locomotion is conspicuous to both prey and predators. The spatial extent of copepod flow fields during cruising was not significantly different between species, but the spatial extent of the escape flow fields were larger for *E. elongata* individuals. To decouple the effects of viscosity and copepod size, a numerical simulation was employed for three different sized spheroids in subtropical, temperate, and polar seawater. For the model spheroids, the increase in viscosity between polar and subtropical environments caused a slight decrease in the spatial extent of the flow field, whereas a doubling of prosome length resulted in an approximate doubling of the spatial extent of the hydrodynamic disturbance. Copepod escapes are not necessarily more conspicuous than the cruising mode, but escapes are significantly more energetically costly to the organism.

4.2 Introduction

Marine species living at higher latitudes tend to be larger than their counterparts at subtropical latitudes in a phenomenon termed 'polar gigantism'. Polar gigantism has been attributed to factors such as metabolic effects at low temperature (Atkinson and Silby, 1997) and oxygen availability (Chapelle and Peck, 1999). Alternatively, the maximum size of organisms may be dictated by resource availability, food limitation, or vulnerability to predation (Atkinson and Silby, 1997). In the case of copepods, the spatial extent and magnitude of fluid disturbances created by copepod propulsion determines the organism's conspicuousness to prey and predators (Yen and Strickler, 1996; Kiørboe and Visser, 1999). The hydrodynamic disturbances generated by copepods vary depending on the fluid properties, copepod morphology, and copepod behavior (Tiselius and Jonsson, 1990; Bundy and Paffenhöfer, 1996; Yen and Strickler, 1996; Visser, 2001; Jiang et al., 2002a, 2002b). In the colder fluid environments found at higher latitudes, kinematic viscosity ranges from 1.3 to 2 times the value of subtropical fluid environments. Researchers have suggested that increased viscosity will reduce the spatial extent of a fluid disturbance (Fields and Weissburg, 2005), although the effect of increased viscosity on the spatial extent of copepod fluid disturbances has not been directly studied. If increased viscosity does reduce the spatial extent of a fluid disturbance, then copepods that live in colder environments and swim at the same speed as their subtropical counterparts could be larger without increasing their fluid disturbance and conspicuousness to prey and predators. Conversely, the energetic cost of propulsion is expected to increase in higher viscosity fluids as the viscous dissipation rate is directly proportional to the kinematic viscosity. The predatory copepod genus *Euchaeta* is ideal

to compare the spatial extents of copepod flow fields due to the global distribution of the genus and its position in the food chain where it functions as both predator and prey. The goal of this study is compare the hydrodynamic disturbances and the energetic costs of propulsion created by copepods of the genera *Euchaeta* living in temperate and subtropical waters.

To test whether copepods have the same hydrodynamic conspicuousness and energetic costs of propulsion in differing viscous realms, the hydrodynamic disturbances generated by copepods must be accurately measured. Previous studies have quantified the fluid disturbances from free-swimming copepods experimentally (Tiselius and Jonsson, 1990; Yen et al., 1991; Bundy and Paffenhöfer, 1996; Malkiel et al., 2003; Catton et al., 2007), numerically (Jiang et al., 2002a, 2002b), and analytically (Kiørboe and Visser, 1999; Visser, 2001). All these methods have been applied to cruising or feeding copepods, and we currently have a limited understanding of the fluid disturbance during escapes. During escapes, copepods are at risk to predation due to the propagation of strong hydromechanical cues (Fields and Yen, 1997a). Also, copepods expend a large amount of energy during escape maneuvers and the relative increase in the cost of propulsion has not been measured. Therefore, to assess the costs of copepod escapes in respect to conspicuousness and propulsion the flow fields generated from both cruising and escape behaviors will be quantified.

The components of a copepod flow field that constitute a hydromechanical cue are dependent on the role of the copepod in a predator-prey interaction. The spatial gradients of velocity, and specifically the linear and shear deformation rates, have been

identified as the hydromechanical cue perceived by copepods that elicits escape response (Fields and Yen, 1996, 1997a; Kiørboe et al., 1999). Kiørboe et al. (1999) found that within developmental stages of a copepod species, the product of the deformation rate and the radius of the prey was a more consistent cue. However, the maximum deformation rate, which is a measure of the largest fluid deformation rate, was the most consistent fluid quantity that copepods of different species responded with an escape response (Kiørboe et al., 1999; Green et al., 2003). Conversely, the hydromechanical cue that is sensed by copepod predators is the magnitude of the fluid velocity (Kiørboe and Visser, 1999; Fields and Yen, 2002). As *Euchaeta* are predators of copepods (Yen, 1983, 1985, 1991) and prey of other species, both the cues to predators and prey will be examined in this study. Hence, we will quantify the velocity, maximum deformation rate, and viscous dissipation rate fields generated by two species of predatory *Euchaeta* copepods with similar morphology and differing size: *Euchaeta rimana*, a subtropical species, and *Euchaeta elongata*, a temperate species, to provide insight to the conspicuousness to predators and prey and the cost of propulsion.

4.3 Methods

4.3.1 Animal collection and handling

Euchaeta elongata specimens were collected on a cruise off the coast of Seattle, WA, USA in May 2007. The animals were shipped overnight to the Georgia Institute of Technology in Atlanta, GA, USA. Adult specimens were sorted by hand and stored in 5 gallon containers of 30 ppt, aerated, artificial seawater at 12 ºC in a dark, environmental chamber. Flow fields for free swimming *E. elongata* specimens were collected within

five days of collection. The flow fields of *E. elongata* were collected in artificial seawater (30 ppt) at a kinematic viscosity of 1.44 mm^2 s^{-1} (8 ºC). *Euchaeta rimana* specimens were collected off the coast of the islands of Hawai'i and Oahu, HI, USA in June 2007. The specimens were sorted and kept in 19 L containers at the Natural Energy Laboratory of Hawai'i Authority in Kailua-Kona, HI, USA at room temperature (20-23 ºC) for less than a week. Flow field data were collected in filtered seawater (35 ppt) at a kinematic viscosity of 0.97 mm^2 s^{-1} (23ºC).

The experimental chamber consisted of a clear, glass tank (6 cm × 6 cm × 15 cm). For the *E. elongata* data collection, a recirculating water bath system was used to maintain the desired temperature (i.e., 8 ºC). The experimental chamber was placed inside a foam-encased larger tank (15 cm × 15 cm × 15 cm) where chilled water was passed through a Fisher Scientific chiller. The recirculation system was not used during the collection of *E. rimana* flow field data because the required fluid temperature equaled room temperature. Within the experimental chamber, the population of copepods was less than fifteen individuals. Specimens were allowed to swim freely and naturally in the chamber. On occasion, the escape behavior was initiated by introducing green laser light into the experimental chamber.

4.3.2 Velocity field data collection

The flow fields were collected with an infrared, planar Particle Image Velocimetry System (PIV) which consists of an infrared laser, two cameras, and an image acquisition system. The principle of PIV is to track the displacement of very small tracer particles via laser sheet illumination and digital imaging in order to measure the

spatial distribution of velocity vectors (Raffel et al., 1998). To visualize the flow field, the experimental chamber was seeded with titanium dioxide particles with diameter of less than 5 microns. The particles were illuminated by a pulsed infrared laser at a wavelength of 808 nm (Oxford HSI-0500, Shirley, MA, USA). Infrared illumination at 808 nm does not appear to alter zooplankton swimming behavior (Catton et al., 2007). During these experiments, the laser sheet width was 60 mm and the depth of view in the laser sheet was 0.725 mm. The time delay between pulses of the laser ranged between 6 to 9 ms and was recorded for each pass to ensure accurate velocity vectors were obtained. A digital camera (VDS Vosskühler CMC-1300, Osnabrück, Germany, 1024 x 1280 pixels) operated at a frame rate of 50 Hz captured the images of illuminated particles. The camera triggered the laser such that each laser pulse was captured on a different digital image and the time difference between an image pair was equal to the time delay of the laser pulses. Hence, image pairs were collected at a frequency of 25 Hz. A second camera (Pulnix TM-745i) was placed perpendicular to the VDS Vosskühler camera to visualize the copepods' location in the experimental chamber. Flow field data were collected when only one copepod was present in the laser sheet.

The velocity field was obtained by dividing the average displacement of the particles by the time delay between images (i.e., the time delay of the laser pulses). The average particle displacement was determined using 32 × 32 pixel interrogation subwindows with 50% overlap over the entire image. A cross-correlation function was calculated between the corresponding subwindows in each image pair. The peak of the cross-correlation function was determined to subpixel accuracy using a Gaussian fit and the particle displacement was determined by calculating the location of the peak to the

center of the subwindow. Velocity components were obtained by dividing the particle displacement in the horizontal (*X*-axis) and vertical (*Y*- or *Z*-axis) directions by the time delay between images. For cruising copepods in this study, the origin of the Cartesian grid is located at the head of the copepod such that the *X*-axis increases along the prosome of the copepod, the *Y*-axis increases along the antennae, and the *Z*-axis increases from the center of the head towards the dorsal side of the copepod (see sketch in Catton et al., 2007). Due to rapidly changing direction of copepod trajectories during escapes, an arbitrary Cartesian grid was chosen such that the *X*-axis is aligned parallel with the top and bottom of the tank and the *Y*-axis is aligned with the vertical sides of the tank (i.e., parallel to the gravity vector. Once the entire velocity field was computed, individual velocity vectors were validated by comparison to the median velocity of a 3 × 3 grid of neighboring points. Vectors outside of an acceptable range were replaced by spatially interpolated value (Westerweel, 1994; Nogueira et al., 1997). The percentage of vectors that were replaced during the filtering process ranged between 0.5 - 3%.

4.3.3 Hydromechanical cue of *Euchaeta* to prey

Kiørboe and Visser (1999) determined that velocity gradients within a flow field are the cue that triggers a response in copepod prey. The quantification of a flow field requires the assignment of a coordinate system to calculate the spatial gradients of velocity (e.g., linear and shear deformation rates). However, copepods are not necessarily aligned with the coordinate system when sensing fluid disturbances. Thus, the maximum deformation rate (E_{max}) has been used to determine the spatial extent of the hydrodynamic disturbance independent of the orientation of the copepod (Kiørboe et al.,

1999). The maximum deformation rate was calculated by finding the eigenvalues (λ_k) of the strain rate tensor (e_{ij}). The eigenvalues were determined by Equation 4.1, where det refers to the determinant of the tensor and δ_{ij} is the Kronecker delta tensor. The maximum deformation rate is the maximum absolute value of the principal axes of the deformation rate tensor (i.e., strain rate tensor) (Equation 4.2).

$$\det\left[e_{ij} - \lambda_k \delta_{ij} \right] = 0 \tag{4.1}$$

$$E_{max} = \max(|\lambda_1|, |\lambda_2|, |\lambda_3|) \tag{4.2}$$

The threshold deformation rate ranges between 0.4 s^{-1} to 6.5 s^{-1} depending on the copepod species (Fields and Yen, 1997; Kiørboe et al., 1999). In the current study, an E_{max} value of 0.4 s^{-1} was defined as the threshold value because it was the lowest value of the deformation rate that initiated a consistent escape response.

The spatial extent was quantified as a two-dimensional area for both cruising and escaping copepods. Due to a limited number of replicates of the dorso-ventral view of cruising copepods, the spatial extent of the hydromechanical cue was determined in the side view. For copepod escapes, the cue extent was calculated at t = 0.04 s with respect to the escape occurring at t = 0.0 s.

4.3.4 Hydromechanical cue of *Euchaeta* to predators

The absolute magnitude of the velocity (V) is suspected to be the fluid quantity that predators with fluid sensory capabilities use to detect prey (Kiørboe and Visser, 1999; Svensen and Kiørboe, 2000). The absolute velocity threshold that elicits the

predatory response of copepods ranges from 0.004 cm s^{-1} for *Oithonia similis* (Kiørboe and Visser, 1999; Svensen and Kiørboe, 2000) to 2 cm s^{-1} for *E. rimana* (Fields and Yen, 2002). In this study, the average background value of fluid velocity prior to the entry of a copepod into the field of view was 0.025 ± 0.015 cm s^{-1} (N = 36); hence, it was impossible to resolve meaningful descriptions of the velocity disturbance below this value. In addition, the velocity threshold of 2 cm s^{-1} was greater than the maximum velocity value observed in the cruising flow fields. Thus, a velocity threshold of 0.1 cm s^{-1} was chosen because this value is between the two thresholds stated above and clearly delineated the flow disturbance from the background flow. The area of the fluid with a velocity greater than the threshold was calculated for cruising and escapes to determine the spatial extent of the hydromechanical cue for predators.

4.3.5 Cost of propulsion

The viscous dissipation rate was calculated to estimate the cost of propulsion in copepods. A two-dimensional approximation of the viscous dissipation rate is required since the PIV system collects two dimensional flow fields (Catton et al., 2007). The viscous dissipation rate (Ψ) was calculated for units of W kg^{-1} (Equation 4.3), and this quantity was integrated over the area of the planar image and multiplied by the fluid density to obtain an estimate of the total energy dissipated in the measured plane with units of W m^{-1}.

$$\Psi = \nu\left[2\left(\frac{\partial u_x}{\partial x}\right)^2 + 2\left(\frac{\partial u_y}{\partial y}\right)^2 + 2\left(-\frac{\partial u_x}{\partial x} - \frac{\partial u_y}{\partial y}\right)^2 + 3\left(\frac{\partial u_x}{\partial y} + \frac{\partial u_y}{\partial x}\right)^2\right] \quad (4.3)$$

4.3.6 Quantifying the Reynolds number

Swimming speed data were collected from the same image files as the flow field data. The copepod velocity was calculated by measuring the displacement between images of a fixed point on the copepod. For copepod escapes only one velocity measurement was obtained due to the short residence time of the copepod in the field of view. For cruising images, five velocity measurements were measured from each pass to calculate an average value. The prosome length was calculated by measuring (in the digital images) the length from the base of the antennae to the base of the tail. The Reynolds number was calculated based on prosome length (l), swimming velocity (u_s), and kinematic viscosity (ν):

$$Re = \frac{u_s l}{\nu} \tag{4.4}$$

4.3.7 Statistical analysis

The Reynolds number, hydrodynamic conspicuousness to prey, hydrodynamic conspicuousness to predators, and cost of propulsion were compared between species for cruise and escape behavior using two-tailed, unpaired t-tests for unequal variance. A family of dependent variables was statistically compared for the Reynolds number (l, u_s, and Re), hydrodynamic conspicuousness to prey (max E_{max}, hydromechanical cue extent, and normalized cue extent), and hydrodynamic conspicuousness to predators (V_{max}, hydromechanical cue extent, and normalized cue extent). The p-values used to reject or accept the null hypothesis were adjusted for the variables within each family using a Bonferroni correction to maintain the familywise error rate. As a result, a p-value

criterion of $p < 0.0167$ was used to determine statistically significant differences between the species for Reynolds number, hydrodynamic conspicuousness to prey, and hydrodynamic conspicuousness to predators. For the cost of propulsion, $p < 0.05$ was the criterion for rejecting the null hypothesis.

4.3.8 Computational fluid dynamics model (CFD)

To gain further insight into the effect of viscosity on copepod flow fields, the flow fields generated by three prolate spheroids (major axis = 2 mm, 4 mm, 7 mm; minor axis = 1 mm, 2 mm, 3.5 mm, respectively) representing the prosome size of three species of copepods (*E. rimana, E. elongata*, and *E. antarctica*, respectively), cruising in three fluids (0°C, 8°C, and 23°C seawater) were modeled in FLUENT™. FLUENT™ is a computational fluid dynamics program that simultaneously solves the Navier-Stokes and continuity equations using a finite volume method on a collocated grid. The equations of fluid motion were solved across the finite volumes using a second order UPWIND spatial discretization for the convective terms and a central difference scheme for the diffusive terms. To find the velocity and pressure fields, the Semi-Implicit Method for Pressure-Linked Equations (SIMPLE) algorithm was employed to ensure continuity or mass conservation in the velocity field and subsequently provide the pressure field. In our study, the prolate spheroids were translated at a uniform velocity of 1 cm s^{-1} and modeled in a steady, laminar flow regime. Within FLUENT, the turbulence model was disabled and the laminar viscous model was selected.

The grid was generated in GAMBIT™ as a half ellipse in cylindrical coordinates (R, θ, X) with the major axis of the ellipse aligned with the X-coordinate and the minor axis

aligned with the *R*-coordinate (Figure 4.1). The midline of the ellipse was classified as an axisymmetric axis such that the elliptical shape was rotated by 360 degrees around the *X*-axis. Hence, the model represents the flow around a three-dimensional prolate spheroid. The extent of the computational domain was 50 times greater than the prosome length in the *R* and *X* directions and the mesh consisted of 27,416 nodes. The wall spacing of the grid was 1.2×10^{-3} wall units (y^+). The difference in estimates of the spatial extent of the hydrodynamic cue between the 27,416 node grid and a 13,708 node grid ranged from 0.5% to 1.3% for the cases with smallest and largest Reynolds numbers, respectively. The boundary conditions of the system consisted of (1) a stationary wall along the edge of the spheroid with a no-slip condition, (2) a velocity inlet condition at the edge of the positive *X*-axis with a uniform velocity of -1 cm s^{-1}, (3) a pressure outlet condition set to ambient pressure at the edge of the negative *X*-axis, (4) a zero normal velocity and zero normal gradient boundary at the edge of the domain in the positive *R*-direction, and (5) an axisymmetric axis condition at the midline of the spheroid. Streamlines, maximum deformation rate, and the cost of propulsion were determined as post-processing calculations. It is important to note that the maximum deformation rate is independent of the frame of reference (i.e., translating spheroid versus spheroid in uniform flow).

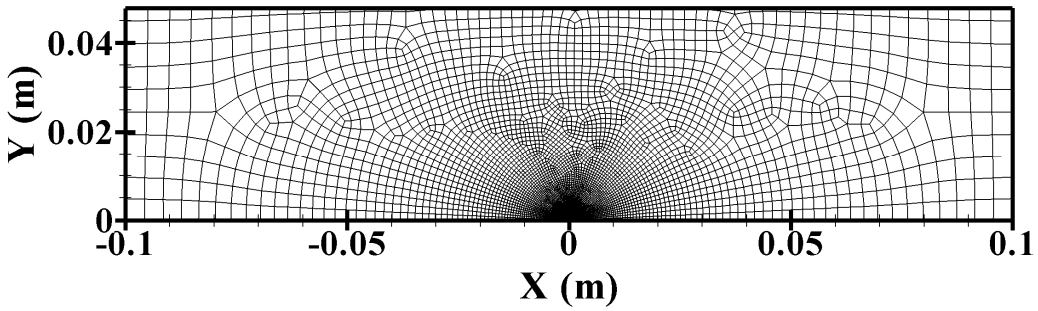

Figure 4.1 The grid for the computational fluid dynamics model of a prolate spheroid (length = 2 mm). The center of the spheroid is located at $X = 0$.

4.4 Results

4.4.1 Euchaeta swimming behavior

E. elongata is a temperate copepod species that is approximately twice as large as its subtropical congener *E. rimana* based on prosome length (Table 4.1). The two swimming behaviors that are described in this study are escaping and cruising. During cruising and escape behaviors, the average swimming velocities between species were not significantly different (Table 4.1). The Reynolds number also was not significantly different between species for either behavior (Table 4.1). The beat rate of the cephalic appendages was within 25-75 Hz for both species. To determine a more accurate beat rate and calculate the Strouhal number, a higher frame capture is needed on the high resolution camera.

Table 4.1 Swimming and flow field data for the cruising and escape behavior shown as mean ± standard error. The asterisks indicate statistically significant differences between the species.

Variable	**Cruising**		**Escape**	
	E. elongata	***E. rimana***	***E. elongata***	***E. rimana***
N	8	9	8	7
Prosome length (cm)	0.41 ± 0.01*	0.24 ± 0.01*	0.34 ± 0.02*	0.25 ± 0.02*
Swimming speed (cm s^{-1})	0.8 ± 0.1	1.0 ± 0.3	31.4 ± 4.8	27.6 ± 3.2
Reynolds number	22 ± 3	25 ± 8	890 ± 140	680 ± 80
Maximum fluid velocity (cm s^{-1})	0.54 ± 0.07	0.52 ± 0.06	2.11 ± 0.27	1.34 ± 0.23
Largest maximum deformation rate (s^{-1})	6.0 ± 0.9	6.1 ± 0.74	21.5 ± 2.4	19.2 ± 4.14

4.4.2 Cruising flow fields

The velocity fields generated by cruising *Euchaeta* in the side view (Figure 4.2 A, B) and the dorso-ventral view (Figure 4.2 C, D) are characterized by fluid converging from the area in front of the head to the swimming appendages along the anterior of the copepod. The fluid is expelled nearly symmetrically on both sides (dorso-ventral view) and primarily to the anterior side of the copepod. On average, the maximum velocities in the cruising flow field are approximately half of the swimming speeds of the copepods and not significantly different between species (Table 4.1). Qualitatively, the flow pattern around these two species of copepods during cruising is characterized by a smooth velocity field typical of moving objects at low Reynolds number rather than a turbulent flow or vortical structures that are typical of high Reynolds number flows.

The fluid disturbance sensed by *Euchaeta* prey (E_{max} field) is characterized by large values near the swimming appendages on the anterior side of the body (Figure 4.3). The cue extends farther to the sides (~3 - 5 mm) and rear of the copepod (~3 - 8 mm) than to the front of the copepod (~2 - 3 mm) (Figure 4.3). The peak values of the maximum deformation rate are not significantly different between cruising *E. rimana* and *E. elongata* (Table 4.1). The spatial extent of the hydrodynamic cue sensed by prey is also not significantly different between cruising *E. rimana* and cruising *E. elongata* (Figure 4.4 A). The normalized spatial extent of the hydromechanical cue, which is defined as the cue area divided by the copepod prosome area, is roughly twice as large for *E. rimana* compared to *E. elongata* (Figure 4.4 B). The area of the fluid disturbance sensed by *Euchaeta* predators (velocity magnitude threshold > 0.1 cm s^{-1}) and

corresponding normalized area are not significantly different between the species (Figure 4.5).

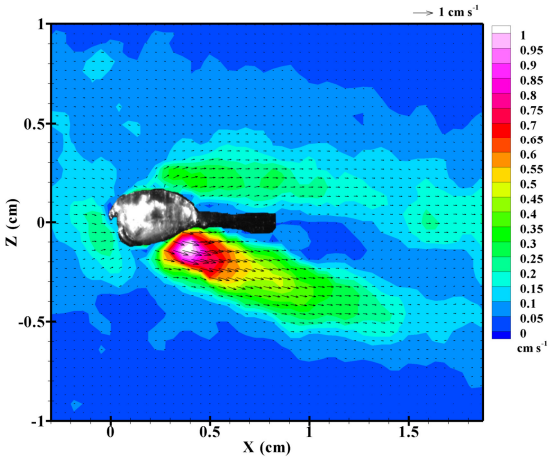

A

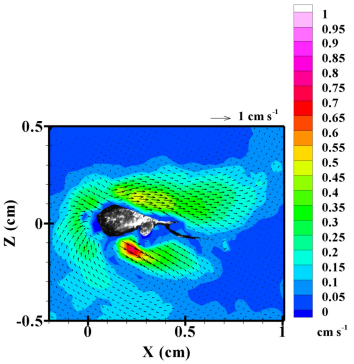

B

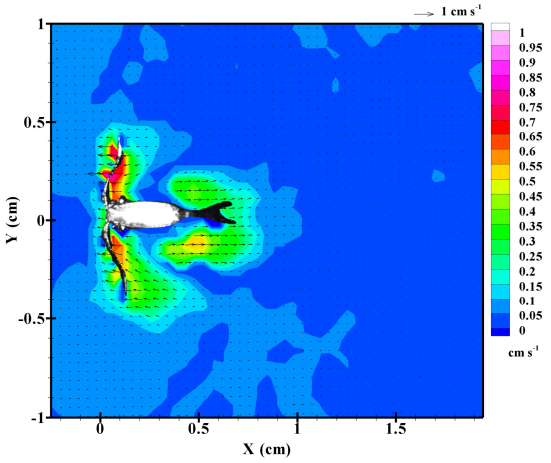

C

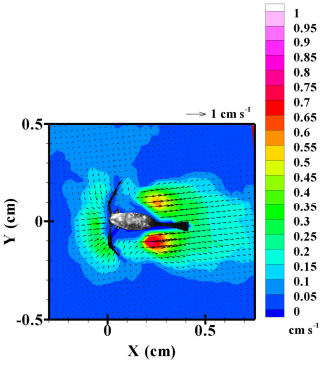

D

Figure 4.2 Instantaneous velocity fields during cruising for the side view of (A) *E. elongata* and (B) *E. rimana* and for the dorso-ventral view of (C) *E. elongata* and (D) *E. rimana*. The velocity is represented by the vectors, and the velocity magnitude is additional indicated by the color contours.

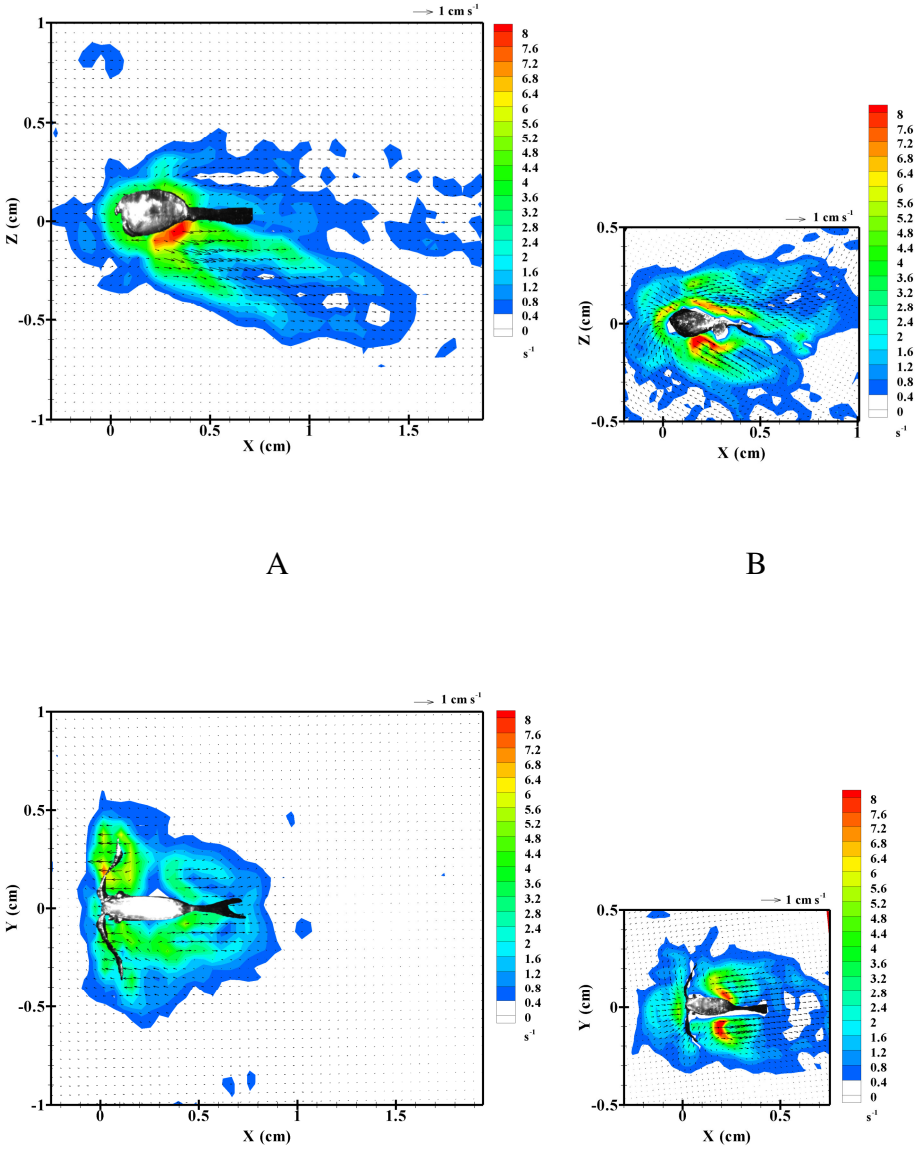

Figure 4.3 Maximum deformation rate fields for the side view of (A) *E. elongata* and (B) *E. rimana* and for the dorso-ventral view of (C) *E. elongata* and (D) *E. rimana* during cruising. The color contours represent the maximum deformation rate above a threshold of 0.4 s^{-1}. Velocity vectors are superimposed on the contour plot.

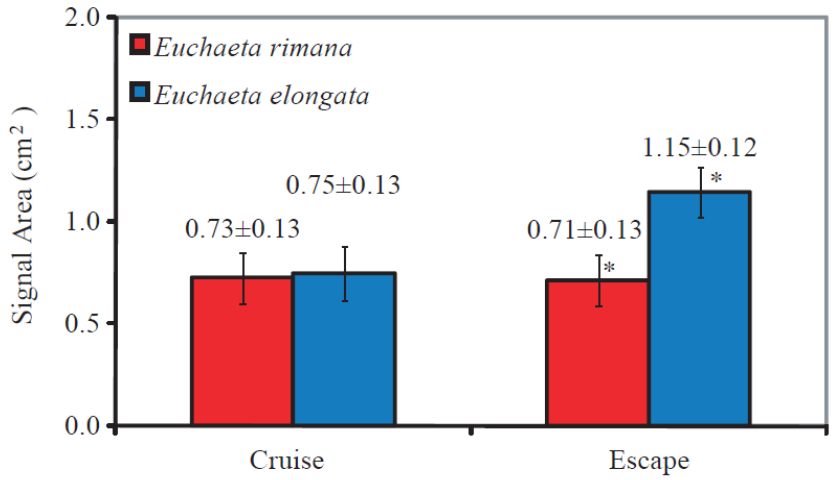

A

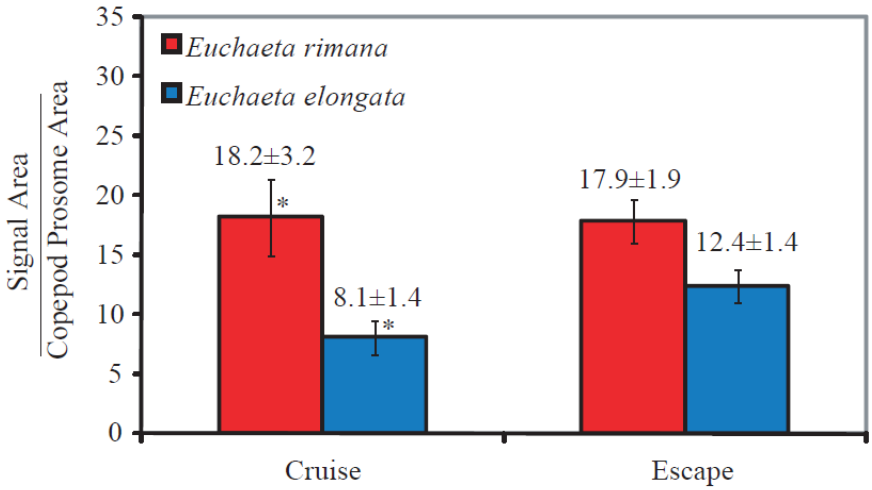

B

Figure 4.4 (A) The hydromechanical signal extent sensed by prey for cruising *E. rimana* ($N = 8$) and *E. elongata* ($N = 9$) and escaping *E. rimana* ($N = 10$) and *E. elongata* ($N = 9$) represented as a mean ± standard error. The cue extent is defined as the area of fluid disturbance with maximum deformation rate greater than 0.4 s^{-1}. (B) The cue area normalized by the copepod body area. The asterisk indicates statistically significant difference between species.

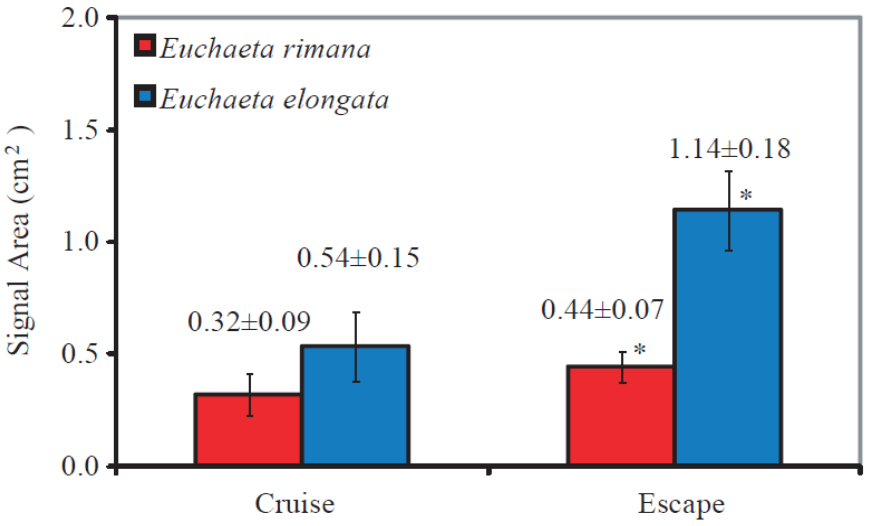

A

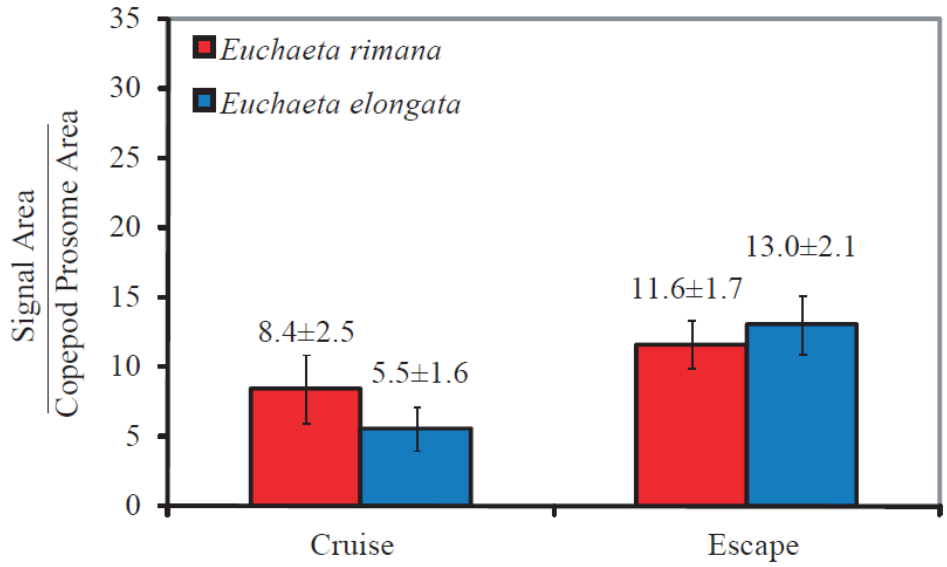

B

Figure 4.5 (A) The hydromechanical signal extent sensed by predators for cruising *E. rimana* (*N*= 8) and *E. elongata* (*N* = 9) and escaping *E. rimana* (*N* = 10) and *E. elongata* (*N* = 9) represented as a mean ± standard error. The cue extent is defined as the area of fluid disturbance with a velocity magnitude greater than 0.1 cm s^{-1}. (B) The cue area normalized by the copepod body area. The asterisk indicates statistically significant difference between species.

4.4.3Escape flow fields

Escape behavior is initiated by the contraction of the first antennae followed by an extension of the swimming legs that creates a pulsed hydrodynamic disturbance (Figures 4.6 and 4.7). The peak value of the fluid velocity in the flow field (Table 4.1) is similar between *E. elongata* and *E. rimana* flow fields. In addition, the velocity decay rate is also similar between species. The maximum velocity in the *E. elongata* flow field shown in Figure 4.6 decreased from 2.5 cm s^{-1} to 1.8 cm s^{-1} over 40 ms time period (28 % decrease) and decreased to 0.33 cm s^{-1} (87%) over 1 s. For an *E. rimana* escape shown in Figure 4.7, the maximum velocity decreased from 1.76 cm s^{-1} to 1.61 cm s^{-1} (9%) in 40 ms and decreased to 0.23 cm s^{-1} (87%) over a 1 s time period. The maximum fluid velocity is an order of magnitude smaller than the copepod escape velocity in both species. The difference between the fluid velocity and the escape velocity is much larger than expected given that the fluid immediately adjacent to the body of the copepod should be moving at a similar velocity due to the no-slip boundary condition. It is likely that the resolution of the PIV system is not fine enough to capture the high values directly adjacent to the body and the steep velocity gradient is being spatially averaged over the area of the measurement subwindow.

The hydromechanical cue perceived by prey of *E. elongata* and *E. rimana* (E_{max} > 0.4 s^{-1}) during an escape is shown in Figure 4.8. The spatial extent of the hydrodynamic cue detectable to *E. elongata* prey appears similar in size to the cue to *E. rimana* prey in Figure 4.8. However, the spatial extent of *E. elongata* cues to prey is significantly larger than that of *E. rimana* between the sample populations (Figure 4.4). In constrast, the

normalized cue extent is not significantly different between *E. elongata* and *E. rimana* (Figure 4.4). The cue that is detectable to predators of *E. elongata* is three times larger in extent than the cue detectable by predators of *E. rimana* (Figure 4.5), and the normalized cue extent was not significantly different between the species. The spatial extent of the *E. elongata* cue to predators during escapes was similar in extent to the cue to prey (comparing Figure 4.4 and Figure 4.5).

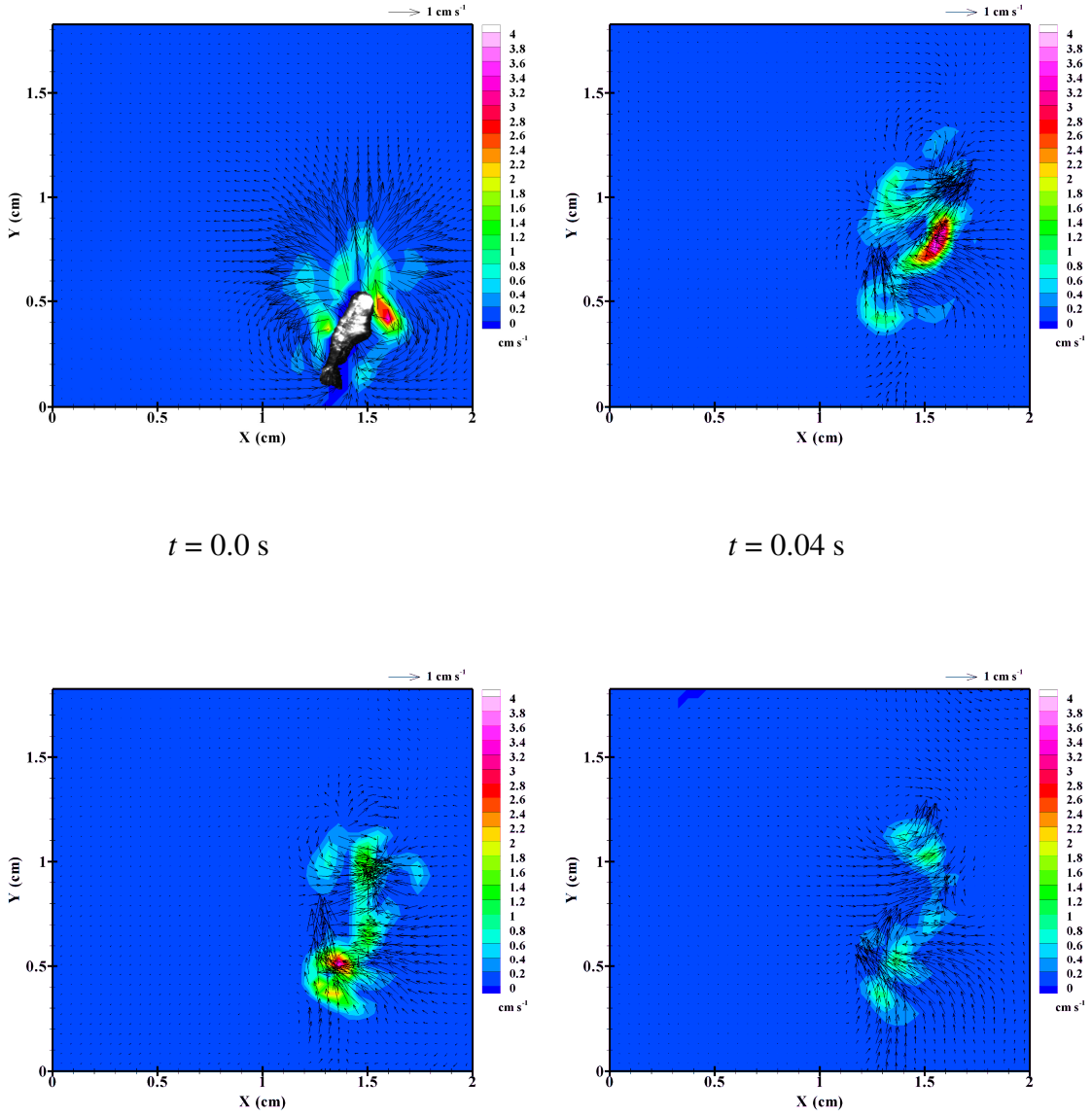

Figure 4.6 Time sequence of the instantaneous velocity field of *E. elongata* during an escape. The velocity is represented by the vectors, and the velocity magnitude is additional indicated by the color contours. The initiation of the escape occurs at $t = 0.0$ s. The copepod location is shown in (A), and the specimen leaves the field of view at $X = 2$, $Y = 1.5$ (i.e., upper right quadrant) prior to $t = 0.04$ s.

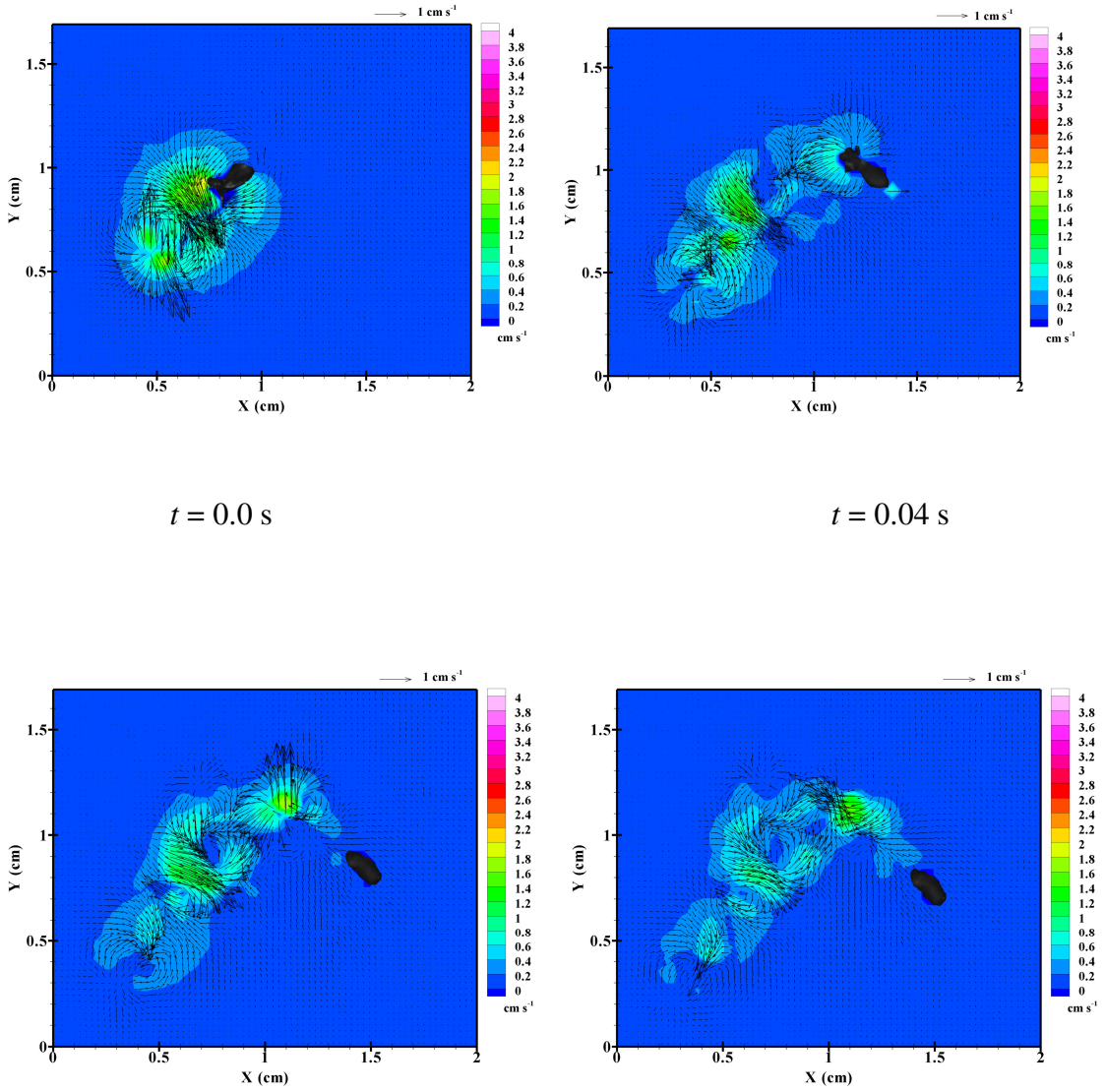

Figure 4.7 Time sequence of the instantaneous velocity field of *E. rimana* during an escape. The velocity is represented by the vectors, and the velocity magnitude is additional indicated by the color contours. The initiation of the escape occurs at $t = 0.0$ s. A second, smaller hop occurs at approximately $t = 0.04$ s. The copepod location is shown in each frame.

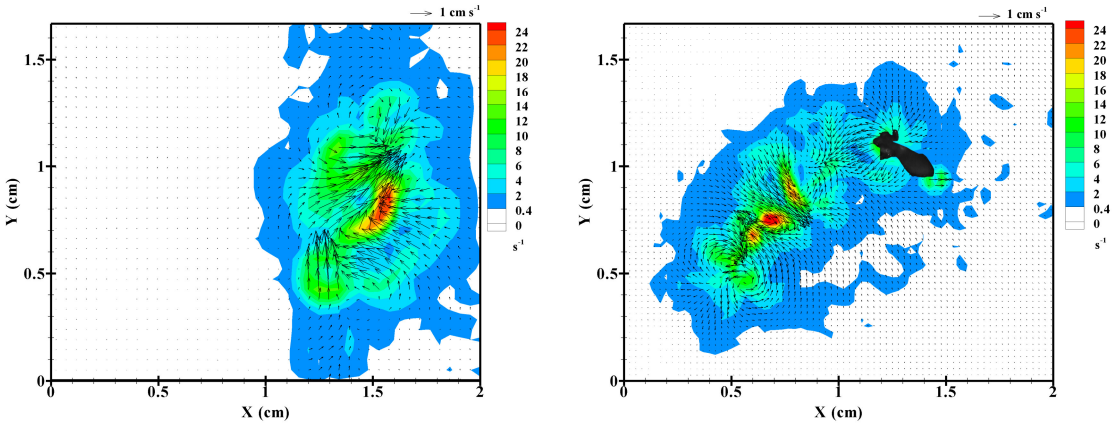

A B

Figure 4.8 Maximum deformation rate of escaping (A) *E. elongata* and (B) *E. rimana* at t = 0.04 s. The color contours represent the maximum deformation rate above a threshold of 0.4 s^{-1}. Velocity vectors are superimposed on the contour plot.

4.4.4 Cost of propulsion

The cost of propulsion is estimated by the total energy dissipated in the fluid by the copepod propulsion flow field. The viscous dissipation rate is largest along the body of cruising copepods where the largest velocity gradients are located (Figure 4.9). For escapes, the viscous dissipation rate is largest in the center of the flow disturbance and decreases towards the edges of the disturbance (Figure 4.10). The peak value of viscous dissipation rate is an order of magnitude smaller for cruising *Euchaeta* compared to escaping *Euchaeta* (Figure 4.9 versus Figure 4.10). Correspondingly, the cost of propulsion is larger for escapes than cruising (an order of magnitude larger in the case of *E. elongata*) (Figure 4.11). The increase in viscosity between tropical and temperate waters did not result in an increase in the cost of propulsion between the species for cruising. In contrast, escapes by *E. elongata* were roughly three times more costly than escapes by *E. rimana* (Figure 4.11).

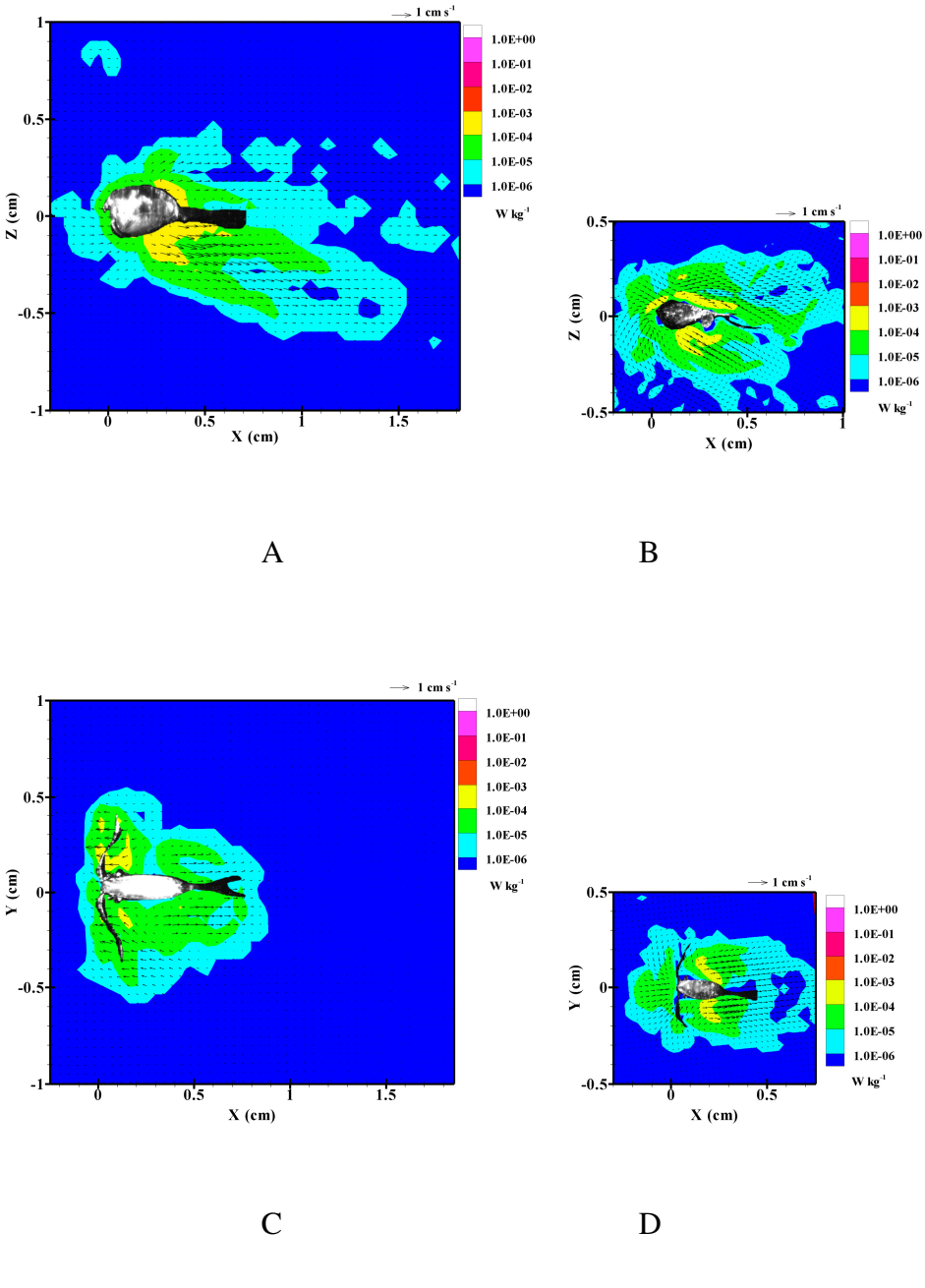

Figure 4.9 Viscous dissipation rate (W kg^{-1}) for the side view of (A) *E. elongata* and (B) *E. rimana* and for the dorso-ventral view of (C) *E. elongata* and (D) *E. rimana* during cruising. Velocity vectors are superimposed on the contour plot.

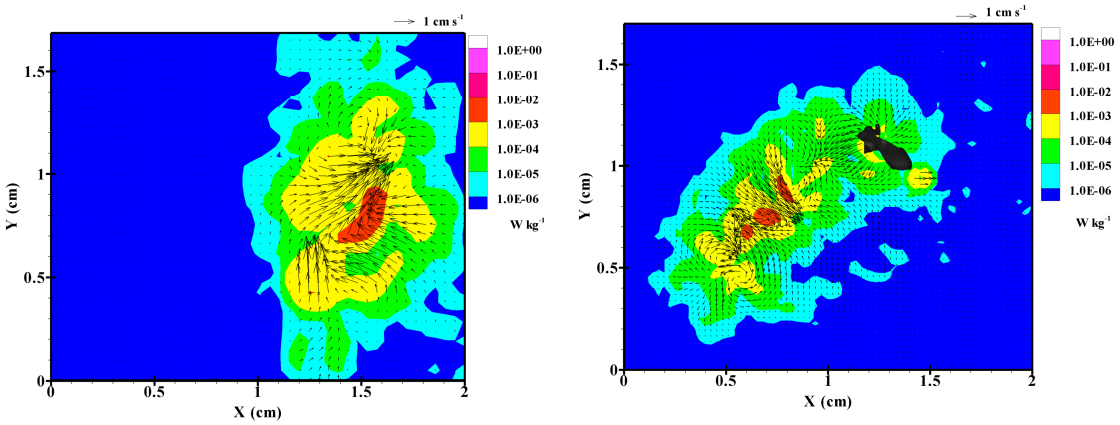

A B

Figure 4.10 Viscous dissipation rate (W kg^{-1}) of escaping (A) *E. elongata* and (B) *E. rimana* at time t = 0.04 s. The velocity vectors are superimposed on the viscous dissipation rate field.

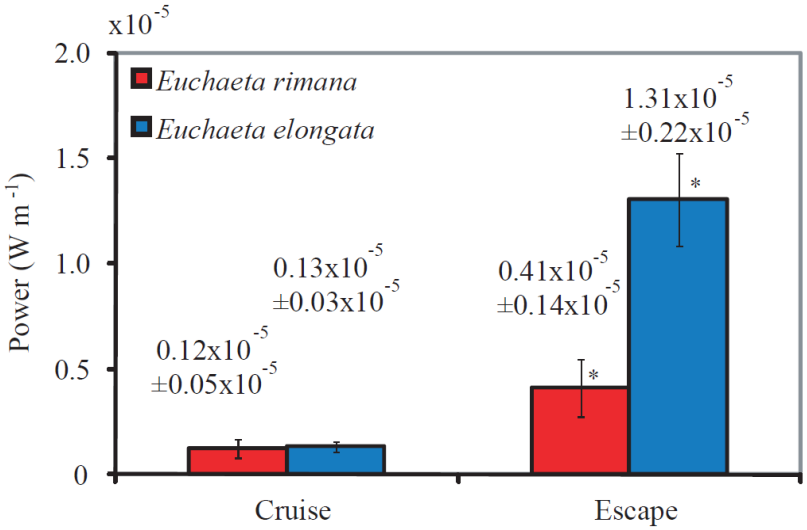

Figure 4.11 The cost of propulsion (W m^{-1}) represented as mean ± standard error for cruising *E. rimana* (*N* = 9), cruising *E. elongata* (*N* = 8), escaping *E. rimana* (*N* = 7), and escaping *E. elongata* (*N* = 7). The asterisk indicates statistically significant difference between species.

4.5Discussion

4.5.1 *Euchaeta antarctica* flow fields

The purpose of this study is to investigate the effect of varying body size and fluid viscosity on the fluid disturbances generated by *Euchaeta* species. In complement with the current data, flow fields generated by cruising *Euchaeta antarctica* (CV copepodids), which is the polar congener of *Euchaeta*, were collected in a previous study (Catton et al. 2007). An examination of the cue generated by cruising *E. antarctica* CV (prosome length of 4.2 mm) swimming at a velocity of 0.82 cm s^{-1} in 0 °C fluid (ν = 1.82 mm^2s^{-1}) provides another comparison point at a Reynolds number of 19 (N = 1). The spatial extent of the hydromechanical cue to prey in the side view of a cruising *E. antarctica* CV was 0.8 cm^2 or 9.2 times the copepodid body area. The spatial extent of the hydromechanical cue detectable to predators in the cruising side view was 0.5 cm^2 or 5.8 times the copepodid body area. Given these results, the fluid disturbance generated by cruising *E. antarctica* CV that is detected by prey species is slightly larger than the disturbance produced by both *E. elongata* and *E. rimana* (Figure 4.4); however, the normalized area of the *E. antarctica* CV cue is similar to the *E. elongata* cue. The hydromechanical cue detectable to predators is similar in absolute and normalized extent to the cue produced by *E. elongata*. The cost of propulsion for cruising *E. antarctica* CV was estimated to be 4.7×10^{-6} W m^{-1}. For cruising *E. elongata* (1.3×10^{-6} W m^{-1}) and *E. rimana* (1.2×10^{-6} W m^{-1}) the average cost of propulsion was not significantly different (from each other) and was lower than the value for *E. antarctica* CV. However,

replicates are needed from *E. antarctica* adults, rather than the juvenile CV copepodid quantified in Catton et al. (2007), to produce a conclusive statistical comparison.

4.5.2 Cruising flow fields

To assess the conspicuousness of *Euchaeta* to prey, the spatial extent of the fluid disturbance directly in front of the copepod is more relevant to the predator-prey interactions than the extents of the cue along the other parts of the copepod. The flow created by a *Euchaeta rimana* copepod has been described by particle tracking around a tethered (Lenz and Yen, 1993; Yen and Strickler, 1996) and free-swimming copepod (Yen et al., 1991). The velocity field in front of the first antennae was shown to have a peak value of 8 mm s^{-1} at the center of the copepod head. The velocity decreases along the antennae to 1 mm s^{-1} at distance of 2.5 mm from centerline near the distal tips where the longest setae are located (Lenz and Yen, 1993; Yen and Strickler, 1996). The flow field around *E. rimana* in this study was remarkably similar, except that the peak velocity at the head was approximately 4 mm s^{-1}. In predation studies with *E. rimana*, copepod prey were preferentially attacked within one body length of the *E. rimana* individual with more attacks clustered around the longest setae at the proximal section (near the head) and distal tips (Doall et al., 2002). The prey cue (E_{max} > 0.4 s^{-1}) in front of *E. rimana* extends a distance of 2 mm (roughly one body length) (Figure 4.3 D). Since the fluid disturbance is minimal in front of *E. rimana* individuals, capture success may be increased. The maximum distance of the *E. elongata* cue (E_{max} > 0.4 s^{-1}) to prey in the front of the copepod is smaller than *E. rimana* (~ 1 mm vs. 2 mm) (Figure 4.3 C). From analytical solutions of a sphere in creeping flow (Kiørboe and Visser, 1999), the

maximum distance that the cue is detectable to prey ($E_{max} > 0.4$ s^{-1}) in front of the modeled copepod is larger for *E. elongata* (5.7 mm) than *E. rimana* (4.2 mm), but in both cases the analytical solution is an overestimate of the actual cue. Compared to a sphere, *Euchaeta* appears to minimize the fluid disturbance in front of the copepod along the antennae and setae to reduce its hydrodynamic conspicuousness during predatory cruising. Additionally, the cue in front of *Euchaeta* detectable by predators appears to be very similar to the cue detectable by prey, but that may be due to the arbitrary choice of a velocity threshold.

4.5.3 Escape behavior

Until now, the flow fields of escaping copepods have not been well quantified experimentally with free-swimming organisms. Predatory copepods often attack prey in response to a fluid disturbance detected during an escape flow field (Yen, 1985; Doall et al., 2002). Thus, quantification of the copepod escape is important to understanding the capture stimulus and the consequence of escape on the copepod. Copepod escapes are expected to produce flow structures that appear more turbulent than cruising copepods because the escape Reynolds number is in the transitional flow regime where inertial forces are increasingly important. A qualitative study on the flow fields produced by free-swimming *Euchaeta* escapes (Yen and Strickler, 1996) found that toroidal vortices were shed with each jump. In the current study, the vortex identification method of Jeong and Hussain (1995) was employed on the measured velocity fields generated by an escape. No vortex cores were identified in the flow disturbance, which indicates that

while the escape flow field possesses vorticity, it does not consist of a coherent vortex structure.

Visser (2001) simulated a copepod escape with a simple impulse applied to the fluid for a finite time interval. The analytical solution showed that the size and velocity of the escape flow field change slowly over time and distance. The velocity of the simulated escape in the previous study is 90% of the initial velocity 10 ms after the escape and it was suggested that the cue would be available up to 20 seconds after the escape. Our data show that the velocity decreases at approximately the same rate between species and the cue is significantly lower after 1 second. Additionally, the spatial extent of the cue generated by *E. rimana* is significantly smaller than the cue produced by *E. elongata*. The difference in the cue is most likely due to decreased size and escape abilities of the smaller copepod since smaller copepods have been reported to jump at smaller distances during an escape (Buskey et al. 2002).

4.5.4 Effects of viscosity and size on the flow fields of translating prolate spheroids

In this study, the differences in measured flow fields between the two species could be dependent on the body size of the copepod, viscosity of the fluid, the swimming behavior, or the combination of these factors. A simple model allows us to decouple the effects of viscosity and size on the hydrodynamic disturbance of a translating prolate spheroid. The flow regime of these copepods is in the transitional regime between laminar and turbulent flow and is, therefore, not amenable to analytical solutions. A computational fluid dynamics (CFD) model allows us to solve the equations of fluid motion numerically. CFD models of three spheroids in three temperatures of seawater

that are of different viscosities (ν = 1.0, 1.44, and 1.82 mm^2s^{-1}) were generated for this study (Figure 4.12, Table 4.2). The three spheroids (major axis = 2 mm, 4 mm, and 7 mm) are sized to represent three species of *Euchaeta* (*E. rimana, E. elongata*, and *E. antarctica*, respectively). The spheroids represent cruising copepods moving at a velocity of 1 cm s^{-1}, which is close to the cruising value of all three species, through a quiescent fluid.

The flow field of the translating spheroid is produced by the application of a body force to the spheroid, whereas the copepod flow field is generated by the application of propulsive forces at the individual beating appendages to the fluid. Therefore, flow fields for the model spheroids are useful for comparison among each other, but it's important to observe that there are noteworthy differences with the actual copepod flow fields. The streamlines of the flow around the spheroid converges into the body of the spheroid near the origin and remain parallel in the flow field of the spheroid. The flow field of the spheroid is characterized by an unequal distribution of maximum deformation rate in front of and to the rear of the spheroid with peak values at the stagnation point in the front of the spheroid. The extent of the maximum deformation rate field exceeding the threshold value is shorter to the front of the spheroid and longer to the rear of the spheroid. In comparison to the spheroids, the flow fields of cruising copepods are asymmetrical (in the side view) rather than symmetrical due to the location and production of a propulsion flow from the anterior side of the cephalic region of the copepod. The peak maximum deformation rate of cruising copepods is located near the rear anterior side of the copepod rather than in front of the organism. Similar to the spheroid, the extent of the maximum deformation rate field is shorter to the front of the

organism than the rear, but the asymmetry of the flow field around the copepod results in an asymmetrical maximum deformation rate between the anterior and dorsal sides of the copepod. The spatial extent of the fluid disturbance of the spheroid (2 mm, subtropical water) is approximately half the value of the cruising *E. rimana* (mean = 0.39 (Table 4.2) vs. mean = 0.73 (Figure 4.4)). In contrast, the spatial extent of the spheroid representing *E. elongata* is slightly greater than the average value of the spatial extent of cruising *E. elongata* (mean = 0.82 (Table 4.2) vs. mean = 0.75 (Figure 4.4).

Thus, flow fields generated by the translating spheroids provide preliminary insights onto the effect of viscosity and size on copepod flow fields but a more detailed model with a similar application of the propulsive force may be needed for more concrete conclusions.

Subtropical ($\nu = 0.97$ mm s^{-1}) Temperate ($\nu = 1.44$ mm s^{-1}) Polar ($\nu = 1.82$ mm s^{-1})

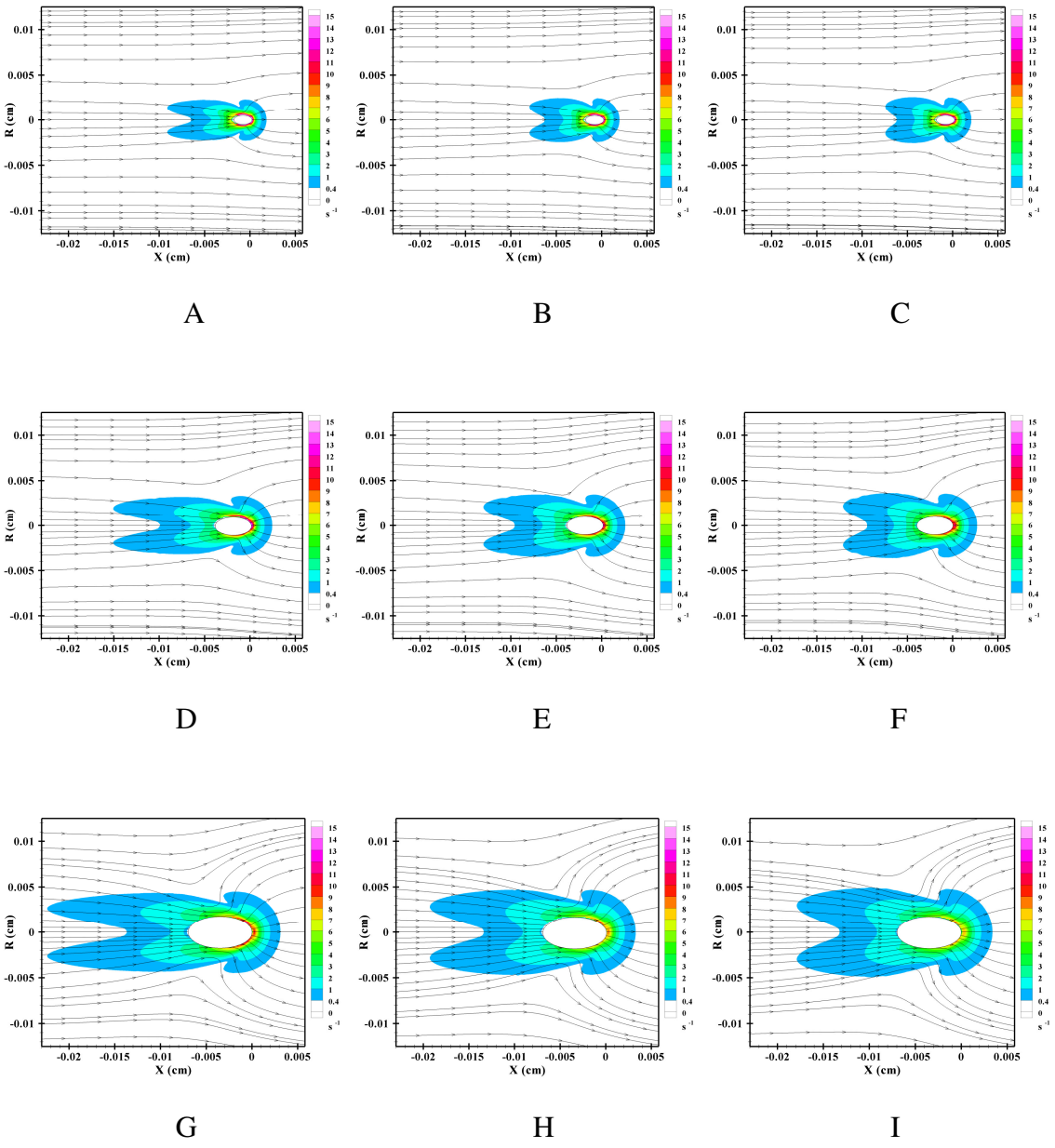

Figure 4.12 Streamlines and contours of maximum deformation rate (s^{-1}) of translating prolate spheroids representing the size of *E. rimana* ($l = 0.2$ cm) (A-C), *E. elongata* ($l = 0.4$ cm) (D-F), *E. antarctica* ($l = 0.7$ cm) (G-I) in three test fluids representing polar seawater (0°C), temperate seawater (8°C) and tropical seawater (23°C). In each case, the translation velocity is 1 cm s^{-1} in the positive X-direction, and the corresponding Reynolds numbers are shown in Table 4.2. The color contours represent maximum deformation rates above a threshold value of 0.4 s^{-1}.

Table 4.2 The Reynolds number, spatial extent of the hydromechanical cue, and two-dimensional estimate of the cost of propulsion of moving prolate spheroids representing the size of three species of copepod, *E. rimana* (l = 0.2 cm), *E. elongata* (l = 0.4 cm), and *E. antarctica* (l = 0.7 cm) in three test fluids. In each case, the translation velocity of the spheroid is 1 cm s^{-1}, which is representative of cruising speeds. The spatial extent of the hydromechanical cue is defined as the area in a two-dimensional slice of the flow where the maximum deformation rate exceeded 0.4 s^{-1}. The normalized area is shown in parenthesis and equals the cue area divided by the area of the ellipse. The two dimensional estimate of cost of propulsion is calculated by spatially integrating the viscous dissipation rate over the two-dimensional slice of the flow.

	Subtropical	**Temperate**	**Polar**
Fluid temperature (°C)	23	8	0
Kinematic viscosity (mm^2 s^{-1})	0.97	1.44	1.82
	Reynolds number		
l = 0.2 cm (*E. rimana*)	20	14	11
l = 0.4 cm (*E. elongata*)	40	28	22
l = 0.7 cm (*E. antarctica*)	70	49	38
	Cue area (cm^2)		
l = 2 mm (*E. rimana*)	0.39 (24)	0.39 (24)	0.39 (24)
l = 4 mm (*E. elongata*)	0.84 (13)	0.82 (13)	0.81 (13)
l = 7 mm (*E. antarctica*)	1.58 (8)	1.52 (8)	1.50 (8)
	Cost of propulsion ($\times 10^{-6}$) (W m^{-1})		
l = 2 mm (*E. rimana*)	6.4	8.2	9.6
l = 4 mm (*E. elongata*)	8.0	10.2	11.9
l = 7 mm (*E. antarctica*)	9.8	12.4	14.3

The effect of viscosity on the flow field is examined by analyzing the numerical solutions for each spheroid that represents a copepod species each in the three fluids of different viscosities. The shape of the flow field changes as the viscosity decreases and the Reynolds number increases. In more viscous fluids, the flow disturbance is shorter in the *X* direction (direction of the spheroid motion) and wider in the *R* direction (transverse to the flow) (Figure 4.12). The spatial extent of the flow disturbance (area of $E_{max} > 0.4$ s^{-1}) slightly decreases in more viscous fluids for two of the spheroid cases (Table 4.2) and this decrease in extent would not be accurately detectable with PIV at the present resolution. The maximum E_{max} value is consistently larger for all three size spheroids in the subtropical fluid (i.e., less viscous fluid) and has a smaller spatial extent in more viscous fluids (Figure 4.13 C). Contrary to the hypothesis that higher viscosity causes increased attenuation of the flow field, the velocity magnitude profile is steeper along the stagnation streamline at the front of the spheroid in subtropical fluid than in more viscous fluids (Figure 4.13 B). Overall, the flow fields of spheroids in higher viscous fluids have slightly decreased spatial extent (Figure 4.12), smaller peak maximum deformation rate value (Figure 4.13 C), and a less steep velocity profile (4.13 B). It is important to note that the flow field data of *E. rimana* and *E. elongata* do not exhibit the trends predicted by the comparison of spheroids in different fluids.

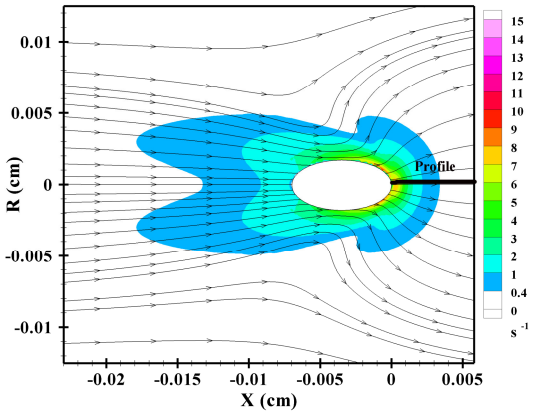

A

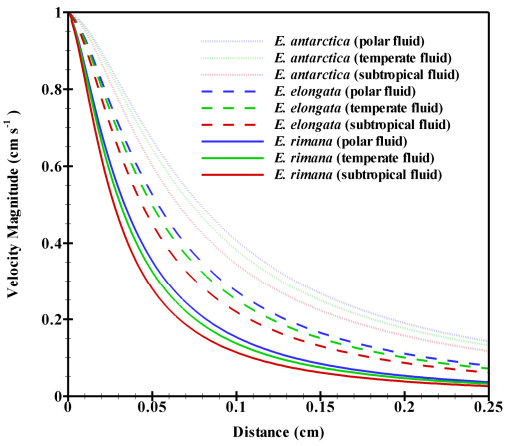

B

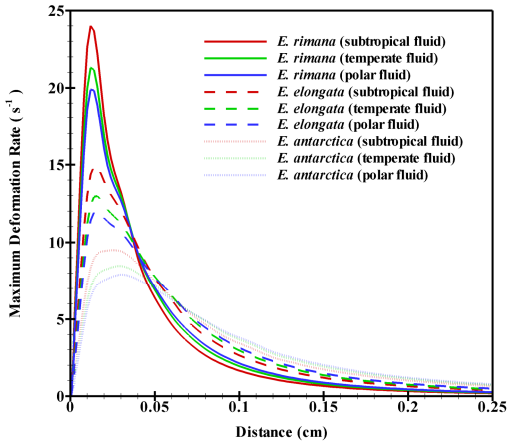

C

Figure 4.13 Profiles of (B) velocity magnitude and (C) maximum deformation rate extracted along the stagnation streamline (shown in A) at the front of the spheroid for the nine test combinations.

An increase in the size of the spheroid is associated with a proportionally larger spatial extent of a hydromechanical cue. The normalized spatial extents of the spheroids representing *E. antarctica*, *E. elongata* and *E. rimana* were 8, 13, and 24 times the area of the spheroids, respectively (Table 4.2). The normalized spatial extent of the experimental cruising copepod flow fields was equal to 9.2, 8.1, and 18.2 copepod body areas, for *E. antarctica* CV, *E. elongata*, and *E. rimana,* respectively. As the *E. antarctica* specimen is a juvenile with a prosome length of 4.2 mm, the similar spatial extent of this specimen to adult *E. elongata* is within reasonable expectations. The spatial extent approximately increases by a factor of two between *E. elongata* and *E. rimana* in both the spheroid and cruising copepod flows. However, these results were not consistent when using the absolute area calculations due to the large variation in the measurements between individual. In addition, the differences between the spheroid model and a copepod may lead to different results with respect to the relationship between the flow field spatial extent and copepod size.

Although the results of the CFD models may not be able to definitively show that the spatial extent of a hydromechanical cue is more dependent on copepod size than fluid viscosity, the model does provide insight on the effect of dynamic similarity on hydromechanical cues. Dynamic similarity is achieved when the Reynolds numbers of two objects are the same value despite differences in speed, viscosity, or size. For the modeled spheroids, dynamic similarity is nearly achieved between the 4 mm spheroid in tropical water and the 7 mm spheroid in polar water (both $Re \sim 40$). From a fluid mechanics perspective, the flow fields and profiles are self-similar (or identical) when plotted non-dimensionally. However, in the dimensional world inhabitated by organisms,

the spatial extents of the flow perturbation of the spheroids are not the same and larger spheroids have larger fluid disturbances despite dynamic similarity with smaller spheroids. In this study, the Reynolds numbers were similar between the species for both behaviors. Based on the model, the similarity in Reynolds number between copepod species does not dictate that the hydromechanical cue is equal in magnitude or spatial extent between the species.

4.5.5 Hydromechanical cue threshold

The quantification of hydromechanical cues detected by prey and predators is sensitive to the behavior threshold value. Many researchers have tried to define the fluid quantity that elicits behavioral responses in copepods with analytical fluid solutions (Viitasalo et al., 1998; Kiørboe and Visser, 1999; Visser, 2001; Svensen and Kiørboe, 2000; Buskey et al., 2002; Burdick et al., 2007), experiments in artificial flow stimuli (Fields and Yen, 1996, 1997; Kiørboe et al., 1999; Fields and Yen, 2002; Titelman, 2001; Titelman and Kiørboe, 2003), and experiments on tethered copepods (Yen and Fields, 1992). The threshold response varies depending on the definition of the flow quantity (e.g., relative velocity vs. shear vs. shear strain rate), the developmental stage of the copepod (Kiørboe et al., 1999), and the species (Fields and Yen, 1997; Kiørboe et al., 1999). Even within a species, different fluid thresholds incite different behaviors (Fields and Yen, 2002). For example, *E. rimana* will capture prey for fluid velocity greater than 2 cm s^{-1} and escape from fluid velocities greater than 18 cm s^{-1} (Doall et al. 2002; Fields and Yen, 2002). The threshold values for a copepod behavioral response determined in previous studies is often larger than the maximum values of the fluid disturbance

generated by *Euchaeta*. For instance, the threshold deformation rate is the cue that would be perceived by *Euchaeta* prey, such as *Oithonia* sp., *Calanus* sp., *Acartia* sp. (Yen, 1985), and the threshold deformation rates for these genus are 3.8 s^{-1}, 0.4 s^{-1}, and 0.38-12 s^{-1}, respectively (Kiørboe et al., 1999; Buskey et al., 2002; Burdick et al., 2007). Additionally, for *Temora longicornus*, the threshold deformation rate is greater than 15 s^{-1} (Burdick et al., 2007). The average maximum E_{max} values for cruising *Euchaeta*, in this study, ranged from 6.0 to 7.4 s^{-1} and these high values were observed within 1 - 2 mm of the copepod body. Similarly, the thresholds that have been cited for the predation response in copepods are either too small (Kiørboe and Visser, 1999; Svensen and Kiørboe, 2000) or too large (Fields and Yen, 2002) to be used to understand the cue extent of *Euchaeta.*

The large variance in behavior thresholds may be explained by the use of an artificial flow stimulus. Yen and Fields (1992) is one of the few studies that used a flow field generated by a tethered copepod to examine the escape response to a fluid disturbance and they discovered that relative velocity was the least varying fluid quantity. Also, the spatial extents of the maximum deformation rate fields (i.e., cues to prey) and the velocity fields (i.e., cues to predators) in this study are similar in many cases and the shape of the cue regions are nearly identical. This finding differs from the results of analytical solutions on creeping flow around a sphere where the velocity field has a larger spatial extent than the maximum deformation rate field (Kiørboe and Visser, 1999) and has a different shape. In addition, the assumption that maximum deformation rate is a better indicator of escape response is predicated on the fact that small prey will be entrained in a large feeding current (Kiørboe and Visser, 1999). For cruising and ambush

copepods, the feeding current is small in extent or does not exist, hence the cue to prey is not well simulated with siphon flow. Given the variance in the response thresholds obtained from artificial sources of flow, behavioral studies of response distance mapped to the flow fields obtained in this study may provide more insight to in situ copepod behavior and more realistic threshold responses.

4.5.6 Copepod sensory systems

The hydrodynamic conspicuousness of *E. rimana* and *E. elongata* to prey and predators depends on the spatial extent of their flow disturbance and also the hydromechanical cue detection ability of their prey and predators. Copepods are equipped with setal mechanosensors that sense fluid velocities as low as 20 μm s^{-1} at 1 kHz (Yen et al., 1992), but copepods do not respond with an escape or capture response to fluid velocities less than 2 mm s^{-1} (Fields et al., 2002). The setal mechanosensors are oriented in many directions along the length of the anntennule to sense fluid disturbances from all directions in a large volume. Although the spheroid model suggests that viscosity alone has only a small effect on the spatial extent of a hydromechanical cue from the production side, the effect of viscosity on the reception of the cue may still be important. Fields and Weissburg (2005) reported that tropical copepods are less sensitive to fluid velocity cues because of the decreased setal displacement in less viscous fluids. The spatial extents and maximum velocity values of cruising *E. rimana* and *E. elongata* were not statistically different. If prey species of *Euchaeta* in tropical environments have decreased sensitivity, then the large normalized spatial extent of the hydromechanical cue generated by *E. rimana* may not be as conspicuous as the flow disturbance indicates.

Therefore, a coupled approach linking the quantified fluid disturbance and the mechanosensory perception of copepods in different viscosity fluids is needed to fully examine the conspicuousness to prey and predators.

4.5.7 Cost of propulsion

The viscous dissipation rate is directly proportional to the kinematic viscosity; hence, an increase in the kinematic viscosity should be associated with an increase in the viscous dissipation rate. For cruising copepods in this study, the cost of propulsion was the same for *E. elongata* and *E. rimana* (Figure 4.11) despite the difference in fluid viscosity. The cost of propulsion was four times greater for *E. antarctica* CV (Catton et al., 2007), the polar species, than *E. rimana* and *E. elongata*. Based on the numerical simulation results, increased viscosity and increased spheroid size result in an increased cost of propulsion, as expected (Table 4.2). The cost of propulsion for the spheroids representing *E. elongata* and *E. antarctica* in their native fluid environments were 60% (l = 4 mm) and 120% (l = 7 mm) greater than the cost of propulsion for the spheroid representing *E. rimana* (l = 2 mm). The numerical solutions provide a good starting point to understanding the effect of viscosity on the dissipation rate but these solutions overestimate the cost of propulsion. The cost of propulsion from the copepod data is less because the copepods morphology may be designed to reduce drag. Between species, the cost of propulsion was different between *E. antarctica* and the other two species as expected from the larger size and effect of viscosity. An increase in the cost of propulsion was expected between *E. rimana* and *E. elongata* from the numerical study

but was not seen in the flow field data. It is possible that *E. elongata* is actively reducing energetic costs by swimming more efficiently or through other behavioral changes.

The numerical simulations do not directly address escape events since they ignore unsteady considerations. Escaping *E. elongata* experience a three fold increase in the cost of propulsion compared to escaping *E. rimana* (Figure 4.11). In general, cruising appears to be a low cost form of propulsion and escapes are more costly (10 × increase for *E. elongata*). In particular, larger copepods will expend a greater amount of energy during escapes and would benefit (at least from an energy expenditure perspective) by modulating their escape response to a higher threshold level.

CHAPTER 5

THE HYDRODYNAMIC DISTURBANCES OF TWO SPECIES OF KRILL

5.1 Summary

Krill are often found in unorganized swarms or coordinated schools depending on the species. To test if group organization is related to the hydrodynamic disturbance produced by swimming krill, we quantified the flow fields produced by *Euphausia superba* and *Euphausia pacifica*. In this study, we used infrared Particle Image Velocimetry (PIV) to analyze the structure of the hydrodynamic disturbance of free-swimming solitary specimens and small, coordinated groups of *E. superba.* The downward directed flow produced by *E. pacifica* has a smaller maximum velocity (3.4 ± 1.1 cm s^{-1} versus 6.2 ± 1.3 cm s^{-1}) and smaller horizontal extent of the flow pattern (2.2 ± 0.5 cm versus 13.8 ± 4.7 cm) compared to the flow produced by *E. superba,* which suggests that the flow disturbance is less persistent for a potential cue in the smaller krill species (*E. pacifica*). Time record analysis reveals that the hydrodynamic disturbance is very weak beyond 1 body length for *E. pacifica*, whereas the hydrodynamic disturbance is observable above the background level at 3 body length for *E. superba.* Since the separation distance of *E. superba* within a school range from 1 to 3 body lengths (from previous data), the presence of hydrodynamic perturbation appears consistently located for *E. superba.*

5.2 Introduction

Aquatic organisms routinely engage in organized, social behaviors such as schooling that can improve fitness through reduced predation rates (Burgess and Shaw, 1979), increased foraging success (Baird et al., 1991; Foster et al., 2001), and reduced energy expenditures (Hamner and Parrish, 1997; Ritz, 2000). Contrarily, there are costs to the individuals within schools including lowered food availability at certain positions within the school (Ritz and Metillo, 1998), increased risk of predation, and increased risk of disease and parasitism (Hamner, 1984). Schooling is defined by the temporal maintenance of uniform, parallel orientation by individuals within a group. Schooling behavior is more commonly observed among larger, pelagic organisms such as marine mammals, fish, and larger species of euphausiids (Hamner, 1984), whereas smaller aquatic organisms (i.e., copepods, juvenile euphausiids) more often form non-uniform aggregations or behave independently (Hamner et al., 1989). This paper aims to provide insight to schooling behavior in *Euphausia superba* and to examine the apparent influence of size by quantifying the structure of the hydrodynamic disturbance generated by two species of krill with particular focus on the orientation, extent, and strength of the hydrodynamic cue available to the nearest neighbor.

Despite having similar morphology and propulsion mechanisms, the social behavior of *Euphausia pacifica* and *E. superba* is different. *E. superba* (Antarctic krill) is an obligate schooler that migrates hundreds of kilometers (Kils, 1983; Hamner, 1984). *E. superba* schools and swarms are regularly found among all age groups and the schools are segregated into specific size, gender, moult-state, and feeding-state classes (Marr,

1962; Nicol, 1984, Johnson and Tarling, 2008). Contrarily, *E. pacifica* (Pacific krill) is a smaller species of krill that is only occasionally found in aggregations, which may be restricted to mature krill during reproduction (Endo, 1981; Nicol, 1984). Hanamura et al. (1984) observed that *E. pacifica* has the ability to form schools, but visual and in situ acoustic observations have shown that *E. pacifica* groups predominantly occur in uncoordinated aggregations or layers (Hanamura et al., 1984; de Robertis et al., 2003). Further, Zhou et al. (2005) observed that individuals of a larger species of euphausiids are more agile swimmers and able to maintain tighter, less random aggregations than smaller species of euphausiids. This observation suggests that larger krill may be better able to control their position in the environment.

Organism size mitigates propulsive ability and also dictates the spatial extent of the hydrodynamic disturbance that potentially provides a sensory field for prey, predators, and conspecifics. Krill flow fields have been identified as a source of hydrodynamic sensory cues between individuals within schools (Hamner, 1984; Wiese and Ebina, 1995; Wiese, 1996) and it is suspected that schooling krill will orient in positions within a school to receive hydrodynamic cues from their neighbors (Wiese, 1996). The dominant frequency of pressure pulses within the flow field is equal to the species-specific pleopod stroke frequency, and this dominant frequency is larger for smaller species of krill (Wiese and Ebina, 1995). Additionally, in experiments on tethered specimens, only the largest euphausiid species, *E. superba,* was found to produce a hydrodynamic cue of sufficient strength to be sensed at a distance of several body lengths (Ebina and Miki, 1996). Thus, there may be an organism size limitation for schooling due to the limited spatial extent of the sensory field. A quantitative

comparison of the flow fields of these two species from the perspective of propulsion and hydrodynamic cues may provide insight to the hydrodynamic constraints on schooling.

A few studies have been published on the flow fields generated by tethered, individual specimens of *E. pacifica* (Yen et al., 2003) and *E. superba* (Kils 1982; Ebina and Miki, 1996). However, flow fields collected from tethered krill specimens have limited value because tethering alters the behavior of the krill (personal observation) and flow fields produced by the specimen (Catton et al., 2007). To date, no studies have examined the flow fields around free-swimming coordinated groups of krill. In this study, we quantified the flow fields produced by free-swimming solitary *E. pacifica*, solitary *E. superba,* and small, coordinated groups of *E. superba* to investigate the differences in the flow field structure of these two species of krill and to provide insight to their schooling abilities. Specifically, we aim to address the following questions: (1) how does the flow regime (Reynolds number) alter the flow fields produced by the two species of krill, (2) can the propulsion-generated flow field of these two species be used as a cue to align position during schooling behavior, and (3) how does aggregative behavior alter the flow fields?

5.3 Materials and methods

5.3.1 Animal collection and care

Euphausia pacifica individuals were collected in July 2007 with a plankton tow off the continental shelf approximately 25 miles off the coast of Newport, Oregon, USA. The collected individuals were kept in a 100 liter tank located inside of a 10°C cold room at the Hatfield Marine Station in Newport, Oregon, USA for a period of two weeks

during the experiments. *Euphausia superba* individuals in this study were in culture at the Australian Antarctic Division in Kingston, Tasmania. The krill were originally collected using a rectangular, midwater trawl net in the Southern Ocean in February 2005 and March 2006 and kept onboard the RSV *Aurora Australis* in 200 liter tanks until arriving in Hobart, Tasmania (Kawaguchi et al., in press). The krill were maintained in 100 liter tanks with recirculating, chilled, filtered seawater at a temperature of 0.5 °C and salinity of 34.5 ppt. The flow field data reported herein were collected in December 2006 and January 2007.

5.3.2 Experimental setup

The flow fields generated by free-swimming euphausiids were measured using Particle Image Velocimetry (PIV) with infrared illumination. PIV is a non-intrusive flow visualization technique that quantifies a velocity field by recording the location of tiny suspended particles via a digital camera and laser sheet illumination of the measurement plane (Raffel et al., 1998, Catton et al., 2007). The velocity vector is measured by quantifying the displacement of the particles over a known time period using a pair of digital images. The PIV system consisted of an 808 nm infrared laser (Oxford HSI-500), a 1280 x 1024 pixel CMOS camera (VDS Vosskuhler CMC-1300), and an image acquisition laptop. In addition, a Pulnix TM-745i camera was located in a perpendicular orientation to the primary digital CMOS camera in order to observe the position of the krill within the laser sheet. The laser sheet was 1 mm thick and spanned a vertical distance of 80 mm. Krill behaved naturally while swimming in and near the infrared laser sheet, which is consistent with our previous observations with other zooplankton.

The time lapse between paired images ranged from 7 ms to 11 ms, and image pairs were collected at a rate of 25 hertz.

Collection of data for solitary krill was performed in a square, glass cubic tank (15 cm × 15 cm × 15 cm) that was maintained at the required temperature of 10°C (ν = 1.37 $mm^2\ s^{-1}$) for *E. pacifica* and 0.5°C (ν = 1.79 $mm^2\ s^{-1}$) for *E. superba.* The seawater in this tank was quiescent such that flow fields generated by krill could be quantified and compared between species.

The experimental setup for coordinated groups of *E. superba* is shown in Figure 5.1. In this setup, krill were visualized in a circular, white, plastic tank that was conducive to group forming and schooling behavior (tank diameter = 600 mm, tank height = 400 mm). White-colored surroundings have been shown to enhance the schooling behavior of *E. superba* resulting in tighter, more cohesive schools (Kawaguchi et al., in press). A 150 mm × 400 mm glass window was added to the tank sidewall to allow optical access. Prior to collection of flow field data, the temperature of the tank was maintained using a chilled water supply. The water supply was stopped at least 10 minutes prior to data collection, and the experiments were conducted for a time period of less than an hour such that the temperature in the tank rose by less than 1°C.

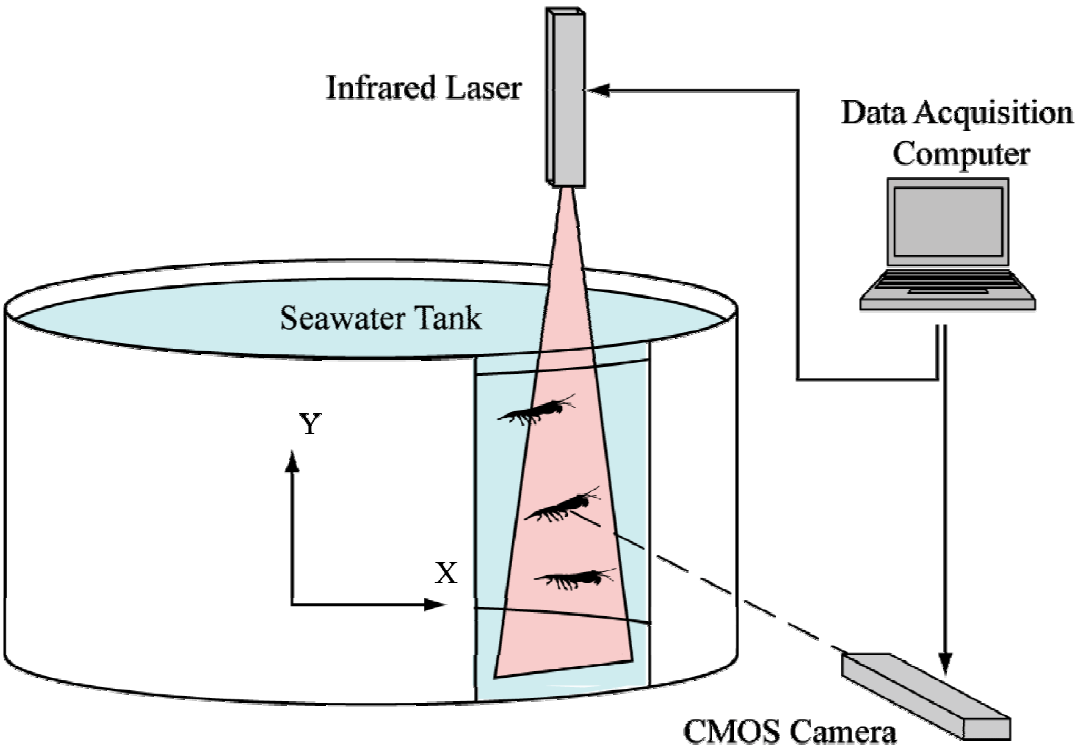

Figure 5.1 Schematic representation of the infrared Particle Image Velocimetry (PIV) setup used to visualize groups of *E. superba.* The coordinate axes are defined such that *X* is the horizontal direction and *Y* is the vertical direction.

5.3.3 Krill handling

For measurements of solitary krill, specimens were introduced individually into the measurement region through a PVC pipe (funnel) aligned with the laser sheet at a distance of 4 cm from the field of view. Typically, krill exited the pipe and swam across the tank, which increases the probability of collecting PIV data with krill swimming parallel to the laser sheet in the camera imaging region. The grouped krill data were collected in a tank that contained 100 krill swimming in coordinated groups of 3 to 6 krill.

5.3.4 Kinematics analysis

To connect krill behavior to the resulting flow field, a kinematic analysis was performed using the same digital images pairs used for the PIV analysis. The length of the krill (l) was measured in the images as the distance between the furthest extent of the antennae and tail. The swimming speed (u_s) of the krill was calculated by measuring the magnitude of the displacement of the krill over an image pair and dividing by the time lapse between the images. To reduce random error of this measurement, the swimming speed data were averaged over five images pairs for each replicate. The Reynolds number is a non-dimensional parameter used to categorize the flow regime around swimming organisms that combines the swimming speed of the organism, the length of the organism, and the kinematic viscosity of the fluid (ν):

$$Re = \frac{u_s l}{\nu} \tag{5.1}$$

The Reynolds number is a key indicator of flow stability in shear flows, and its value usually defines the transition between laminar and turbulent conditions. Previous observations indicate that euphausiids swim in a flow regime of intermediate Reynolds number (Yen et al., 2003) where the flow is neither viscous dominated nor fully turbulent.

The pleopod beat frequency (f_{beat}) was estimated from the image sequences (which were collected at a frequency of 25 hertz). The krill body angle (θ_{swim}) during swimming was calculated relative to horizontal with Equation 2, where ΔX and ΔY refer to the horizontal distance and vertical distance, respectively, between the base of the tail and the center of the eye.

$$\theta_{swim} = \tan^{-1}\left(\frac{\Delta Y}{\Delta X}\right) \tag{5.2}$$

5.3.5 Flow field calculations

The displacement of the particles between PIV image pairs was found via cross-correlation analysis. The pattern of particles within a 32 × 32 pixel region in the first image is compared to the pattern of particles in the corresponding region in the second image. The location of the peak value of the cross-correlation function relative to the center of the region corresponds to the displacement of the particles located in the region. The details of the validation and filtering algorithms used in the data analysis programs are explained in Catton et al. (2007). The planar PIV system is used to collect velocity vectors in a plane defined by the X (horizontal) and Y (vertical) directions. The symbol, u, represents the X-direction velocity component, and v represents the Y-direction

velocity component. Vorticity (ω) describes the local rotation of the fluid, and the component calculated in the measurement plane is defined as:

$$\omega = \left(\frac{\partial v}{\partial X} - \frac{\partial u}{\partial Y} \right) \tag{5.3}$$

The spatial gradients of velocity in this equation are calculated via a central difference calculation of the measured velocity field.

Wiese and Marschall (1990) and Wiese (1996) report that the antennular flow sensors of *E. superba* are highly sensitive to flow disturbances created by a vibrating objecting. Patria and Weise (2004) state that the receptor system of North Atlantic krill (*Meganyctiphanes norvegica*) is tuned to velocity at low frequency and to acceleration at higher frequency and that the threshold sensitivity for *E. superba* is 0.15 mm s^{-1}. While these studies are extremely helpful to establish that krill are sensitive to flow velocity disturbances, they do not establish the specific aspects of the flow disturbance that elicits a behavior response. In this regard, copepods show the highest correlated respond to deformation in the fluid by either shear deformation, linear deformation, or both (Fields and Yen, 1997; Kiørboe et al., 1999; Fields et al., 2002; Woodson et al., 2005). Hence, in addition to the velocity fields, we report the maximum deformation rate as an indicator of the strength of the stimulation provided by spatial gradients of the velocity field. The maximum deformation rate, E_{max}, is defined as the absolute value of the largest principal component of the deformation rate tensor (Kiørboe and Visser, 1999). Spatial gradients of velocity in the deformation rate tensor are again calculated via a central difference calculation of the measured velocity field. The quantities extracted from the flow fields

include maximum velocity, maximum vorticity, wake angle, vertical extent of the flow disturbance, and horizontal extent of the flow disturbance. The wake angle is the orientation of the core of the flow disturbance relative to horizontal. The vertical and horizontal extents of the flow disturbance are defined as the maximum distance from the rear pleopods to the point where the velocity of the flow disturbance was equivalent to the background velocity. The background velocity is defined as the average velocity magnitude of the flow field prior to entry of the krill into the field of view. For several of the data sets, the horizontal and vertical extents of the flow disturbance continued beyond of the measurement region. In these cases, a different value of *n* is noted to show the number of replicates used in the analysis. The horizontal and vertical extents of the maximum deformation rate fields were not reported separately because they were similar in value to the extents measured by the velocity field.

5.3.6 Energy dissipation rate

The cost of propulsion was estimated based on the viscous energy dissipation rate (Ψ). The energy dissipation rate (W m^{-3}) at each point in the flow field was approximated based on the measured two-dimensional velocity fields shown in Equation 5.4 and as described in Catton et al. (2007).

$$\Psi = \mu\left[2\left(\frac{\partial u}{\partial x}\right)^2 + 2\left(\frac{\partial v}{\partial y}\right)^2 + 2\left(-\frac{\partial u}{\partial x} - \frac{\partial v}{\partial y}\right)^2 + 3\left(\frac{\partial u}{\partial y} + \frac{\partial v}{\partial x}\right)^2\right] \quad (5.4)$$

To estimate the total energy dissipation rate over the three-dimensional space, the energy dissipation rate was first spatially integrated over the measured two-dimensional

field in the side view. Then, the energy dissipation was integrated over the transverse width of the flow disturbance, which was estimated to equal 0.5 cm for *E. pacifica* and 1.5 cm for *E. superba* based on the dorsal view data sets.

5.3.7 Statistical analysis

In order to compare among species and behaviors, a multivariate ANOVA (MANOVA) analyses was performed using the statistical program JMP to test the two null hypotheses:

(1) There is no difference in mean values of the kinematics variables (i.e., l, u_s, Re, f_{beat}, θ_{swim}) or flow field variables (i.e., maximum velocity, maximum vorticity, wake angle, extent of the flow perturbation, total dissipation rate) between species (*E. pacifica* versus *E. superba*).

(2) There is no difference in the mean values of the kinematics variables (i.e., l, u_s, Re, f_{beat}, θ_{swim}) or flow field variables (i.e., maximum velocity, maximum vorticity, wake angle, extent of the flow perturbation, total dissipation rate) between behaviors of *E. superba* (solitary versus coordinated group behavior).

If the null hypothesis was rejected, then a protected t-test was used to identify the variables that were significantly different between the two groups (Timm, 2002). The significant p-value was defined as $p < 0.05$ to identify statistically significant variables since only two groups were being tested.

5.4 Results

For the first time, simultaneous measurements of krill swimming kinematics and high-resolution flow fields were collected on freely-swimming krill of two species. Data were also collected on one species of krill (*E. superba*) performing two different behaviors: solitary swimming and coordinated group swimming. This section presents comparisons of swimming krill kinematics and characteristics of the flow field.

5.4.1 Krill kinematics

Table 5.1 shows the length of krill, swimming speed, Reynolds number, body angle, and pleopod beat frequency. All of these quantities were significantly different between species (*E. pacifica* versus *E. superba*). In this study, the length of *E. pacifica* individuals was approximately half of the length of *E. superba* individuals, and the *E. pacifica* swimming speed was approximately one-third of the swimming speed of *E. superba.* As a result, the Reynolds number of the swimming *E. pacifica* was roughly 4.5 times smaller than the Reynolds number of *E. superba*. Therefore, *E. pacifica* effectively swim in a more viscous flow regime compared to the larger *E. superba* despite the temperature-induced difference in the viscosity of the ambient fluid. In addition, the body angle compared to horizontal is greater (i.e., steeper orientation) for *E. pacifica*. The kinematics data match the observation during the experimental trails that the

different krill species have different swimming behaviors. During the experiments, *E. pacifica* individuals circled the tank with their body positioned at a steep vertical angle, whereas *E. superba* individuals swam in a straight line out of the funnel until the wall of the tank, where the krill dropped to the bottom of the tank.

Table 5.1 Swimming kinematics of solitary *E. pacifica*, solitary *E. superba,* and *E. superba* individuals in small, coordinated groups. Data are shown as the mean ± standard deviation. Quantities that were statistically significantly different between species and behaviors are marked with one asterisk (*) and two asterisks (**), respectively.

Species	**Solitary** ***Euphausia pacifica***	**Solitary** ***Euphausia superba***	**Group** ***Euphausia superba***
n	8	6	7
Length (cm)	2.7 ± 0.2*	5.1 ±0.5*	5.4 ± 0.3
Swimming speed (u_s) (cm s^{-1})	2.5 ± 1.5*	7.7 ± 3.3*	6.8 ± 1.2
Reynolds number	500 ± 300*	2300 ± 800*	2200 ± 400
Body orientation angle (degrees)	39 ± 14*	12 ± 7*,**	22 ± 15**
Pleopod beat frequency (beat s^{-1})	5.6 ± 0.7*	3.0 ± 0.2*,**	2.5 ± 0.2**

Unlike the species comparison above, there was no effect of behavior on the length of the length of the krill, swimming speed, and Reynolds number (

Table 5.1). However, between solitary and grouped *E. superba*, the coordinated group behavior was associated with increased body angle and decreased pleopod beat frequency. Therefore, grouped *E. superba* swim in a more vertical position with a lower pleopod beat speed to generate the same swimming speed and Reynolds number as solitary *E. superba*.

5.4.2 Flow fields

Sequences of four instantaneous, side view velocity fields generated by solitary free-swimming *E. pacifica* and *E. superba* are shown in Figure 5.2 and Figure 5.3, respectively. From the side view, the *E superba* flow field is characterized by multiple, separated regions of high downward-directed velocity produced by the beating motion of the pleopods. The high velocity regions of the flow field penetrate a small distance in the vertical direction and are not visible beyond half of one body length below the specimen. Consistently, quantifies the vertical extent of several krill flow disturbances as roughly half of one body length. The high velocity patches in the flow field persist in the horizontal direction for more than one body length behind the specimen (Figure 5.2). Consistently, quantifies the horizontal extent of the flow disturbance as roughly three body lengths. In comparison, the flow disturbance produced by *E. pacifica* consists of

only two identifiable high-velocity regions. The maximum velocity in these regions is significantly smaller than the maximum velocity in the flow field of *E. superba* ( ). As the strength of the flow disturbance decays for *E. pacifica*, the high velocity regions merge, and the flow disturbance extends approximately one body length in both the vertical and horizontal directions ( ). The dorsal view of the *E. superba* flow disturbance is again characterized by larger regions of high-velocity compared to the *E. pacifica* flow disturbances (Figure 5.4). The measured flow field in the dorsal view is particularly sensitive to the location and orientation of the measurement plane relative to the orientation of the flow field, which may lead to disparate appearance of the vector fields. The transverse width of the flow disturbance for both species of krill was roughly equal to width of the krill, hence the flow perturbation created by the krill decreases rapidly in the transverse direction (Figure 5.4).

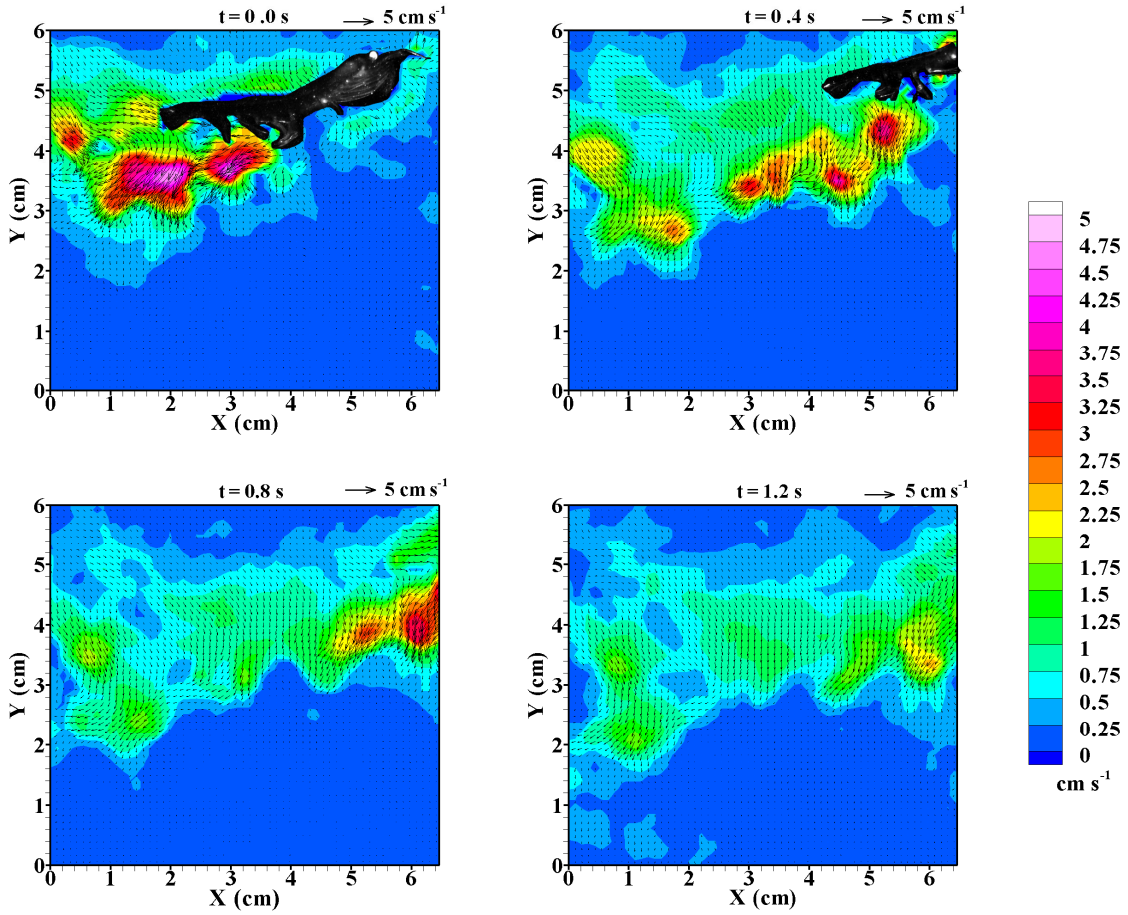

Figure 5.2 A sequence of flow fields generated by a solitary *E. superba* (side view). The velocity field is represented with vectors that indicate the direction and magnitude of the flow and color contours of the velocity magnitude (cm s^{-1}).

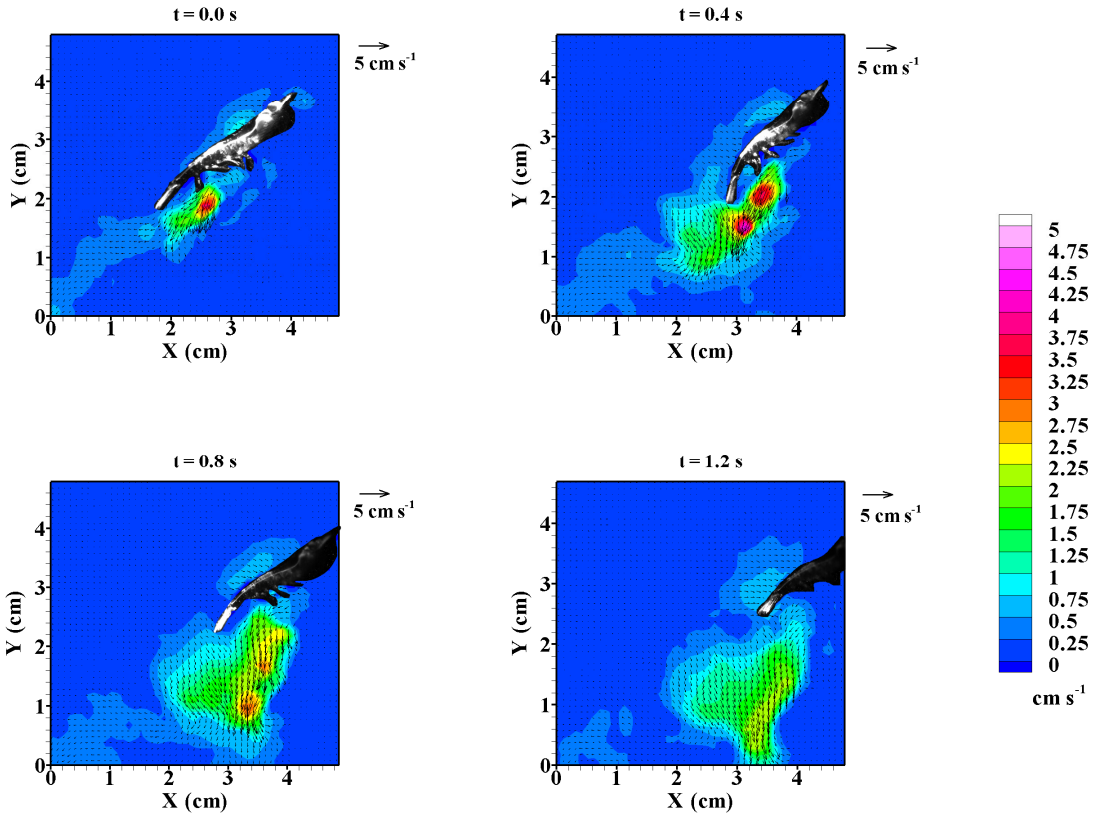

Figure 5.3 A sequence of flow fields generated by a solitary *E. pacifica* (side view). The velocity field is represented with vectors that indicate the direction and magnitude of the flow and color contours of the velocity magnitude (cm s^{-1}).

Table 5.2 Characteristics of the flow disturbance of solitary *E. pacifica*, solitary *E. superba,* and *E. superba* individuals in small, coordinated groups. Data are shown as the mean ± standard deviation. Quantities that are statistically significantly different between species and behaviors were marked with one asterisk (*) and two asterisks (**), respectively.

Species	**Solitary *Euphausia pacifica***	**Solitary Euphausia *superba***	**Group Euphausia *superba***
n	8	6	6
Maximum velocity (cm s^{-1})	3.4 ± 1.1*	6.2 ± 1.3*	6.0 ± 1.2
Maximum vorticity (s^{-1})	13.4 ± 4.6	29.9 ± 16.1	18.1 ± 7.8
Wake angle (degrees)	59 ±20	48 ± 14	38 ± 8
Vertical extent of velocity perturbation (cm)	2.1 ± 0.7	2.6 ± 1.0 [1]	3.0 ± 0.1 [2]
Horizontal extent of velocity perturbation (cm)	2.2 ± 0.5*	13.8 ± 4.7 [1] *	19.4 ± 2.2 [2]
Energy dissipation rate (Watts×10^{-6})	0.22 ± 0.13*	4.0 ± 1.6*	6.1 ± 4.7

[1] $n = 5$ due to limited spatial extent of the measurement region.

[2] $n = 2$ due to limited spatial extent of the measurement region.

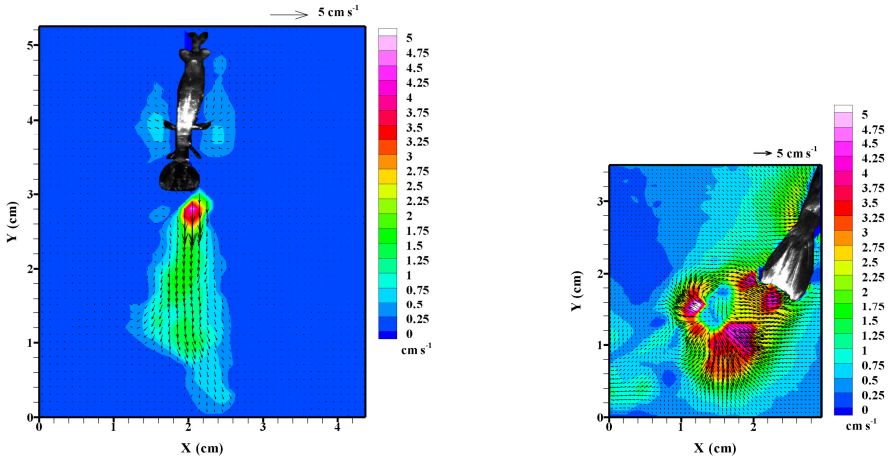

A B

Figure 5.4 Velocity fields in the dorsal view generated by (A) a solitary *E. pacifica*, and (B) a solitary *E. superba.*

The maximum value of vorticity in the flow disturbance of these two species of krill was not significantly different ( ), but the shape of the vorticity fields differed between the two species (Figure 5.5). In the case of *E. pacifica*, the regions of large positive and negative vorticity align vertically along the edges of the downward-directed jet (Figure 5.5 A). In contrast, these regions of vorticity are aligned with the horizontal direction in the flow disturbance of *E. superba* (Figure 5.5 B). From the dorsal view, there are two defined areas of opposite signed vorticity in the flow disturbance of *E. pacifica*, whereas the vorticity field in the flow disturbance of *E. superba* appears as a more complex pattern (Figure 5.5 C, D). Figure 5.6 shows the fields of maximum deformation rate, which may provide insight to the sensory field created by the flow disturbance. In the side view, the peak value of maximum deformation rate is very similar between *E. pacifica* and *E. superba*. Choosing a threshold value of 0.5 s^{-1} to define the krill flow field, the estimates of horizontal and vertical extents of the krill flow disturbances are similar to those based on the velocity field with magnitudes greater than 0.25 cm s^{-1}.

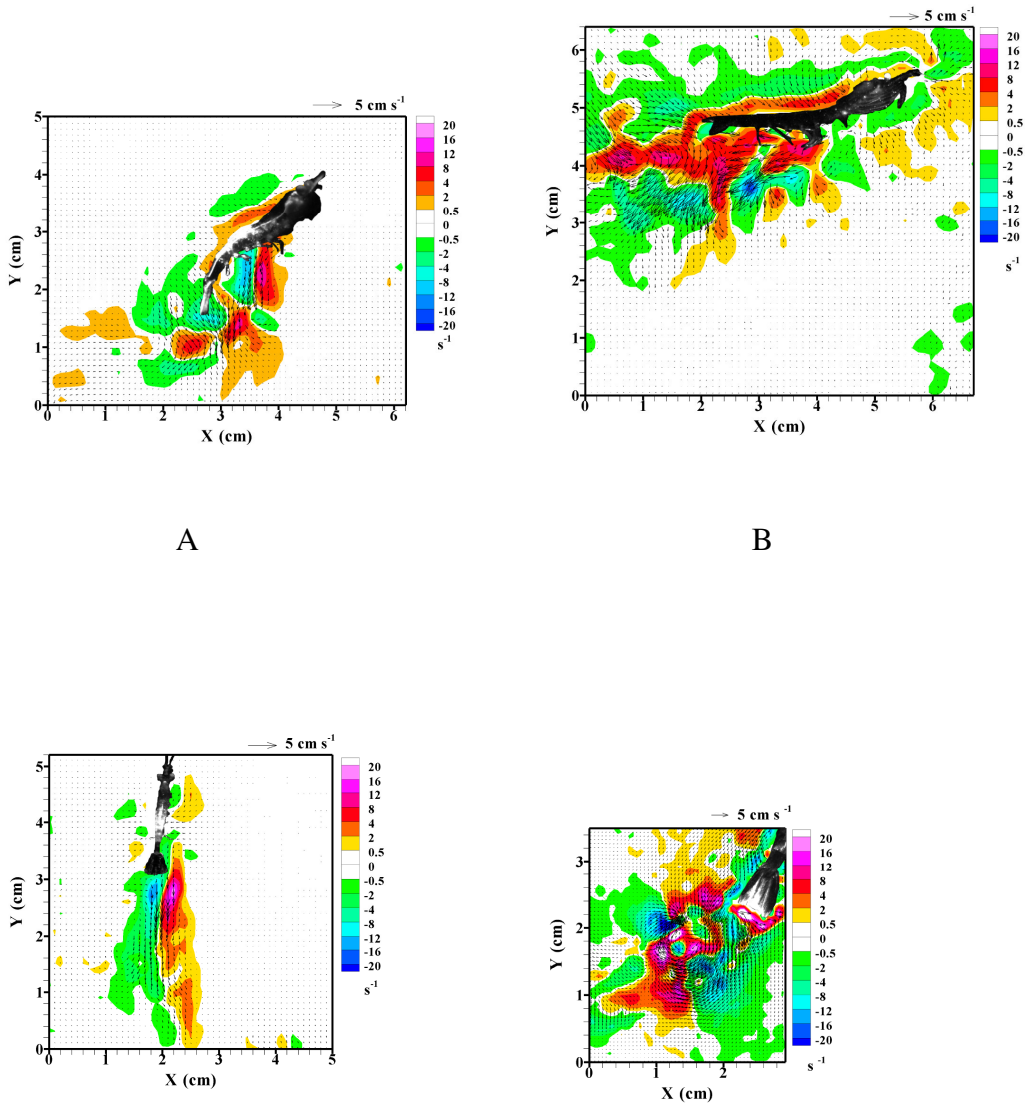

Figure 5.5 Vorticity fields in the side view of (A) *E. pacifica* and (B) *E. superba* and in the dorsal view of (C) *E. pacifica* and (D) *E. superba.* The color contours represent the magnitude of the vorticity (s^{-1}) above a threshold value of ± 0.5 s^{-1}. The superimposed vectors represent the velocity field.

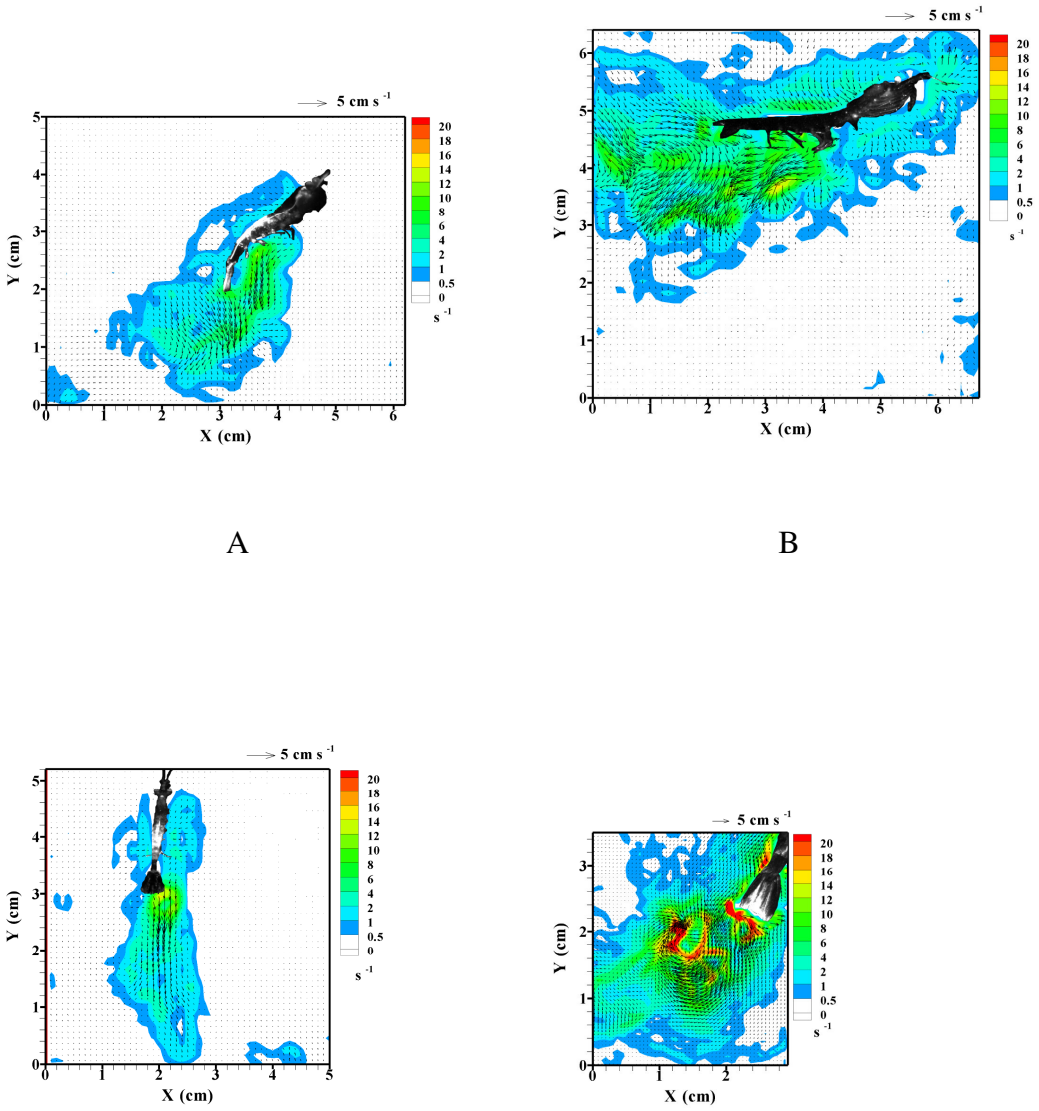

Figure 5.6 Maximum deformation rate fields in the side view of (A) *E. pacifica* and (B) *E. superba* and in the dorsal view of (C) *E. pacifica* and (D) *E. superba.* Maximum deformation rate is defined as the absolute value of the largest principal rate of deformation. The color contours represent maximum deformation rates (s^{-1}) above a threshold value of ± 0.5 s^{-1}. The superimposed vectors represent the velocity field.

Figure 5.7 shows a sequence of four instantaneous, side view velocity fields generated by *E. superba* swimming in a small, coordinated group. The maximum velocity, maximum vorticity, and wake angle were not significantly different when compared to the solitary *E. superba* flow fields ( ). Additionally, the horizontal and vertical extents of the flow fields were not significantly different in the coordinated groups of *E. superba* ( ). In most of the data sets, the horizontal and vertical extents were larger than those of solitary *E. superba* but those extents could not be accurately quantified due to the finite size of the observation region and the presence of neighboring krill. As seen in Figure 5.2 and Figure 5.7, the flow disturbance pattern produced by *E. superba* in a coordinated group is visually similar in structure to the flow disturbance of solitary *E. superba*, with several regions of high-velocity fluid located below and behind the pleopods. The negative and positive vorticity regions for the group *E. superba* were not aligned as horizontally (Figure 5.8) as for the vorticity regions generated by solitary krill (Figure 5.5). The peak value of maximum deformation rate was greater in the flow disturbances of grouped *E. superba* compared to solitary *E. superba* (Figure 5.9 versus Figure 5.6), which suggests higher shear or linear deformation rates in those flow disturbances. Since swimming speed and Reynolds number were not significantly different between the solitary and group members, few differences in the flow field structure are expected. However, it appears that the flow disturbances of individual krill in the group interact to alter the flow structure. Thus, the flow field of groups of *E. superba* is not perfectly equivalent to a flow field of superimposed solitary flow fields.

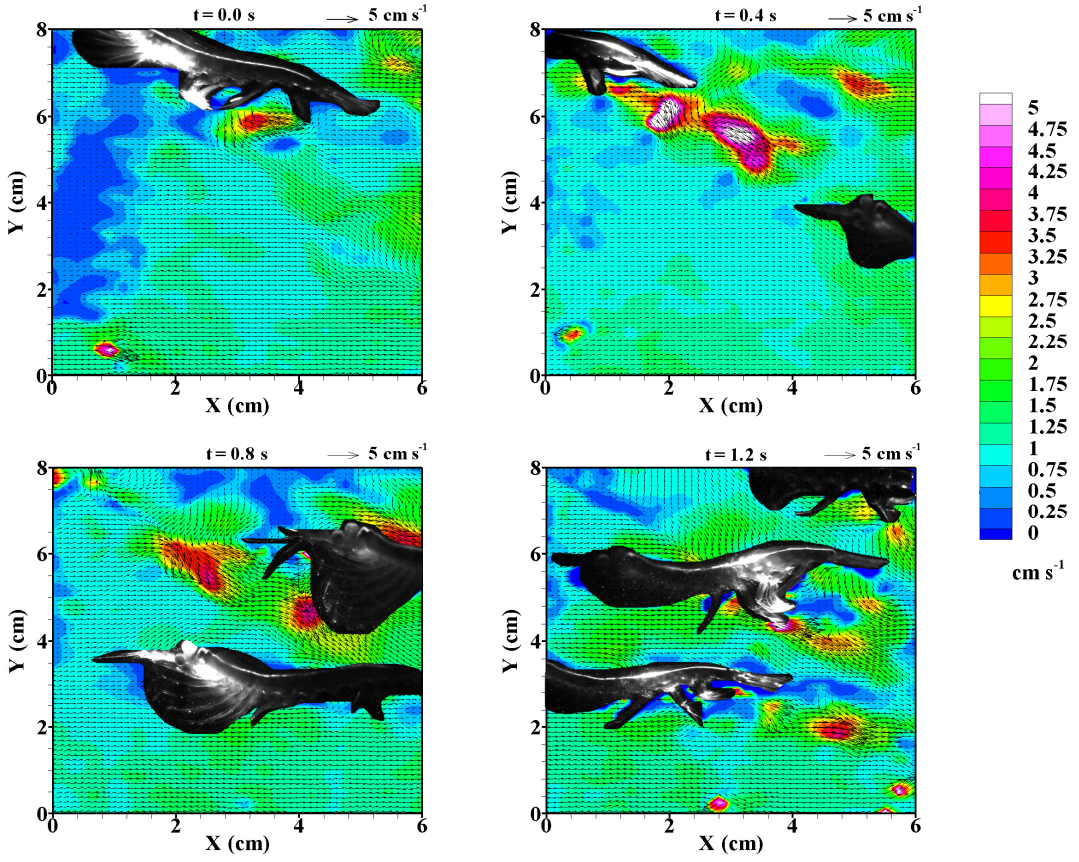

Figure 5.7 A sequence of flow fields generated by a small, coordinated group of *E. superba*. The velocity field is represented with vectors that indicate the direction and magnitude of the flow and color contours of the velocity magnitude (cm s^{-1}).

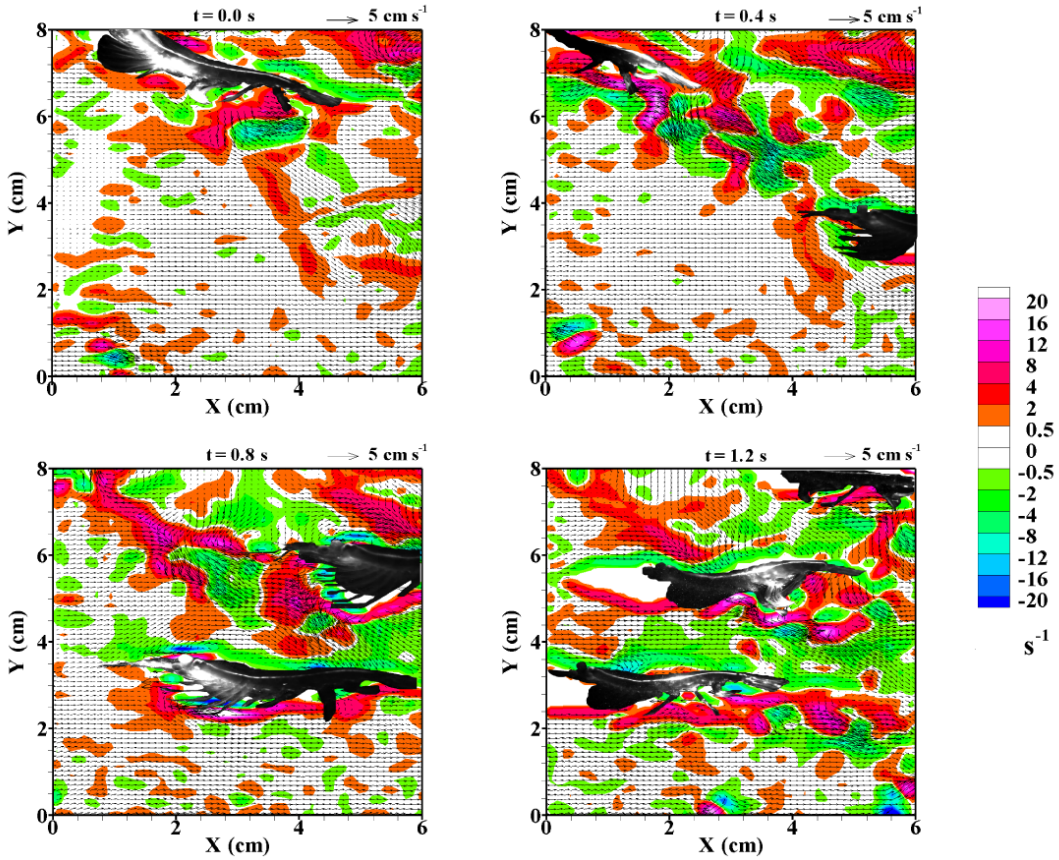

Figure 5.8 Vorticity fields of *E. superba* swimming in a small, coordinated group. The color contours represent the magnitude of the vorticity (s^{-1}) above a threshold value of ± 0.5 s^{-1}. The superimposed vectors represent the velocity field.

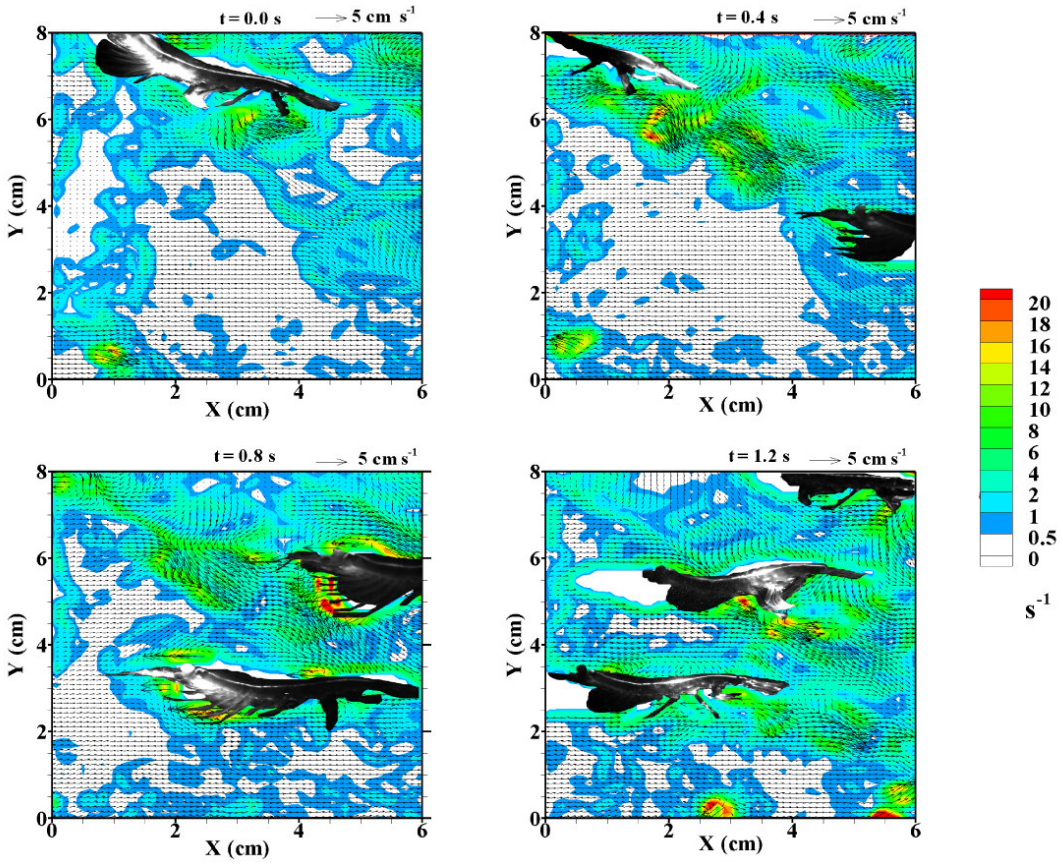

Figure 5.9 Maximum deformation rate fields of *E. superba* swimming in a small, coordinated group. The color contours represent the magnitude of the maximum deformation rate (s^{-1}) above a threshold value of ± 0.5 s^{-1}. The superimposed vectors represent the velocity field.

5.4.3 Cost of propulsion

The energy dissipated in the flow disturbance of solitary *E. pacifica* was an order of magnitude smaller than the energy dissipated by solitary *E. superba* individuals (2.2×10^{-7} W versus 4.0×10^{-6} W) ( ). Based on these calculations, the energy dissipated in the flow disturbance of individuals in coordinated groups was not significantly different than the energy dissipated in the flow disturbance of the solitary *E. superba* ( ).

5.4.4 Time series analysis

Time series of velocity, vorticity, and maximum deformation rate were extracted from the flow fields in a moving frame of reference that represented a krill swimming at a set distance and angle behind the krill generating the flow field. The time series were extracted at a set of points defined by distances of 0.5, 1, 2, and 3 body lengths behind the swimming krill and at nearest neighbor elevation (NNE) angles of 0, 15, 30, 45, and 60 degrees from horizontal (Figure 5.10). This set of points was translated in space with the reference krill such that the points always remained at the original distance and angle relative to the reference krill position. The time records, therefore, correspond to the flow perturbation, which is potentially available to a neighbor as a hydrodynamic cue, at the particular point of extraction.

Figure 5.11 and Figure 5.12, respectively, show the velocity and maximum deformation rate records at the described locations. The time records of vorticity are not shown because they qualitatively follow the same trends observed in Figure 5.12. To highlight the distances and angles that have a significant hydrodynamic perturbation, a

background noise level was identified with a red background. Background noise levels for the velocity series (V) were identified by measuring the average velocity magnitude of the flow field prior to the entry of the krill ($V < 0.1$ cm s^{-1} for solitary *E. pacifica*, $V < 0.2$ cm s^{-1} for solitary *E. superba*, and $V < 0.6$ cm s^{-1} for group *E. superba)*. The significant hydrodynamic perturbation was interpreted as the velocity measurements that exceeded the background noise level. The threshold level for the maximum deformation rate was arbitrarily set at 0.5 s^{-1} in order to be consistent with the sensitivity of other zooplankton.

For *E. pacifica*, the most robust velocity perturbation was located at a position of NNE of 60 degrees (which agrees with the wake angle reported in) and a distance of less than 2 body lengths from the individual. The flow perturbation also was evident at a NNE of 45 degrees at distances less than 2 body lengths. Consistently, the time series of maximum deformation rate show perturbations at the same positions and all maximum deformation rates were below the threshold beyond 2 body lengths.

Strong velocity and deformation rate perturbations in the flow field of *E. superba* were located at an orientation of NNE of 15 degrees and a distance of at least 3 body lengths from the reference krill. In order for grouped *E. superba* to use a hydromechanical perturbation for cues, a preferential position is 15 degrees and roughly less than three body lengths (note that we do not have data beyond this distance to evaluate the cue strength at greater distances). Power spectra calculated from the time series of velocity magnitude reveal a peak of energy at approximately 3 Hz (for positions less than 3 body lengths), which agrees with the pleopod beat frequency for *E. superba*

(Table 5.1). In contrast, power spectra calculated based on the time records collected in the flow field of *E. pacifica* do not show a peak of energy at a specific frequency.

In the velocity field around the coordinated group, it is difficult to separate the background flow field produced by the general movement of the group from the cue produced by one krill within the group (Figure 5.7). As a consequence, the time records extracted for the group *E. superba* reveal a larger flow perturbation compared to the solitary specimen (Figure 5.11 and Figure 5.12). The peak perturbation appeared at a NNE orientation of 0 degrees and all NNE orientations shown had significant velocity perturbations.

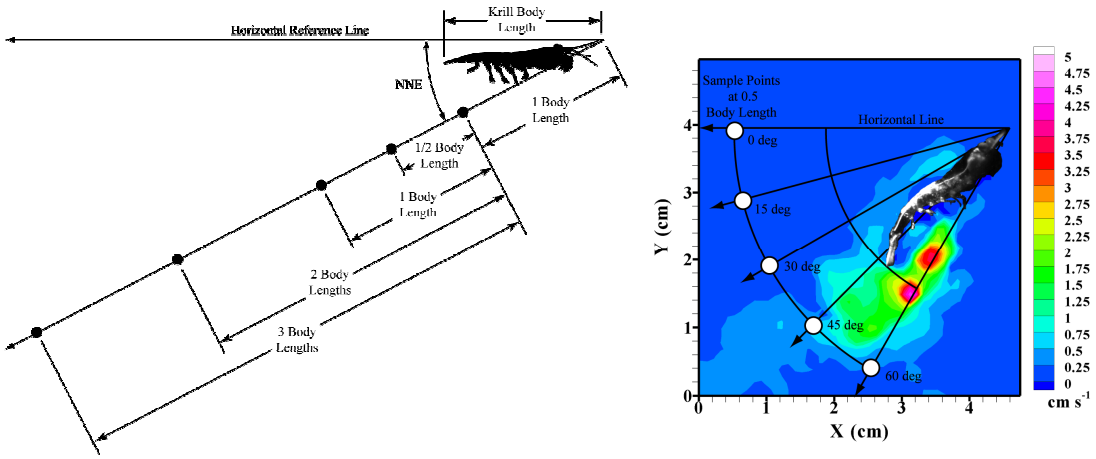

A B

Figure 5.10 Two schematics of the locations of the extracted time records of velocity and maximum deformation rate. Data were extracted for nearest neighbor distances (NND) that correspond to 0.5, 1, 2 and 3 body lengths beyond the tail of the krill (shown in A). Data were extracted for nearest neighbor elevation (NNE) angles ranging from 0 to 60 degrees from horizontal (shown in B). The extraction locations move with the reference krill in order to simulate the perspective of another krill following at the same velocity magnitude and direction.

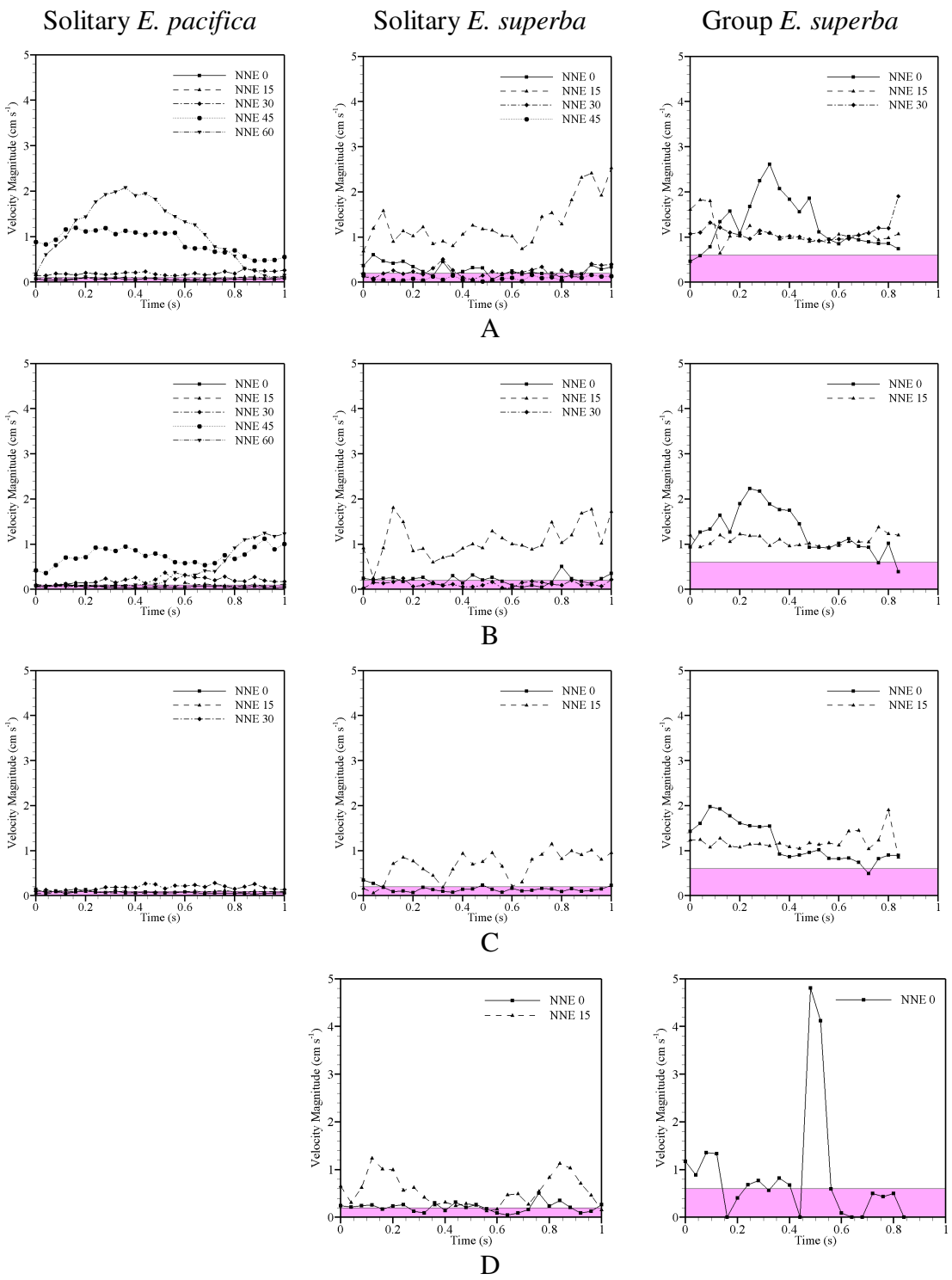

Figure 5.11 Time records of the velocity magnitude at (A) 0.5, (B) 1, (C) 2, and (D) 3 body lengths behind free-swimming, solitary *E. pacifica,* solitary *E. superba,* and *E. superba* in a group. The velocity time record was unavailable for solitary *E. pacifica* at a distance of three body lengths. Background velocity levels are marked by the red region for values of 0.1, 0.2, and 0.6 cm s^{-1} for solitary *E. pacifica*, solitary *E. superba* and group *E. superba,* respectively.

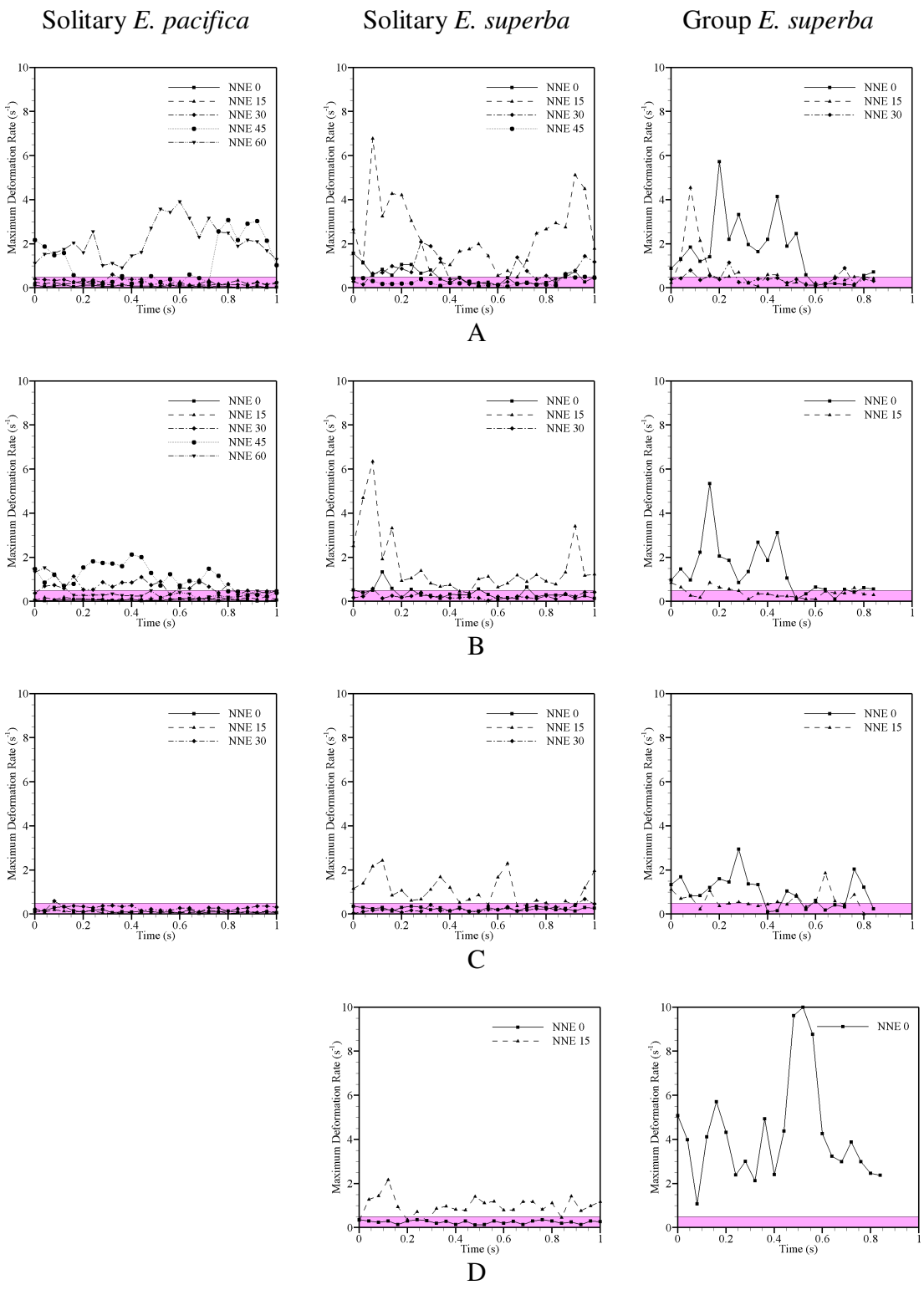

Figure 5.12 Time records of the maximum deformation rate at (A) 0.5, (B) 1, (C) 2, and (D) 3 body lengths behind free-swimming, solitary *E. pacifica*, solitary *E. superba,* and *E. superba* in a group. The red region marks a threshold value of 0.5 s^{-1}.

5.5 Discussion

5.5.1 Swimming kinematics

Accurate assessments of the propulsive and sensory limitations of krill require that the behavior of the krill in this laboratory study match the behavior of krill in situ. In this study, we collected data on free-swimming krill performing pleopod swimming at mean swimming speeds of approximately 2.5 cm s^{-1} (*E. pacifica*) and 7 cm s^{-1} (*E. superba*), which are similar to the swimming speeds of solitary *E. pacifica* and horizontal schooling *E. superba* measured in situ at 1.8 cm s^{-1} (de Robertis et al., 2003) and between 3 and 15 cm s^{-1} (Hamner, 1984), respectively. *E. pacifica* swim at lower swimming speeds at a steeper body angle than solitary *E. superba*. *E. pacifica* swim at oblique trajectories of less than 60 degrees (de Robertis et al., 2003), while the body angle of *E. superba* was typically horizontal (Hamner, 1984). In conclusion, the behavior of krill in this study was similar to field observations and is suitable for further discussion.

The swimming behavior of *E. pacifica* and *E. superba* has been analyzed in laboratory studies but none of these studies directly compared the swimming behavior to the resulting flow fields for these two species. In previous laboratory studies, the average swimming speeds of *E. superba* and *E. pacifica* during laboratory studies of pleopod swimming were 6 cm s^{-1} (Kils, 1979a, 1979b) and less than 2 cm s^{-1} (Miyashita et al., 1996), respectively. However, some studies found steeper body angles (Endo, 1993; Kils, 1982) than our study because these studies observed krill during hovering rather than during pleopod swimming. Miyashita et al. (1996) found that the swimming speed

of *E. pacifica* is inversely related to swimming angle, such that hovering krill will have larger swimming angles than faster swimming krill.

5.5.2 Flow fields

Past studies on euphausiid flow fields are limited to studies of tethered specimens of *Meganyctiphanes norvegica* (Kils, 1982; Patria and Wiese, 2004), *Euphausia pacifica* (Yen et al., 2003), *Euphausia superba* (Ebina and Miki, 1996). Tethered specimens generate flow fields with higher velocities and more rotation in the flow (Catton et al., 2007) because the tether imparts an unbalanced force on the fluid. Therefore, studies on tethered specimens do not provide an accurate representation of the induced flow fields. The free-swimming *E. pacifica* flow field more closely resembled the findings of tethered studies with a distinct downward directed jet (Kils, 1982; Yen et al., 2003; Patria and Wiese, 2004), whereas the fluid disturbance produced by each stroke of the pleopods was more apparent in the *E. superba* flow fields. Unlike the study by Patria and Wiese (2004), the larger species (*E. superba*) did not produce vortex rings from the side view, which suggests the observed vortex rings were an artifact of the aquarium or tethering in their study. Patria and Wiese (2004) identified the vortex as a potential benefit to propulsion because well positioned krill could take advantage of regions of flow disturbances that have an upward and forward moving component. Since coherent rings do not appear in the flow disturbances in our study, it is unlikely that larger free-swimming krill gain any propulsive advantage from such rings.

The Reynolds number around a free-swimming, solitary *E. superba (Re* ~ 2300*)* is more than four times larger than the Reynolds number for a solitary *E. pacifica (Re* ~

500). These findings are supported by previous studies that estimated Reynolds number of *E. superba* as ranging between 500 – 3000 (Swadling et al., 2005) and *E. pacifica* as 175 (Yen et al., 2003). It should be noted that the average Reynolds number of *E. pacifica* in our study was 265 when calculated using the method in Yen et al. (2003). The Reynolds number is generally interpreted as the non-dimensional ratio of inertial forces to viscous forces, and the value compared to unity indicates the relative importance of these effects. Marine organisms swim at a range of flow regimes from viscosity-dominated flow regimes ($Re \leq 1$), through intermediate flow regimes with both viscous and inertial forces acting on the organism, to inertia-dominated flow regimes where viscous drag is restricted to a thin boundary layer adjacent to the organism body ($Re >> 1000$). The Reynolds numbers in our study are representative of an intermediate flow regime.

In our study, the flow field produced by *E. pacifica* was characterized by lower maximum velocities and smaller horizontal extent. The larger swimming speed exhibited by *E. superba* accounts for the increase in maximum velocity in the flow disturbance. In addition, the decreased body angle and increased Reynolds number explain why the flow disturbancewake pattern of *E. superba* is more directed in the horizontal direction and has more irregular and persistent flow features.

5.5.3 Energy expenditure

When comparing energy expenditure, the energy dissipated in the flow field of *E. superba* was an order of magnitude greater than the energy dissipated in the flow field of *E. pacifica*. As swimming speed and body length are greater in *E. superba*, the increase

in energy expenditure was expected. The energy expended during propulsion is estimated to be 73% of a krill's metabolic expenditure (Swadling et al., 2005) and energy consumption has been measured through oxygen consumption for a variety of kinematic variables. Oxygen consumption rate increases with body length (Small, 1967), pleopod beat rate (Swadling et al., 2005), temperature (Small and Hebard, 1967; Torres and Childress, 1983), swimming speed (Torres and Childress, 1983), and species (Small and Hebard, 1967). The weight of *E. superba* is 60 times greater than the weight of *E. pacifica* (Kils, 1983), which suggests that *E. superba* expend more energy than *E. pacifica* to maintain their position in the ocean. For the pleopod beat rate measured in this study, the respiration of *E. superba* is expected to be around 4 mg O_2 g^{-1} h^{-1} (Swadling et al. 2005). For a mean swimming speed of 2.5 cm s^{-1} at 12ºC, the oxygen consumption rate of *E. pacifica* is 3.2 mg O_2 g^{-1} h^{-1}(Torres and Childress, 1983). Given that the dry weight of a typical *E. pacifica* (7 mg) (Torres and Childress, 1983) is smaller than the dry weight of a typical *E. superba* (50 mg) (Swadling et al. 2005), the overall energy expenditure from oxygen consumption studies is similar to the energy expenditure measured from the fluid environment perspective (i.e., roughly 10 times greater for *E. superba*). Thus, we conclude that propulsion costs are significantly higher for *E. superba* than *E. pacifica.*

Individuals within a school are thought to expend less energy than solitary organisms due to a hydrodynamic benefit (Weihs, 1973). Studies on mysids have shown reduced oxygen uptake by large aggregations (Ritz, 2000), but similar studies on *E. superba* did not find a reduction in oxygen uptake (Swadling et al., 2005). Grouped *E. superba* in this study swam with a lower pleopod beat rate, which is associated with a

decreased respiration rate (Swadling et al., 2005). However, in the current study the energy dissipated in the flow field was not significantly different between solitary *E. superba* and individuals in a group. Because the variation in the dissipation rate calculation was high in the grouped krill, it may be that the calculation of energy dissipated in the flow field does not have sufficient resolution to be an accurate measure of energy expenditure. Based on these measurements and calculations, the energy savings of grouping appear to be subtle, although the behavior may confer other benefits such as refuge from predation and increased ability to find a mate.

5.5.4 Hydrodynamic cue

Hydromechanical cues are suspected to be important for individuals to maintain positions within schools of krill (Hamner, 1984; Wiese and Ebina, 1995). To sense these hydromechanical cues, krill have multiple antennules that are oriented to sense flow in the vertical and horizontal directions. The antennules are lined with hair-type sensilla of a length of 50 μm that sense high frequency (>40 Hz) flow perturbations (Patria and Wiese, 2004). These small sensilla may act similar to copepod setae in response to hydrodynamic cues. Velocity gradients, represented in this study as the maximum deformation rate, have been shown to provide a hydrodynamic sensory cue to copepods via the deflection of setae (Fields and Yen, 1997a, Kiørboe et al., 1999, Fields et al., 2002). In addition to the sensilla, the proprioreceptor at the base of the antennule has been hypothesized to be sensitive to fluid perturbations at 5 – 40 hertz, which roughly matches the frequency of flow perturbations generated by krill (Patria and Wiese, 2004). The proprioreceptor is activated by water velocities along the length of the antennae (half

of the body length of a krill) that are large enough to produce movement of the hinge. For the proprioreceptor, regions of high fluid velocity rather than fluid deformation may act as hydrodynamic cues since a uniform velocity may generate the same deflection of the antennae as a flow perturbation with velocity gradients. Therefore, to identify potential cues in the flow, both the velocity field and maximum deformation rate field were extracted in this study to identify spatial regions with potential hydrodynamic cues.

The sensory cue between krill is suspected to be the high velocity core of the downward directed flow disturbance, where the largest velocities occur (Yen et al., 2003), or the edges of the flow disturbance, where the krill can avoid areas of high velocity (Wiese, 1996; Wiese and Ebina, 1995). In this study, the velocity and deformation rate cue of *E. superba* flow disturbances were persistent at a longer distance (three body lengths vs. one body length) and at a shallower angle (15º vs. 60º from horizontal) than *E. pacifica* flow disturbances. Since *E. pacifica* swim more vertically, they generate a downward directed flow disturbance. Thus, an individual *E. pacifica* krill would need to be located under a neighboring krill to sense the hydrodynamic cue and would potentially experience a significant downward force from the flow field. In contrast, *E. superba* individuals within schools could be spaced farther apart and sample the more horizontally-aligned flow field without experiencing the negative consequences of a high downward-directed velocity. In addition, the greater spatial extent of the hydrodynamic cue in the flow field of *E. superba* suggests that individuals can be spaced farther apart in schools. Individuals would experience less of the negative consequences of schooling such as decreased oxygen supply and increased parasitism as the individuals have less direct contact with each other. As one caveat, since these studies were

performed under still tank conditions, we expect that the cues identified in this study are stronger than the cues present in the natural environment. Further, the data collected for grouped *E. superba* indicate that neighboring flow disturbances interact to produce flow perturbations above background levels at all angles and distances within the groups. Hence, robust hydrodynamic cue may be only available at short distances in the ocean.

5.5.5 Comparison to schooling behavior of *E. superba*

To assess the ability of krill to communicate hydrodynamically, it is important to compare the flow field cues to actual krill arrangements within a school. In situ measurements of *E. pacifica* swarms found that vertical migration was not synchronous (de Robertis et al., 2003) and only one study found a portion of an *E. pacifica* surface swarm with krill in a uniform orientation (Hanamura et al., 1984). It is assumed, therefore, that *E. pacifica* is not a obligate schooling species, and data are not available on the internal arrangement of schools for this species. In contrast, *E. superba* have been reported to school in aquarium during the day (O'Brien, 1989; Strand and Hamner, 1990; Kawaguchi et al., in press) and in the natural environment during the day and night (Hamner et al., 1983). The length of a school is reported to be up to 100 m, but the schools tend to be narrow in one dimension such that an individual is only a few meters from clear water (Hamner et al., 1983; Hamner, 1984). Observations on the density of krill within a school range from 100 to 100,000 krill per cubic meter (Mauchline, 1980), but 60,000 krill per cubic meter is a fairly typical density (Hamner, 1984). The nearest neighbor distances from laboratory studies of schooling krill range from 0.4 body lengths to 3 body lengths (O'Brien, 1989; Kawaguchi et al., in press). Since the hydrodynamic

perturbation of *E. superba* is present at a distance of less than 3 body lengths, the potential cue is within the range of schooling individuals.

Individuals positioned to the side of *E. superba* have a smaller nearest neighbor distance than individuals in front of or behind the krill (O'Brien, 1989). Also, *E. superba* prefer to swim at the same elevation as their neighbors at a nearest neighbor elevation of 0 degrees rather than the optimal 15 degree orientation to sense a velocity or deformation rate cue. The optimal angle of 15 degrees was extracted from the solitary *E. superba* data, and the perturbation cue for the coordinated group occurred at 0 degrees as well, which better coincides with the spatial orientation data. Based on these data, *E. superba* appear to avoid the flow fields of neighboring krill because the krill are oriented in the positions associated with minimal flow disturbance.

The small, coordinated groups in this study consisted of approximately five krill, whereas natural krill schools consist of more than hundreds, usually with densities of tens of thousands of individuals per liter. To more completely address the questions of the cost of propulsion and sensory field around schooling krill, further studies are necessary with simultaneous measurements of schooling krill behavior and the flow fields generated by the krill.

CHAPTER 6

SUMMARY AND CONCLUSIONS

In this study, the flow fields generated by copepods and krill were collected with an infrared Particle Image Velocimetry (PIV) system. The study consisted of three main parts: (1) the flow fields of tethered and free-swimming *Euchaeta antarctica* copepodids were quantified, (2) the flow fields generated by two additional species of *Euchaeta* were compared to elucidate the effect of size and viscosity on the hydromechanical cues associated with copepod propulsion, and (3) the flow fields of schooling and non-schooling krill species were compared to determine if the hydromechanical cue and the energetic costs of propulsion differed between the species. The results of each separate study are described in the summary section of this chapter. The conclusion section of this chapter describes the overall conclusions from all of the studies. Finally, unique contributions of this research and future directions complete this chapter.

6.1 Summary

6.1.1 The effect of tethering on copepodid flow fields

In previous studies, copepods were often tethered during the collection of flow field data with PIV (and other approaches) to reduce the data acquisition time. The tether exerts an unbalanced force on the fluid, and the resulting flow field is similar to the analytical solution of flow induced by a point force in an unbounded fluid volume. The flow fields quantified from tethered copepods are induced by the movement of the

swimming appendages and the point force instead of the copepod alone. Therefore, the data collected on tethered copepods placed in a uniform flow with velocity equal to the copepod swimming speed (presuming the force on the tether is not exactly zero) and tethered copepods in quiescent flow are both not representative of the flow fields generated by free-swimming copepods due to the unbalanced force. The tethered copepodids in this study produced an asymmetrical velocity field (upstream to downstream asymmetry and dorsal to ventral asymmetry) with streamlines of increased curvature (i.e., less parallel to the copepodid body). The hydromechanical cue, which was estimated by the spatial extent of the shear strain rate field, was artificially enlarged by the presence of the tether. Due to the enlarged strain rate fields, the cost of propulsion was overestimated for *E. antarctica* when using tethered flow fields. Hence, ecological predictions of the conspicuousness of the copepod in predator-prey interactions are inaccurate for tethered copepods and these conclusions should be drawn from free-swimming specimens only.

6.1.2 Hydrodynamic disturbances of temperate and subtropical *Euchaeta* species

Euchaeta copepods are globally distributed and inhabit sea water of varying temperature and viscosity. An increase in copepod prosome length is associated with the increase in viscosity between subtropical and polar environments. The resulting Reynolds numbers for cruising and escaping *Euchaeta elongata* (temperate species) and *Euchaeta rimana* (subtropical species) are similar in this study. Consequently, the flow fields of the two species were similar in terms of maximum fluid velocity, peak value of maximum deformation rate, and the spatial extent of the hydromechanical cue during

cruising behavior. The spatial extent of the hydromechanical cues detectable to *Euchaeta* predators and prey were not significantly different between the species when dimensionally quantified. In contrast, the spatial extent normalized by the copepod prosome area was significantly different during cruise behavior. In this case, the area of the cue to prey for the cruising *E. rimana* is equivalent to eighteen body areas, whereas the area of the *E. elongata* cue to prey is eight body areas.

To provide more insight to the effects of size and viscosity on objects moving in a fluid environment, the fluid disturbance generated by moving spheroids with the same dimensions as *E. rimana* (l = 2 mm), *E. elongata* (l = 4 mm), and *E. antarctica* (l = 7 mm) was examined via numerical simulation. The numerical simulation is a greatly simplified model of copepod-induced flow that ignores the details of appendage propulsion. Viscosity had minimal effect on the spatial extent of the spheroid flow fields compared to the effect of the spheroid size. In the simulations of translating spheroids, larger spheroids in the same flow regime as smaller spheroids (i.e., same Reynolds number) produced larger hydrodynamic disturbances. Thus, the larger copepod species (*E. elongata*) is expected to make larger hydromechanical cues during cruising than the smaller species (*E. rimana*) despite the similarity in Reynolds number. Cruising flow fields were similar in spatial extent suggesting a complex interaction of fluid viscosity, organism size, swimming speed, and behavior.

Escape behavior was associated with an increase in propulsion cost compared to cruising copepods. Further, the estimates of propulsive costs during escapes for *E. elongata* are significantly larger than that for *E. rimana*

6.1.3 The hydrodynamic disturbances of two species of krill

Obligate schooling behavior occurs in the largest euphausiid species, *Euphausia superba,* but is not consistently observed in the smaller species, *Euphausia pacifica*. To assess schooling ability, the differences in hydromechanical cue availability and propulsion ability were examined between the two species and coordinated groups of *E. superba.* The swimming behavior of *E. superba* included faster swimming speed, greater Reynolds number, shallower body orientation, and lower pleopod beat rate compared to *E. pacifica*. Individual krill within a coordinated group swam with a decreased pleopod beating rate and steeper body orientation. The use of hydromechanic cues is more likely in *E. superba* than *E. pacifica* because the hydrodynamic disturbances of *E. superba* are larger in horizontal extent and contain a velocity fluctuation at the same frequency as the pleopod beat rate. Hydromechanical cue extractions from the krill flow fields show that *E. superba* cues may be detectable at a distance of more than 2 body lengths, which is consistent with nearest neighbor distances of schooling krill (O'Brien, 1989), while *E. pacifica* cues may be detectable at only less than one body length.

The cues extracted from the coordinated groups show that the flow disturbance is complicated by the interaction of multiple krill flow fields, hence successful transmission of hydrodynamic cues should occur at short distances. The coordinated group behavior has previously been suspected as providing an energetic benefit to krill (Swadling et al., 2005). In this study, krill individuals within a coordinated group did not experience reduced energetic expenditures compared to solitary individuals when measured via the total energy dissipated in the flow disturbance.

6.2 Conclusions

6.2.1 Hydromechanical cues

Copepods have limited visual abilities and rely on hydromechanical cues to sense predators, prey, mates, and oceanic fluid disturbances. Predation of copepods can be cannibalistic or by other species of copepods. Thus, the sensory abilities of predator and prey are similar, and copepods greatly benefit from reducing the spatial extent of their hydrodynamic signature. For *E. elongata*, the extent of the flow disturbance was smaller for the more common cruising behavior than the rarer escape behavior resulting in reduced hydrodynamic conspicuousness (Figure 6.1). Alternatively, krill are significantly larger than copepods and are predated on by large mammals with less sensitive rheotactic sensors. Therefore, reducing the hydromechanical cue, presumably, would not improve species success. The hydromechanical cues of the krill, particularly *E. superba,* extend much further behind the organism than the flow disturbances of copepods. The existence of a large hydrodynamic trail suggests that hydromechanical cues in krill is encouraged to sense conspecifics and maintain schools. In conclusion, the ecological niche of zooplankton determines the necessity and type of hydromechanical cues.

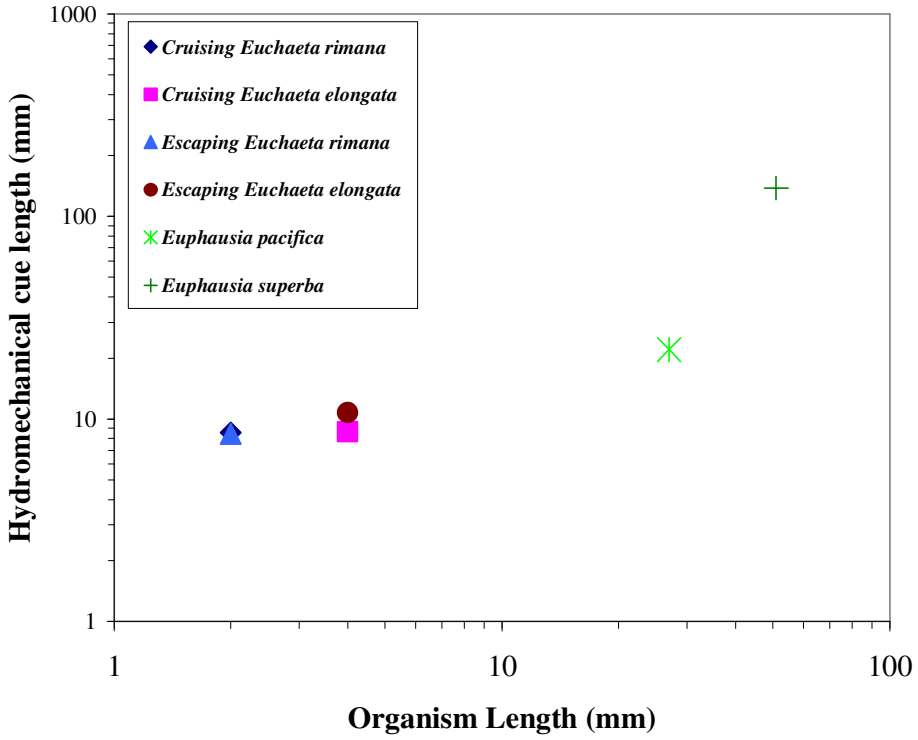

Figure 6.1 The characteristic length of the flow fields for copepods and krill plotted against organism size on log-scaled axes. The lengths were designated as the square root of the area of the hydromechanical cue to prey for the copepod species and the horizontal extent of the flow disturbance for the krill speces.

6.2.2 Cost of propulsion

To provide insight about the cost of propulsion among different types of zooplankton, the energetic cost of propulsion is plotted against Reynolds number in Figure 6.2. Cruising copepods that operate in a Reynolds number of roughly 10 used on the order of 10^{-8} Watts for propulsion. When the Reynolds number increased to roughly 100 for escaping copepods or *E. pacifica*, the subsequent cost of propulsion increased to the order of 10^{-7} Watts. For Reynolds numbers of 1000, the cost of propulsion was around 10^{-6} Watts. Thus, the consequences of increased size or increased swimming speed are a larger cost of propulsion.

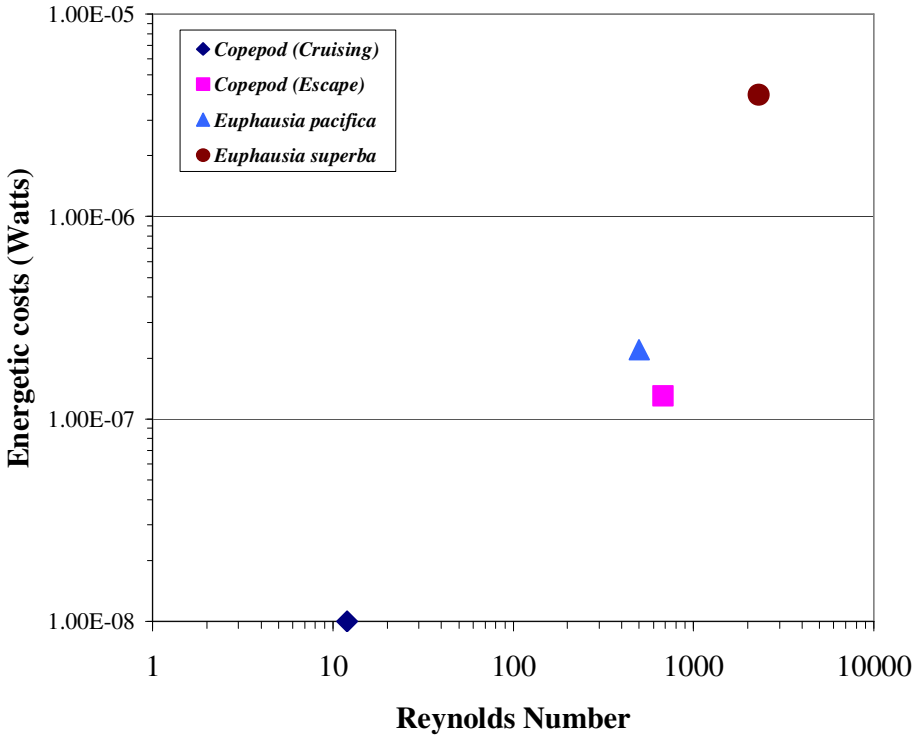

Figure 6.2 The energetic costs of propulsion for copepods and krill plotted against Reynolds number on log-scaled axes.

Since the swimming behavior was different between organisms with similar energetic costs and Reynolds number, the propulsion method is not indicated as the significant factor in the cost of propulsion (at least by the measure of energy dissipated in the flow disturbance). Ecologically, this conclusion is logical because an optimal swimming behavior that reduced energetic costs by an order of magnitude for a particular Reynolds number would be more successful in the competitive marine environment. If energetic costs were reduced, then the organism would require less energetic input. Further comparisons of propulsion costs would elucidate how the cost of propulsion may change in varying ecological conditions.

6.3 Unique contributions of the research

Unique contributions to the field of fluid mechanics of zooplankton propulsion and sensory ecology include the following:

- The quantification of the flow fields of multiple species of *Euchaeta* with high resolution PIV.
- The collection of the first untethered velocity field of an escaping copepod.
- A theoretical analysis that clearly explains how tethering alters the measurement of copepod-generated flow fields.
- A computational analysis of the effect of viscosity on the flow fields of prolate spheroids scaled to represent cruising copepods.
- The quantification of the flow fields of two species of free-swimming krill.
- The collection of flow fields around coordinated groups of krill, which appears to be the first PIV study of a group of zooplankton.

The contributions to the field of biological and physical interactions in marine ecology are listed below:

- The calculation of zooplankton flow field statistics with replicate flow field data to address ecological questions.
- The quantification of the hydromechanical cues of interest to the predators, prey, and conspecifics for three species of copepod and two species of krill.

- The cost of propulsion was estimated for zooplankton at a range of Reynolds numbers.

6.4 Future Directions

The results of this research effort provide the groundwork to answer several questions in the interdisciplinary research area of fluid mechanics and ecology. The future directions motivated by the current research are outlined in the following sections.

6.4.1 Three-dimensional flow fields

This research effort was limited to the collection of two-dimensional flow fields with a planar PIV system. To construct three-dimensional representations of the flow, flow fields were obtained for several individuals at different body orientations. Zooplankton perform specific behaviors that cause the data collection to be challenging and different for each species. For instance, the copepods swam both vertically and horizontally such that flow fields could be collected in the dorso-ventral and side view without realignment of the PIV system. Contrarily, the krill moved forward in the horizontal direction such that only side views were easily collected with the system. Due to field site limitations, mounting of the cameras below or above the krill to collect multiple dorsal-ventral views was nearly impossible. In addition, zooplankton must swim straight along the laser sheet (rather than at an angle) to produce a usable flow field. For this reason, more replicates were collected than were needed for the statistical analysis at a considerable data storage cost because passes of poor quality were subsequently discarded.

Recent advances in technology have led to the development of three-dimensional PIV systems that would allow complete assessment of the flow fields without a considerable effort to accommodate varying zooplankton behavior. In addition, many research questions require an assessment of the fluid volume (e.g., cue extent, feeding currents, and propulsion estimates) rather than a planar slice of the flow field. For better completeness and accuracy, future data collection efforts require the quantification of the fluid disturbances produced by zooplankton in a three-dimensional volume.

6.4.2 Accurate assessment of the hydromechanical cue

The estimation of a hydromechanical cue requires both an accurate quantification of the flow field of the organism producing the cue and the location of organism sensing the cue. Previous studies on the hydromechanical cue generated by copepods determined the behavioral threshold value of the cue by stimulating a response to the cue with artificial stimuli (e.g., Fields and Yen, 1996, 1997; Kiørboe et al., 1999; Fields and Yen, 2002; Titelman, 2001; Titelman and Kiørboe, 2003). The behavioral response of an organism to an artificial flow condition does not take into account response plasticity to different species, ambient conditions, and other factors, and is less desirable. The typical flow fields generated by the zooplankton in this study are now accurately quantified such that behavioral experiments can be conducted on *Euchaeta* predators, *Euchaeta* prey, and schooling *E. superba* to determine the threshold fluid disturbance.

The simultaneous measurement of flow fields with various organism responses is preferable. However, the PIV system collects high resolution images, which require a significant amount of computer storage and management. Often, the response of interest

(e.g., capture, mating) is a rare occurrence and requires the collection of data over long time periods. Thus, the reaction distances of response of organisms to a biologically-generated flow field may need to be collected separately from the flow fields and combined in a way similar to the studies on artificial flow stimuli. As stated, the first step towards accurately assessing the hydromechanical cues may be a decoupled research effort; however, the future research direction should be the simultaneously collection of flow field and behavioral data.

6.4.3 Propulsion estimates

As stated above, a three-dimensional measurement of the flow fields would provide better estimates of the cost of propulsion. In addition, the temporal aspects of the measurements need to be improved. For example, the copepod escape flow field data were collected at 25 Hz, whereas a frequency of 1,000 Hz is needed to capture the movement of the antennule and swimming legs during an escape (personal observation). As a result, the "instantaneous" flow field data represents a time-averaged flow field from the perspective of high speed behavior, such as an escape. Improved temporal resolution of the acquisition would be positive step forward.

In addition, many replicate flow fields are needed to calculate an estimate of the cost of propulsion for a given species and swimming method. When numerical models are employed to model the flow field produced by an organism, copepod, fluid, and behavior properties can be modified without additional experimentation. Jiang et al. (2002a,b) created several numerical models of copepod swimming, but the models were not directly validated to experimental results and were performed at too low of a

resolution to capture all of the pertinent propulsion data. The future direction of propulsion studies should be the combined approach of experimental fluid mechanics data with complementary numerical simulations. The experimental data will provide verification of the modeled flow field and the numerical simulation will be used to create varied fluid and organism conditions.

APPENDIX A

KRILL AGGREGATION BEHAVIOR AS A MECHANISM FOR MIXING IN THE OCEAN

A.1 Summary

The generation of significant biomixing, the mixing of the ocean by biological organisms, depends on the structure of the flow fields produced by marine organisms. Flow induced by solitary krill is shown here to be restricted to the length scale of the krill body, and the corresponding mixing efficiency is small. However, when krill form coordinated groups, the flow pattern occurring over the length scale of the aggregation may provide sufficient vertical transport to overturn density-stratified layers. Aggregations of krill have vertical extents that are significantly (5 – 15 times) larger than the typical buoyancy length scale, with a potential contribution of 20% of the generated kinetic energy to ocean mixing.

A.2 Introduction

The contribution of the swimming motion of marine organisms to diapycnal mixing, known as biomixing, is currently under debate (Kunze et al., 2007; Visser, 2007). The controversy centers around how efficiently biologically-generated turbulence vertically mixes the stratified ocean. In situ measurements (Kunze et al., 2006) and theoretical calculations (Huntley and Zhou, 2004) of biologically-generated turbulence estimate that the turbulent energy dissipation rates generated by groups of krill are on the order of 10^{-4} W kg^{-1} to 10^{-5} W kg^{-1}, which are four orders of magnitude greater than the

background turbulence level in density-stratified water. From these studies, it appears that biologically-generated turbulence is a significant contribution to ocean mixing.

However, Visser (2007) contends that at most only 1% of the kinetic energy produced by schools of krill is converted to ocean mixing because krill generate turbulence at a small-scale (approximately the length scale of one krill, i.e., 20-65 mm). To overturn the stratification, turbulent eddies must be larger than the buoyancy length scale (Ozmidov scale), and the typical buoyancy length scales for the deep ocean and surface ocean are 1 to 10 meters, respectively (Visser 2007). In contrast to this theoretical argument, Kunze et al. (2007) observed biologically-generated turbulence at length scales of 1 to 10 meters, which are larger than the length scales of a single krill.

To date, only theoretical and large-scale field studies have been performed to determine whether biomixing is a significant contributor to the mixing of the ocean. In the current study, we measure the flow fields generated by solitary krill of two species, *Euphausia pacifica* (body length = 20 mm) and *Euphausia superba* (body length = 65 mm), and a coordinated group of *Euphausia superba* with Particle Image Velocimetry (PIV). To our knowledge, this is the first study that quantifies the small-scale fluid motion around solitary and aggregated krill to address the question of mixing, although we should note that Goldthwait et al. (2004) used flow field measurements around solitary krill to address the disruption of marine snow aggregates, which affects the rate of carbon cycling in the ocean. We calculate the instantaneous energy dissipation rate fields and the length scales of the flow perturbation for solitary and groups of krill to address mixing efficiency and determine whether krill are capable of mixing the ocean.

A.3 Methods

Euphausia pacifica specimens were collected in July 2007 from a location 25 miles off the coast of Newport, Oregon and kept in a temperature controlled room at 10°C. *Euphausia superba* were collected from various locations south of the 60° S latitude line and individuals were kept in Kingston, Tasmania at the Australian Antarctic Division in a temperature controlled aquarium at 0.5°C. Free-swimming passes of solitary specimens of both species were captured in a clear, glass cubic tank (volume = 3375 cm^3) of still seawater. *E. superba* group data were collected in a circular 100 liter tank of still seawater while a group of approximately 100 krill were swimming in a uniform direction (krill density = 1000 krill per cubic meter). The krill density in the study is conservative compared to in situ observations of *E. superba* aggregations (Watkins, 2000). The velocity fields were collected at a rate of 25 hertz using a planar, infrared Particle Image Velocimetry (PIV) system consisting primarily of an Oxford pulsed, infrared laser (model HSI-500) and a VDS Vosskühler CMC-1300 Complementary Metal Oxide Semiconductor (CMOS) digital camera (1280 × 1024 pixels). An infrared laser was used in this study because the wavelength of the laser (808 nm) is outside of the visible range of krill perception, hence krill behavior was unaffected by the laser. A Pulnix camera was positioned perpendicular to the CMOS camera to monitor the location of the krill within the tank and ensure that data were only collected while krill were actively swimming within the plane of the laser sheet. Two dimensional velocity vector fields were obtained by measuring the displacement of very small titanium dioxide particles (< 5 μm) by fluid motion over a known time period (i.e., the time period between laser pulses). The velocity field data from the PIV analysis was

used to calculate the energy dissipation rate as described in Catton et al. (2007). The energy dissipation rate represents the rate at which kinetic energy is dissipated by viscosity due to the presence of velocity gradients.

A.4 Results

The maximum values of the energy dissipation rate in the flow disturbance of solitary *Euphausia pacifica* and *Euphausia superba* krill were 1.4×10^{-3} W kg^{-1} (mean value, $n = 8$, range 2.0×10^{-4} W kg^{-1} to 3.4×10^{-3} W kg^{-1}) and 4.8×10^{-3} W kg^{-1} (mean value, $n = 6$, range 1.7×10^{-3} W kg^{-1} to 1.2×10^{-2} W kg^{-1}), respectively (Figure A.1). The mean value for the maximum energy dissipation rate was not significantly different ($p > 0.05$) between the two species despite the fact that *E. superba* individuals were typically three times the length of *E. pacifica* individuals. Furthermore, coordinated behavior among the *Euphausia superba* (Figure A.2) did not significantly increase the maximum energy dissipation rate (mean value = 4×10^{-3} W kg^{-1}, $n = 3$, range 3×10^{-3} W kg^{-1} to 6×10^{-3} W kg^{-1}). The flow fields are not turbulent because the Reynolds number of the biologically-induced jet is on the order of one hundred and, hence, in the transitional regime. The flow is, however, unsteady due to appendage motion and the movement of the organism. From a large scale perspective, the flow field induced by krill aggregations may appear similar to turbulence because the flow field is unsteady and possesses a wide range of scales of motion. As discussed further below, the characteristic length scale of the flow field is on the order of the depth and width of the krill aggregation rather than the length of an individual krill.

Although the field measurements were collected with different approaches, it is appropriate to compare our estimates of energy dissipation rate within the krill aggregations to the estimates made via the in situ data. The energy dissipation rate estimates in this study were calculated with the spatial gradients of the instantaneous velocity field calculated by finite difference for data separated typically by a distance of 2 mm. The turbulent energy dissipation rate measured in situ was estimated by fitting the shear spectra produced by microscale shear, temperature and conductivity probes with 1 cm resolution to a model turbulence spectrum (Kunze et al., 2006). The turbulent kinetic energy dissipation rate measured in the field, therefore, corresponds to the time-averaged value of the viscous dissipation by small scale turbulent fluctuations. The dissipation rate calculated in the current study corresponds to the energy dissipated by viscosity acting on the gradients in the instantaneous velocity fields. Hence, these quantities describe the same physical phenomenon, but time-averaging for the turbulence perspective of the in situ data has the effect of masking brief (and local) high values of dissipation rate that the current measurements capture. As a consequence, the maximum energy dissipation rates measured in the current study were two orders of magnitude larger than the in situ measurements. However, comparison of the in situ data to the spatially and temporally averaged value for the velocity fields measured in this study should be of the same order of magnitude. The spatially-averaged dissipation rate averaged over the time record is 1×10^{-5} W kg^{-1}, which agrees well with the in situ data (Kunze et al., 2006; Huntley and Zhou, 2004).

A.5 Discussion

The flow generated by swimming krill contributes to high levels of local transport within the schools, but the effect of the small-scale flow patterns on global ocean mixing is unknown. The buoyancy length scale, which is a function of the energy dissipation rate (ε) and the buoyancy frequency (N), represents the minimum size of a turbulent eddy that can overturn in a density stratified layer:

$$l_b = \left(\frac{\varepsilon}{N^3} \right)^{\frac{1}{2}} \tag{A.1}$$

The buoyancy length scale (l_b) was derived by equating the inertial forces in turbulence to the buoyancy force under the assumptions of isotropic turbulent flow and a linear density gradient (Gibson, 1980). The fluid motion generated by solitary krill is not isotropic turbulent flow but rather an inclined jet that extends in the vertical direction roughly 26 ± 11 mm (n = 7) for *E. pacifica* and 21 ± 4 mm (n = 6) for *E. superba* based on the location where the flow decreases to less than 10% of the maximum jet velocity (Figure A.2). The flow pattern induced by solitary and groups of krill consists of structured, coordinated fluid motion, in contrast to isotropic turbulence in which the fluid motion is randomly directed. The spatial extent of the flow patterns generated by solitary krill is well approximated as the vertical extent of the jet, which is roughly the same scale as the krill length (20 – 65 mm) as assumed by Visser (2007) (Figure A.1). Thus, we conclude that solitary swimming krill do not have the ability to created flow patterns that overturn in stratified waters and mix the ocean because the mixing efficiency is small.

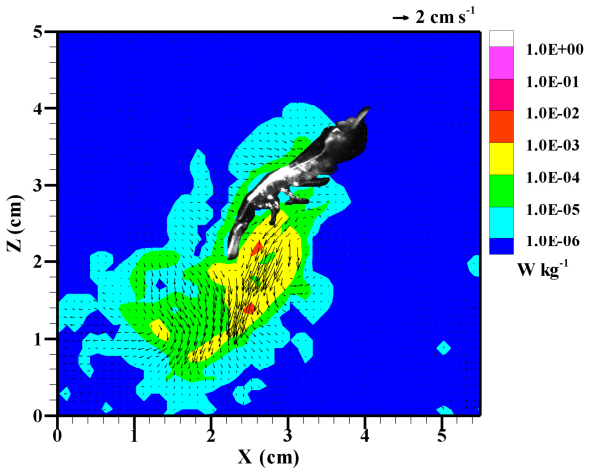

A

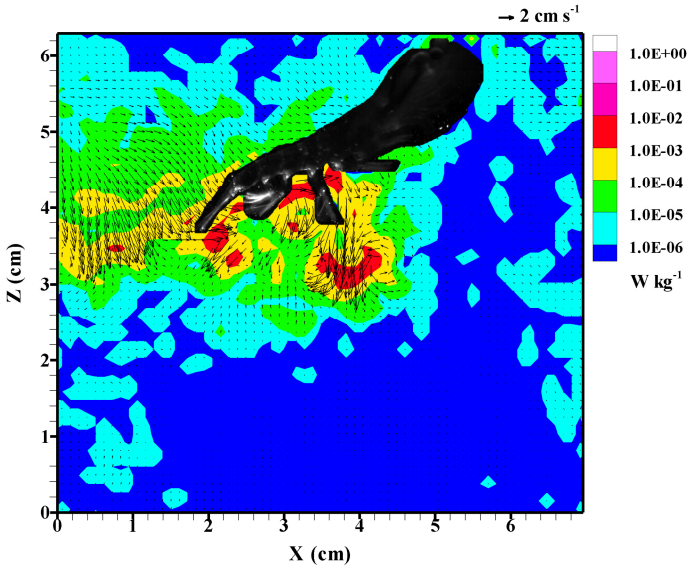

B

Figure A.1 Instantaneous flow and energy dissipation rate fields produced by a solitary free-swimming (A) *Euphausia pacifica*, and (B) *Euphausia superba.* The vectors represent the magnitude and direction of the fluid velocity, while the contour level indicates dissipation rate.

The conclusion is different when considering krill aggregations. In order to assess the vertical transport of fluid within the krill aggregation we calculated the vertical displacement of a small fluid region (illustrated by a black box in Figure A.2). The displacement of the small fluid region was calculated based on the sequence of measured velocity fields (i.e., the region was displaced by a distance equal to the local velocity times the time delay between fields then the calculation was repeated at the new location in the subsequent velocity field). Over the measured 1.8 s sequence, the average vertical distance was calculated to be 25.3 mm ± 4.2 mm and the vertical transport continues beyond our measurement region. The average vertical distance of the box displacement in replicate data sets was found to be 27 mm (n = 2). In addition, in each of the group data sets the vertical transport of the box continued past the measurement area. Hence, a larger field of view and a longer observation period would reveal significantly greater transport distance in the vertical direction due to the flow induced by neighboring krill. Hence, our measurements and calculations suggest that fluid is transported over the vertical extent of the aggregation, rather than the scale of an individual, due to the combined flow induced by neighboring krill. Vertical advection of fluid was facilitated by the passing of water from the flow disturbance of one krill into the flow disturbance of the next krill as seen in the sequences in Figure A.2. Consequently, in a stratified layer the krill-induced flow, whose spatial extent is the depth of the aggregation, may transport less dense water into denser water, which explains the unstable density regions seen in the field (Kunze et al., 2007). In a related study, Ritz (2000) qualitatively observed in the laboratory a powerful downdraft beneath a swarm of mysids, another aggregating organism, and an updraft equal to the height of the swarm as a result of the displacement

of the water. Hence, the largest flow perturbations created by krill aggregations is on the order of the depth of the krill aggregation, which range from 25 to 150 meters for *E. superba* (Zhou and Dorland, 2004) and 25 meters for *E. pacifica* (Kunze et al., 2006), rather than the length scale of an individual krill. These length scales are significantly larger than the typical buoyancy length scales near the surface and in the deep ocean. Employing this estimate of the vertical length scale of the flow pattern induced by krill in the mixing efficiency calculation of Visser (2007), the mixing efficiency estimate is closer to 20%. Using the 400 GW estimate given by Dewar et al. (2006) for the mechanical energy of zooplankton migration, we calculate that 80 GW is provided by zooplankton migration to the ocean for mixing. Munk and Wunsch (1998) estimate that the maintenance of abyssal stratification requires 2.1 TW with distributed pelagic turbulence and localized turbulent patches inputting 200 and 700 GW, respectively. Hence, zooplankton migration provides an energy input to ocean mixing, but the contribution is less than other sources of turbulence.

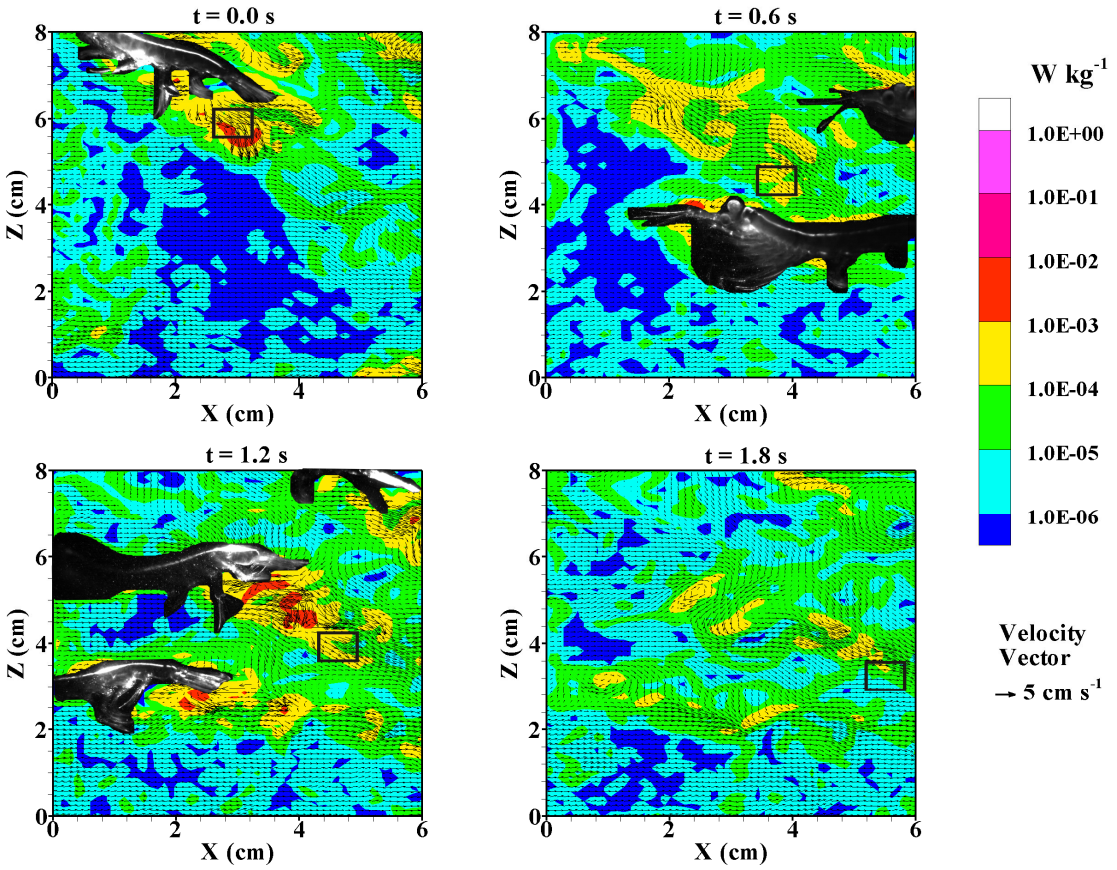

Figure A.2 A sequence of the flow and instantaneous energy dissipation rate fields produced by a group of free-swimming *Euphausia superba.* In this sequence, a group of four krill are observed passing through the measurement region.

We identified a mechanism that produces biologically-generated flow patterns of length scales much larger than individual krill, but it should be noted that the group behavior of krill ultimately determines the existence of the flow patterns and vertical transport. Kunze et al. (2006) noted that krill-induced turbulence was not present on a subsequent sampling day when larger euphausiids did not vertically migrate, which suggests that only groups of large euphausiids are capable of generating biomixing. In addition, de Robertis (2002) studied the in situ behavior of *E. pacifica* at the same location and found that *E. pacifica* were not swimming in aggregations but rather as solitary individuals. In contrast, *E. superba* is an obligate schooling species (Hamner and Hamner, 2000) that vertically migrates several times a day and as a result is the species that is more likely to contribute large amounts of mixing. Also, krill schools are accompanied by large numbers of predators, which may contribute to the overall mixing associated with krill aggregations. In conclusion, we showed that it is necessary for krill to be swimming in coordinated aggregations in order to pass water vertically between neighbors and create large-scale flow patterns and vertical transport.

REFERENCES

Adrian, R. J. (1991). Particle-imaging techniques for experimental fluid mechanics. Ann. Rev. Fluid Mech. 23: 261-304.

Alcaraz, M., Paffenhöfer, G. A. and Strickler, J. R. (1980). Catching the algae: A first account of visual observations on the filter feeding calanoids. In Evolution and Ecology of Zooplankton communities. Special Symposium American Society of Limnology and Oceanography, 57th edition, 241-248. Hanover: University Press of New England.

Alcaraz, M. and Strickler, J. R. (1988). Locomotion in copepods: pattern of movements and energetcis of *Cyclops*. Hydrobiologia 167/168: 409-414.

Atkinson, D. and Sibly, R. M. (1997). Why are organisms usually bigger in colder environments. Making sense of a life history puzzle. Trends Ecol. Evol. 12: 235-239.

Baird, T. A., Ryer, C. H. and Olla, B. L. (1991). Social enhancement of foraging on an ephemeral food source in juvenile walleye pollock, *Theragra chalcogramma*. Environ. Biol. Fish. 31: 307-311.

Berner, A. (1962). Feeding and respiration in the copepod *Temora longicornis*. J. Mar. Biol. Ass. U.K. 42: 625-640.

Bocher, P., Cherel, Y., Alonzo, F., Razouls, S., Labat, J. P., Mayzaud, P. and Jouventin, P. (2002). Importance of the large copepod *Paraeuchaeta antarctica* (Giesbrecht, 1902) in coastal waters and the diet of seabirds at Kerguelen, Southern Ocean. J. Plank. Res. 24: 1317-1333.

Bollens, S. M., Frost, B. W. and Lin, T. S. (1992). Recruitment, growth, and diel vertical migration of *Euphausia pacifica* in a temperate fjord. Mar. Biol. 114: 219-228.

Braga, E., Zardoya, R., Meyer, A. and Yen, J. (1999). Mitochondrial and nuclear rRNA based copepod phylogeny with emphasis on *Euchaetidae* (*Calanoida*). Mar. Biol. 133: 79-90.

Bundy, M. H. and Paffenhöfer, G. A. (1996). Analysis of flow fields associated with freely swimming calanoid copepods. Mar. Ecol. Prog. Ser. 133: 99-113.

Burdick, D. S, Hartline, D. K. and Lenz, P. H. (2007). Escape strategies in co-occurring calanoid copepods. Limnol. Oceanogr. 52: 2373-2385.

Burgess, J. W. and Shaw, E. (1979). Development and ecology of fish schooling. Oceanus 22: 11-17.

Buskey, E. J. (2000). Role of vision in the aggregative behavior of the planktonic mysid *Mysidium columbiae*. Mar. Biol. 137: 257-265.

Buskey, E. J., Lenz, P. H. and Hartline, D. K. (2002). Escape behavior of planktonic copepods in response to hydrodynamic disturbances: high speed video analysis. Mar. Ecol. Prog. Ser. 235: 135-146.

Catton, K. B., Webster, D. R., Brown, J. and Yen, J. (2007). Quantitative analysis of tethered and free-swimming copepodid flow fields. J. Exp. Biol. 210: 299-310.

Cekunova, V. I. and Rynkova, T. I. (1974). Energy requirements of the Antarctic crustacean *Euphausia superba* Dana. Oceanology 14: 434-440.

Chapelle, G. and Peck, L. S. (1999). Polar gigantism dictated by oxygen availability. Nature 399: 114-115.

Cohen, J. H. and Forward, R. B. Jr. (2002). Spectral sensitivity of vertically migrating marine copepods. Biol. Bull. 203: 307-314.

Coombs, S., Janssen, J. and Webb, J. C. (1988). Diversity of lateral line systems: Evolutionary and functional considerations. In Sensory Biology of Aquatic Animals (eds. J. Atema, R. Fay, A. N. Popper, and W. N. Tavolga), pp. 553-594. Springer Verlag.

Dabiri, J. O. (2005). On the estimation of swimming and flying forces from wake measurements. J. Exp. Biol. 208: 3519-3532.

de Robertis, A. (2002). Small-scale spatial distribution of the euphausiid *Euphausia pacifica* and overlap with planktivorous fishes. J. Plank. Res. 24: 1207-1220.

De Robertis, A., Schell, C. and Jaffe, J. S. (2003). Acoustic observations of the swimming behavior of the euphausiid *Euphausia pacifica* Hansen. J. Mar. Res. 60: 885-898.

Dewar, W. K., Bingham, R. J., Iverson, R. L., Nowacek, D. P., St. Laurent, L. C. and Wiebe, P. H. (2006). Does the marine biosphere mix the ocean? J. Mar. Res. 64: 541-561.

Doall, M. H., Strickler, J. R., Fields, D. M., and Yen, J. (2002). Mapping the free-swimming attack volume of a planktonic copepod *Euchaeta rimana*. Mar. Biol. 140: 871-879.

Drucker, E. G. and Lauder, G. V. (2002). Experimental hydrodynamics of fish locomotion: Functional insights from wake visualization. Integr. Comp. Biol. 42: 243-257.

Ebina, Y. and Miki, T. (1996). Range and biological significance of characteristic water currents produced by the shrimps *Euphausia superba* and *Metapenaeus intermedius*. Zoology 99: 163-174.

Emlet, R. B. (1990). Flow fields around ciliated larvae: Effects of natural and artificial tethers. Mar. Ecol. Prog. Ser. 63: 211-225.

Endo, Y. (1981). Ecological studies on the euphausiids occurring on the Sanriku waters with special reference to their life history and aggregated distribution. Ph.D. Thesis, Tokuhu University, Sendhai.

Endo, Y. (1993). Orientation of Antarctic krill in an aquarium. Nippon Suisan Gakkaishi 59: 465-468.

Epp, R. W. and Lewis, W. M. (1979). Metabolic responses to temperature change in a tropical freshwater copepod (*Mesocyclops brasilianus*) and their adaptive significance. Oecologia 42: 123-138.

Epps, B. P. and Techet, A. H. (2007). Impulse generated during unsteady maneuvering of swimming fish. Exp. Fluids 43: 701-712.

Fields, D. M. and Weissburg, M. J. (2005). Evolutionary and ecological significance of mechanosensor morphology: Copepods as a model system. Mar. Ecol. Prog. Ser. 287: 269-274.

Fields, D. M. and Yen, J. (1993). Outer limits and inner structure: The 3-dimensional flow field of *Pleuromamma xiphias* (Calanoida: Metridinidae). Bull. Mar. Sci. 53: 84-95.

Fields, D. M. and Yen, J. (1996). The escape behavior of *Pleuromamma xiphias* (Calanoida: Metridinidae). Bull. Mar. Sci. 53: 84-95.

Fields, D. M. and Yen, J. (1997a). The escape behavior of marine copepods in response to a quantifiable fluid mechanical disturbance. J. Plank. Res. 19: 1289-1304.

Fields, D. M. and Yen, J. (1997b). Implications of the feeding current structure of *Euchaeta rimana*, a carnivorous pelagic copepod, on the spatial orientation of prey. J. Plank. Res. 19: 79-95.

Fields, D. M. and Yen, J. (2002). Fluid mechanosensory stimulation of behavior from a planktonic marine copepod, *Euchaeta rimana* Bradford. J. Plank. Res. 24: 747-755.

Fields, D. M., Shaeffer, D. S. and Weissburg, M. J. (2002). Mechanical and neural responses from the mechanosensory hairs on the antennule of Gaussia princes. Mar. Ecol. Prog. Ser. 227: 173-186.

Foster, E. G., Ritz, D. A., Osborn, J. E. and Swadling K. M. (2001). Schooling affects the feeding success of Australian salmon (*Arripis trutta*) when preying on mysid swarms (*Paramesopodopsis rufa*). J. Exp. Mar. Biol. Ecol. 261: 93-106.

Fraser, W. R., Pitman, R. L. and Ainley, D. G. (1989). Seabird and fur seal responses to vertically migrating winter krill swarms in Antarctica. Polar Biol. 10: 37-41.

Gallager, S. M. (1988). Visual observations of particle manipulations during feeding in larvae of a bivalve mollusk. Bull. Mar. Sci. 43: 344-365.

Gallager, S. M. (1993). Hydrodynamic disturbances produced by small zooplankton: A case study for the veliger larva of a bivalve mollusk. J. Plank. Res. 15: 1277-1296.

Gibson, C. H. (1980). Fossil temperature, salinity and vorticity turbulence in the ocean. In Marine turbulence (ed. J.C.J. Nihoul), pp. 221-258, Elsevier Scientific Pub. Co.

Goldthwait, S., Yen, J., Brown, J. and Alldredge, A. (2004). Quantification of marine snow fragmentation by swimming euphausiids. Limnol. Oceanogr. 49: 940-952.

Green, S., Visser, A. W., Titelman, J. and Kiørboe, T. (2003). Escape responses of copepod nauplii in the flow field of the blue mussel, *Mytilus eduli*. Mar. Biol. 142: 727-733.

Greene, C. H. and Landry, M. H. (1985). Patterns of prey selection in the cruising calanoid predator *Euchaeta elongata*. Ecology 66: 1408-1416.

Hain, J. H. W., Carter, G. R., Kruas, S. D., Mayo, C. A. and Winn, H. E. (1982). Feeding-behavior of the humpback whale, *Megaptera-Novoaenglei*, in the Northern Atlantic. Fish. Bull. 80: 259-268.

Hamner, W. M. (1984). Aspects of schooling in *Euphausia superba.* J. Crust. Biol. 4: 67-74.

Hamner, W. M. (1995). Predation, cover and convergent evolution in the epipelagic oceans. Mar. Fresh. Behav. Physiol. 26: 71-89.

Hamner, W. M. and Hamner, P. P. (2000). Behavior of Antarctic krill (*Euphausia superba*): Schooling foraging, and antipredatory behavior. Can. J. Fish. Aquat. Sci. 57: 192-202.

Hamner, W. M. and Parrish, J. K. (1997). Is the sum of the parts equal to the whole: The conflict between individuality and group membership. In Animal Groups in Three Dimensions: How Species Aggregate. (eds. J. K. Parrish and W. M. Hamner), pp. 165-173, Cambridge University Press.

Hamner, W. M., Hamner, P. P., Obst, B. S. and Carlton, J. H. (1989). Field observations on the ontogeny of schooling of *Euphausia superba furciliae* and its relationship to ice in Antarctic waters. Limnol. Oceanogr. 34: 451-456.

Hamner, W. M., Hamner, P. P., Strand, S. W. and Gilmer, R. W. (1983). Behavior of Antarctic krill, *Euphausia superba*: Chemoreception, feeding, schooling, and molting. Science 220: 433-435.

Hanamura, Y., Endo, Y. and Taniguchi, A. (1984). Underwater observation on the surface swarm of a Euphausiid, *Euphausia pacifica* in Sendai Bay, Northeastern Japan. La Mer 22: 63-68.

Huntley, M. E. and Zhou, M. (2004). Influence of animals on turbulence in the sea. Mar. Ecol. Prog. Ser. 273: 65-79.

Hwang, J., Turner, J. T., Costello, J. H., Coughlin, D. J. and Strickler, J. R. (1993). A cinematographic comparison of behavior by the calanoid copepod *Centropages hamatus* Lilljeborg: Tethered versus free-swimming animals. J. Exp. Mar. Biol. Ecol. 167: 277-288.

Jaffe, J. S., Ohman, M. D., and de Robertis, A. (1999). Sonar estimates of daytime activity levels of *Euphausia pacifica* in Saanich Inlet. Can. J. Fish. Aqua. Sci. 56: 2000-2010.

Jeong, J. and Hussain, F. (1995). On the identification of a vortex. J. Fluid Mech. 285: 69-94.

Jiang, H., Meneveau, C. and Osborn, T. R. (1999). Numerical study of the feeding current around a copepod. J. Plank. Res. 21: 1391-1421.

Jiang, H., Osborn, T. R. and Meneveau, C. (2002a). The flow field around a freely swimming copepod in steady motion. Part I: Theoretical analysis. J. Plank. Res. 24: 167-189.

Jiang, H., Meneveau, C. and Osborn, T. R. (2002b). The flow field around a freely swimming copepod in steady motion. Part II: Numerical simulation. J. Plank. Res. 24: 191-213.

Johnson, M. L. and Tarling, G. A. (2008). Influence of individual state on swimming capacity and behavior of Antarctic krill *Euphausia superba.* Mar. Ecol. Prog. Ser. 366: 99-110.

Kanda, K., Takagi, K. and Seki. Y. (1982). Movement of the larger swarms of Antarctic krill *Euphausia superba* off Enderby Land during 1976-1977 season. J. Tokyo Univ. Fish. 68: 25-42.

Kerfoot, W. C. (1978). Combat between predatory copepods and their prey-Cyclops, *Epischura*, and *Bosmina*. Limnol. Oceanogr. 23: 1089-1102.

Katija, K. and Dabiri, J. O. (2008). In situ field measurements of aquatic animal fluid interactions using a Self Contained Underwater Velocimetry Apparatus (SCUVA). Limnol. Oceanogr.: Methods 6: 162-171.

Kawaguchi, S., King, R., Meijers, R., Osborn, J. E., Swadling, K. M., Ritz, D. A. and Nicol, S. (in press). An experimental aquarium for observing the schooling behaviour of Antarctic krill (*Euphausia superba*). Deep-Sea Res. II.

Kils, U. (1979a). Performance of Antarctic krill *Euphausia superba,* at different levels of oxygen saturation. Meeresforsch 27: 35-48.

Kils, U. (1979b). Swimming speed and escape capacity of Antarctic krill, *Euphausia superba.* Meeresforsch 27: 264-266.

Kils, U. (1982). The swimming behaviour, swimming performance and energy balance of Antarctic krill, *Euphausia superba.* BIOMASS Scientific Series 3: 1-121.

Kils, U. (1983). Swimming and feeding of Antarctic krill, *Euphasia superba* - some outstanding energetics and dynamics - some unique morphological details. On the biology of krill *Euphausia superba,* Proceedings of the Seminar and Report of Krill Ecology Group.

Kiørboe, T. and Visser, A. W. (1999). Predator and prey perception in copepods due to hydromechanical cues. Mar. Ecol. Prog. Ser. 179: 81-95.

Kiørboe, T., Saiz, E. and Visser, A. W. (1999). Hydrodynamic signal perception in the copepod *Acartia tonsa*. Mar. Ecol. Prog. Ser. 179: 97-111.

Koehl, M. A. R. and Strickler, J. R. (1981). Copepod feeding currents: food capture at low Reynolds number. Limnol. Oceanogr. 26, 1062-1073.

Kristensen, A. and Dalen, J. (1986). Acoustic estimation o f size distribution and abundance of zooplankton. J. Acoust. Soc. Amer. 80: 601-611.

Kunze, E., Dower, J. F., Beveridge, I., Dewey, R. and Bartlett, K. P. (2006). Observations of biologically generated turbulence in a coastal inlet. Science 313: 1768-1770.

Kunze, E., Dower, J. F., Dewey, R. and D'asaro, E. A. (2007). Mixing it up with krill. Science 318: 1239.

Landau, L. (1944). A new exact solution of Navier-Stokes equations. Doklady Akademii nauk SSSR 43: 286-288.

Lasker, R. (1966). Feeding, growth, respiration and carbon utilization of a euphausiid crustacean. J. Fish. Res. Board Canada 23: 1291-1317.

Lauder, G. V. and Madden, P. G. A. (2008). Advances in comparative physiology from high speed imaging of animal and fluid motion. Ann. Rev. Physiol. 70: 143-163.

Lenz P. H. and Hartline, D. K. (1999). Reaction times and force production during escape behavior of a calanoid copepod *Undinula vulgaris*. Mar. Biol. 133: 249-258.

Lenz, P. H. and Yen, J. (1993). Distal setal mechanoreceptors of the first antennae of marine copepods. Bull. Mar. Res. 53: 170-179.

Malkiel, E., Sheng, J., Katz, J. and Strickler, J. R. (2003). The three-dimensional flow field generated by a feeding calanoid copepod measured using digital holography. J. Exp. Biol. 206: 3657-3666.

Marr, J. S. W. (1962). The natural history of and geography of the Antarctic krill (*Euphausia superba* Dana). Discovery Rep. 32: 33-464.

Mauchline, J. (1980). Studies on patches of krill, *Euphausia superba* Dana. Biomass Handbook 6: 1-35.

McWhinnie, M. A. and Marciniak, P. (1964). Temperature response and tissue respiration in Antarctic crustacean with particular reference to the krill *Euphausia superba.* In Biology of the Antarctic Seas, (ed. M. O. Lee), American Geophysical Union.

Miller, D. G. M. and Hampton, I. (1989). Biology and ecology of Antarctic krill (*Euphausia superba* Dana): A review. BIOMASS Science Series 9: 1-166.

Miyashita, K., Aoki, I. and Inagaki, T. (1996). Swimming behavior and target strength of isada krill (*Euphausia pacifica*). ICES J. Mar. Sci. 53: 303-308.

Moore, P. A., Fields, D. M. and Yen, J. (1999). Physical constraints of chemoreception in foraging copepods. Limnol. Oceanogr. 44: 166-177.

Munk, W. and Wunsch, C. (1998). Abyssal recipes II: Energetics of tidal and wind mixing. Deep Sea Res. I 45: 1977-2010.

Nakamura, Y. and Turner, J. T. (1997). Predation and respiration by the small cyclopoid copepod *Oithonia similis*: How important is feeding on ciliates and heterotrophic flagellates? J. Plank. Res. 19: 1275-1288.

Naudascher, E. (1965). Flow in the wake of self-propelled bodies and related sources of turbulence. J. Fluid Mech. 22: 625-656.

Nicol, S. (1984). Population structure of daytime surface swarms of the euphausiid *Meganyctiphanes norvegica* in the Bay of Fundy. Mar. Ecol. Prog. Ser. 18: 241-251.

Nicol. S. and Endo, Y. (1997). Krill fisheries of the world. Fisheries Technical Paper 367. Food and Agriculture Association of the United Nations, Rome.

Nogueira, J., Lecuona, A. and Rodriquez, P. A. (1997). Data validation, false vectors correction and derived magnitudes calculation on PIV data. Meas. Sci. Technol. 8: 1493-1501.

O'Brien, D. P. (1989). Analysis of the internal arrangement of individuals within crustacean aggregations (*Euphausiacea, Mysidacea*). J. Exp. Mar. Biol. Ecol. 128: 1-30.

Ohman, M. D. (1990). The demographic benefits of diel vertical migration by zooplankton. Ecol. Monogr. 60: 257-281.

Parker, F. R. Jr. (1975). Reduced metabolic rates in fishes as a result of induced schooling. Trans. Am. Fish. Soc. 1: 125-131.

Patria, M. P. and Wiese, K. (2004). Swimming in formation in krill (*Euphausiacea*), a hypothesis: dynamics of the flow field, properties of antennular sensor systems and asensory-motor link. J. Plank. Res. 26: 1315-1325.

Peng, J. F and Dabiri, J. O. (2007). A potential-flow, deformable-body model for fluid–structure interactions with compact vorticity: Application to animal swimming measurements. Exp. Fluids 43: 655-664.

Peng, J. F, Dabiri, J. O., Madden, P. G. and Lauder, G. V. (2007). Non-invasive measurement of instantaneous forces during aquatic locomotion: A case study of the bluegill sunfish pectoral fin. J. Exp. Biol. 210: 685-698.

Raffel, M., Willert, C. and Kompenhans, J. (1998). Particle Image Velocimetry - A Practical Guide. New York: Springer-Verlag.

Ritz, D. A. and Metillo, E. B. (1998). Costs and benefits of swarming behavior in mysids: Does orientation and position in the swarm matter? J. Mar. Biol. Ass. U.K. 78: 1011-1014.

Ritz, D. A. (2000). Is social aggregation in aquatic crustaceans a strategy to conserve energy? Can. J. Fish. Aquat. Sci. 57: 59-67.

Schlichting, H. and Gersten, K. (2000) Boundary Layer Theory. Springer-Verlag.

Sheng, J., Malkiel, E., Katz, J., Adolf, J., Belas, R. and Place, A. R. (2007). Digital holographic microscopy reveals prey-induced changes in swimming behavior of predatory dinoflagellates. Proc. Nat. Acad. Sci. USA 104: 17512-17517.

Siegel, V. (2005). Distribution and population dynamics of *Euphausia superba*: Summary of recent findings. Polar Biol. 29: 1-22.

Sirviente, A. I. and Patel, V. C. (2000). Wake of a self-propelled body, Part 1: Momentumless wake. AIAA J. 38: 613-619.

Small, L. F. and Hebard, J. F. (1967). Respiration of a vertically migrating marine crustacean *Euphausia pacifica* Hansen. Limnol. Oceangr. 12: 272-280.

Small, L. F., Hebard, J. F. and McIntire, C. D. (1967). Respiration in euphausiids. Nature 211: 1210-1211.

Squire, H. B. (1951). The round laminar jet. Quart. J. Mech. Appl. Math. 4: 321-329.

Stamhuis, E. J., and Videler, J. J. (1995). Quantitative flow analysis around aquatic animals using laswer sheet particle image velocimetry. J. Exp. Biol. 198: 283-294.

Stamhuis, E. J., Videler, J. J., van Duren, L. A. and Mueller, U. K. (2002). Applying digital particle image velocimetry to animal-generated flows: Traps, hurdles and cures in mapping steady and unsteady flow in *Re* regimes between 10^{-2} and 10^{5}. Exp. Fluids 33: 801-813.

Stearns, D. E. and Forward, R. B. Jr. (1984). Photosensitivity of the calanoid copepod *Acartia tonsa*. Mar. Biol. 82: 85-89.

Strand, S. W. and Hamner W. M. (1990). Schooling behavior of Antarctic krill (*Euphausia superba*) in laboratory aquaria: Reactions to chemical land visual stimuli. Mar. Biol. 106: 355-359.

Strickler, J. R. (1977). Observation of swimming performances of planktonic copepods. Limnol. Oceanogr. 22: 165-170.

Strickler, J. R. (1982). Calanoid copepods, feeding currents, and the role of gravity. Science 218: 158-160.

Svensen, C., and Kiørboe, T. (2000). Remote prey detection in *Oithona similis*: Hydromechanical versus chemical cues. J. Plank. Res. 22: 1155-1166.

Swadling, K. M., Ritz, D. A., Nicol, S., Osborn, J. E. and Gurney, L. J. (2005). Respiration rate and cost of swimming for Antarctic krill, *Euphausia superba,* in large groups in the laboratory. Mar. Biol. 146: 1169-1175.

Timm, N. H. (2002). Applied Multivariate Analysis. Springer-Verlag.

Tiselius, P. and Jonsson, P. R. (1990). Foraging behavior of six calanoid copepods: Observations and hydrodynamic analysis. Mar. Ecol. Prog. Ser. 66: 23-33.

Titelman, J. (2001). Swimming and escape behavior of copepod nauplii: Implications for predator-prey interactions among copepods. Mar. Ecol. Prog. Ser. 213: 203-213.

Titelman, J. and Kiørboe, T. (2003). Predator avoidance by nauplii. Mar. Ecol. Prog. Ser. 247: 137-149.

Torres, J. J. and Childress, J. J. (1983). Relationship of oxygen consumption to swimming speed in *Euphausia pacifica*. I. Effects of temperature and pressure. Mar. Biol. 74: 79-86.

Tytell, E. D. (2006). Median fin function in bluegill sunfish *Lepomis macrochis*: streamwise vortex structure during steady swimming. J. Exp. Biol. 209: 1516-1534.

van Duren, L. A. and Videler, J. J. (2003). Escape from viscosity: The kinematic and hydrodynamics of copepod foraging and escape swimming. J. Exp. Biol. 206: 269-279.

van Duren, L. A., Stamhuis, E. J. and Videler, J. J. (1998). Reading the copepod personal ads: Increasing encounter probability with hydromechanical cues. Phil. Trans. R. Soc. Lond. 353: 691-700.

van Duren, L. A., Stamhuis, E. J. and Videler, J. J. (2003). Copepod feeding currents: Flow patterns, filtration rates and energetics. J. Exp. Biol. 206: 255-267.

Viitasalo, M., Kiørboe, T., Flinkman, J., Pedersen, L. W. and Visser, A. W. (1998). Predation and vulnerability of planktonic copepods: consequences of predator foraging strategies and prey sensory abilities. Mar. Ecol. Prog. Ser. 175: 129-142.

Visser, A. W. (2001). Hydromechanical signals in the plankton. Mar. Ecol. Prog. Ser. 222: 1-24.

Visser, A. W. (2007). Biomixing of the oceans? Science 316: 838-839.

Visser, A. W. (2007). Mixing it up with krill (Response). Science 318: 1239.

Vogel, S. (1994). Life in Moving Fluids: The Physical Biology of Flow. Princeton University Press.

Waggett, R. J. and Buskey, E. J. (2007). Copepod escape behavior in non-turbulent and turbulent hydrodynamic regimes. Mar. Ecol. Prog. Ser. 334: 193-198.

Watkins, J. L. and Murray, A. W. A. (1998). Layers of Antarctic krill, *Euphausia superba*: are they just long krill swarms? Mar. Biol. 131: 237-247.

Weihs, D. (1973). Hydromechanics of fish schooling. Nature 241: 290-291.

Westerweel, J. (1994). Efficient detection of spurious vectors in particle image velocimetry data. Exp. Fluids 16: 236-247.

Westerweel, J. (1997). Fundamentals of digital particle image velocimetry. Meas. Sci. Tech. 8: 1379-1392.

Wickstead, J. H. (1976). Marine Zooplankton. The Institute of Biology's Studies in Biology no. 62. Edward Arnold Limited, London.

Wiese, K. (1996). Sensory capacities of Euphausiids in the context of schooling. Mar. Fresh. Behav. Physiol. 28: 183-194.

Wiese, K. and Ebina, Y. (1995). The propulsion jet of *Euphausia superba* (Antarctic krill) as a potential communication cue among conspecifics. J. Mar. Biol. Ass. U.K. 75: 43-54.

Wiese, K. and Marschall, H. P. (1990). Sensitivity to vibration and turbulence of water in context with schooling in Antarctic krill *Euphausia superba.* In Frontiers in Crustacean Neurobiology, (eds. K. Wiese et al.), pp. 121-130, Birkhäuser Verlag.

Woodson, C. B., Webster, D. R., Weissburg, M. J. and Yen, J. (2005). Response of copepods to physical gradients associated with structure in the ocean. Limnol. Oceanogr. 50: 1552-1564.

Woodson, C. B., Webster, D. R., Weissburg, M. J. and Yen, J. (2007a). Cue hierarchy and foraging of calanoid copepods: Ecological implications of oceanographic structure, Mar. Ecol. Prog. Ser. 330: 163-177.

Woodson, C. B. Webster, D.R., Weissburg, M. J. and Yen, J. (2007b). The prevalence and implications of copepod behavioral responses to oceanographic structure. Integr. Comp. Biol. 47: 831-846.

Yen, J. (1983). Effects of prey concentrations, prey size, predator life stage, predator starvation, and season on predation rates of the carnivorous copepod *Euchaeta elongata*. Mar. Biol. 75: 69-77.

Yen, J. (1985). Selective predation by the carnivorous marine copepod *Euchaeta elongata*: laboratory measurements of predation rates verified by field observations of temporal/spatial feeding patterns. Limnol. Oceanogr. 30: 577-597.

Yen, J. (1988). Directionality and swimming speeds in predator-prey and female-male interactions of *Euchaeta rimana*, a subtropical marine copepod. Bull. Mar. Sci. 43: 395-403.

Yen, J. (1991). Predatory feeding behavior of an Antarctic marine copepod, *Euchaeta antarctica*. Polar Res. 10: 433-442.

Yen, J. (2000) Life in transition: Balancing intertial and viscous forces by planktonic copepods. Biol. Bull. 198: 213-224.

Yen, J. and Fields, D. M. (1992). Escape responses of *Acartia hudsonica* (copepoda) nauplii from the flow field of *Temora longicornis* (copepoda). Arch. Hydrobiol. Beih. 36: 123-134

Yen, J. and Nicoll, N. T. (1990). Setal array on the 1st antennae of a carnivorous marine copepod, *Euchaeta norvegica*. J. Crustac. Biol. 10: 218-224.

Yen, J. and Strickler, J. R. (1996). Advertisement and concealment in the plankton: what makes a copepod hydrodynamically conspicuous? Invertebr. Biol. 115: 191-205.

Yen, J., Brown, J. and Webster, D. R. (2003). Analysis of the flow field of the krill, *Euphausia pacifica*. Mar. Fresh. Behav. Physiol. 36: 307-319.

Yen, J., Lenz, P. H., Gassie, D. V. and Hartline, D. K. (1992). Mechanoreception in marine copepods: electrophysiological studies on the first antennae. J. Plank. Res. 14: 459-512.

Yen, J., Sanderson, B., Strickler, J. R. and Okubo, A. (1991). Feeding currents and energy dissipation by *Euchaeta rimana*, a subtropical pelagic copepod. Limnol. Oceanogr. 36: 362-369.

Yen, J., Weissburg, M. J. and Doall, M. H. (1998). The fluid physics of signal perception by mate-tracking copepods. Phil. Trans. R. Soc. Lond. B 353: 787-804.

Zhou, M. and Dorland, R. D. (2004). Aggregation and vertical migration behavior of *Euphausia superba.* Deep Sea Res. II 51: 2119-2137.

Zhou, M., Zhu, Y. and Tande, K. S. (2005). Circulation and behavior of euphasiids in two Norwegian sub-Arctic fjords. Mar. Ecol. Prog. Ser. 300: 159-178.